Heat Engineering

Journal of Research

of the

National Bureau of Standards

AUGUST 1953

VOLUME 51 NUMBER 2

U. S. DEPARTMENT OF COMMERCE
Sinclair Weeks, Secretary
NATIONAL BUREAU OF STANDARDS
A. V. Astin, Director

AUGUST • 1953
VOLUME • 51
NUMBER • 2

JOURNAL OF RESEARCH

of the

NATIONAL BUREAU OF STANDARDS

PERIODICALS OF THE NATIONAL BUREAU OF STANDARDS

The National Bureau of Standards is engaged in fundamental and applied research in physics, chemistry, mathematics, and engineering. Projects are conducted in fifteen fields: electricity, optics and metrology, heat and power, atomic and radiation physics, chemistry, mechanics, organic and fibrous materials, metallurgy, mineral products, building technology, applied mathematics, electronics, ordnance development, radio propagation, and missile development. The Bureau has custody of the national standards of measurement and conducts research leading to the improvement of scientific and engineering standards and of techniques and methods of measurement. Testing methods and instruments are developed; physical constants and properties of materials are determined; and technical processes are investigated.

JOURNAL OF RESEARCH

Internationally known as a leading scientific periodical, the Journal presents research papers by authorities in the specialized fields of physics, mathematics, chemistry, and engineering. Complete details of the work are presented, including laboratory data, experimental procedures, and theoretical and mathematical analyses. Annual subscription: domestic, $5.00; foreign, $6.75.

TECHNICAL NEWS BULLETIN

Summaries of current research at the National Bureau of Standards are published each month in the Technical News Bulletin. The articles are brief, with emphasis on the results of research, chosen on the basis of their scientific or technologic importance. Lists of all Bureau publications during the preceding month are given, including Research Papers, Handbooks, Applied Mathematics Series, Building Materials and Structures Reports, and Circulars. Each issue contains 12 or more two-column pages; illustrated. Annual subscription: domestic, $1.00; foreign, $1.35.

BASIC RADIO PROPAGATION PREDICTIONS

The Predictions provide the information necessary for calculating the best frequencies for communication between any two points in the world at any time during the given month. The data are important to all users of long-range radio communications and navigation, including broadcasting, airline, steamship, and wireless services, as well as to investigators of radio propagation and ionosphere. Each issue, covering a period of one month, is released three months in advance and contains 30 large pages, including pertinent charts, drawings, and tables. Annual subscription: domestic, $1.00; foreign, $1.25.

Order all publications from the Superintendent of Documents
U. S. Government Printing Office, Washington 25, D. C.

The printing of this publication has been approved by the Director of the Bureau of the Budget, May 29, 1953.

Journal of Research of the National Bureau of Standards Vol. 51, No. 2, August 1953 Research Paper 2432

Heat Capacity, Heats of Fusion and Vaporization, and Vapor Pressure of Tetrafluoroethylene[1]

George T. Furukawa, Robert E. McCoskey, and Martin L. Reilly

The heat capacity of tetrafluoroethylene of 99.9$_6$-mole-percent purity was measured in an adiabatic calorimeter from 16° to 210° K. A smoothed table of heat capacity at 5-degree intervals from 0° to 210° K was constructed from the data. The average heat of fusion of three experiments gave 7,714.5 ±7 abs j mole^{-1} at the triple-point temperature of 142.00 ±0.01° K. The three heats of vaporization measurements at the normal boiling temperature of 197.53 ±0.01° K gave an average value of 16,821 ±10 abs j mole^{-1}. The results of the vapor-pressure measurements from 142° to 208° K can be represented by the equation

$$\log_{10} p_{\text{mm Hg}} = 4.71241 - \frac{972.9810}{T} + 4.816562 \times 10^{-2} T - 2.427347 \times 10^{-4} T^2 + 3.958793 \times 10^{-7} T^3.$$

The entropy of the ideal gas tetrafluoroethylene at 197.53° K and 1 atm was computed from the calorimetric data to be 270.06 ±0.37 abs j deg^{-1} mole^{-1} or 64.55 ±0.09 cal deg^{-1} mole^{-1}(1 cal=4.1840 abs j). The entropy was computed from molecular and spectroscopic data to be 64.54 cal deg^{-1} mole^{-1}.

1. Introduction

In continuation of the program for the thermodynamic investigation of high temperature resistant polymers and their respective monomers or prototype molecules, heat-capacity, heats of fusion and vaporization, and vapor-pressure measurements were conducted with tetrafluoroethylene (C_2F_4). This substance has recently become important as the monomer in the production of polytetrafluoroethylene (Teflon) plastic, which has exceedingly high chemical and thermal stability. Heat-capacity studies with this polymer have recently been reported from the National Bureau of Standards.[2]

2. Apparatus and Method

The heat-capacity and heat-of-fusion measurements with tetrafluoroethylene were made in an adiabatic calorimeter which has been previously described.[3] The heat of vaporization was determined in another adiabatic calorimeter constructed by R. B. Scott of the Bureau. This calorimeter was similar in design to those described by Osborne and Ginnings [4] and by Aston, et al,[5] in which a throttle valve was contained within the space enclosed by the adiabatic shield. Briefly, during the vaporization experiments a known electric power was supplied continuously, and the vapor was removed isothermally from the calorimeter by controlling the throttle valve. The material removed from the calorimeter in a measured time interval, was collected by condensation in a small high-pressure cylinder (150 ml) and weighed.

In the vapor-pressure measurements the same calorimeter used for the vaporization measurements served as a thermostated container. No provision was made to stir the sample. The pressures were read by means of a mercury manometer and a mirror-backed glass scale. The readings were converted to standard mm Hg (g=980.665 cm/sec^2, temperature=0° C) on the basis that the local gravity is 980.076 cm/sec^2.

The International Temperature Scale[6] was used, and below 90° K, a provisional scale[7] was used based on a set of platinum resistance thermometers calibrated against a helium-gas thermometer.

3. Material

The sample was originally received in a high-pressure cylinder (300 g. to 1.5 ft.^{3}) and inhibited against polymerization and other reactions. To remove the inhibitor, the material was passed through a train of gas-washing bottles containing concentrated sulfuric acid, and to remove traces of permanent gases, it was later frozen and pumped three times. About 155 g of the purified material was collected. As this substance is considered to be hazardous, particularly in the uninhibited state, it was kept at temperatures below that of dry-ice at all times, except when being weighed.

The purity of the material was determined in the calorimeter before the thermal measurements from the equilibrium melting temperatures [8] on the bases that no solid solution was formed and that the liquid solution followed Raoult's law. The equilibrium temperatures and the corresponding reciprocal of the fraction melted, F, are given in table 1.

[1] This paper is based on the work sponsored by the Ordnance Corps, U. S. Department of the Army.
[2] G. T. Furukawa, R. E. McCoskey, and G. J. King, J. Research NBS 49, 273 (1952) RP2364.
[3] R. B. Scott, C. H. Meyers, R. D. Rands, Jr., F. G. Brickwedde, and N. Bekkedahl, J. Research NBS 35, 39 (1945) RP1661.
[4] N. S. Osborne and D. C. Ginnings, J. Research NBS 39, 453 (1947) RP1841.
[5] J. G. Aston, H. L. Fink, G. J. Janz, and K. E. Russell, J. Am. Chem. Soc. 73, 1939 (1951).
[6] H. F. Stimson, J. Research NBS 42, 209 (1949) RP1962.
[7] H. J. Hoge and F. G. Brickwedde, J. Research NBS 22, 351 (1939) RP1188.
[8] G. T. Furukawa, D. C. Ginnings, R. E. McCoskey, and R. A. Nelson, J. Research NBS 46, 195 (1951) RP2191.

262279—53——1

TABLE 1. *Equilibrium melting temperatures of tetrafluoroethylene*

Mole fraction impurity = 0.0460 ΔT, °K = 273.16° + °C

Reciprocal of fraction melted, $1/F$	T
	°K
9.59	141.9762
4.73	141.9936
3.67	141.9959
1.93	142.0012
1.46	142.0013
1.21	142.0016
0.00	[a] 142.0048
Triple-point temperature, 142.00±0.01° K. Purity, 99.98$_0$ mole percent.	

[a] Extrapolated.

The data were plotted and the purity was computed from the slope of the curve to be 99.98$_0$ mole percent. The intercept or the triple-point temperature of pure tetrafluoroethylene was found to be 142.00 ±0.01° K. The results of the premelting heat-capacity measurements made during the course of this study indicated that the purity remained essentially the same. (The temperature in degrees Kelvin was obtained from the relation: °K = 273.16° + °C. Whenever the temperatures are expressed in the paper to the fourth decimal place, the last two figures are significant only in the measurement of small temperature differences.)

4. Heat Capacity

The heat-capacity measurements were made from 16° to 210° K. In the computation to obtain the net heat capacities, the observed gross-heat capacities were first smoothed, then the smoothed tare heat capacities were subtracted at the corresponding equally spaced integral temperatures. Curvature corrections (see footnote 8) were applied to the gross and tare heat capacities wherever significant. The vapor-pressure data obtained in this work and the liquid densities reported by Ruff and Bretschneider[9] were used to make vapor saturation corrections.[10]

The results of the heat-capacity measurements gave a precision of ±0.02 percent in the liquid and from ±0.02 to ±0.05 percent in the solid range, except for the lowest temperatures. There is, however, a fairly large uncertainty in the vapor-saturation correction to the heat capacity at the higher temperatures because the amount of material in the filling tube is not accurately determinable. Considering these factors, particularly the latter, and other possible sources of error, the uncertainty in the final heat-capacity values given in table 2 is believed to be ±0.2 percent. In table 2 the values below 15° K were obtained by the extrapolation (see footnote 8) of a Debye function fitted to experimental values between 16° and 30° K.

[9] O. Ruff and O. Bretschneider, Z. anorg. allgem. Chem. **210**, 173 (1933).
[10] H. J. Hoge, J. Research NBS **36**, 111 (1946) RP1693.

TABLE 2. *Molal heat capacity of tetrafluoroethylene at integral temperatures*

Molecular weight = 100.02, ° K = 273.16° + °C.

T	$C_{sat.}$[a]	T	$C_{sat.}$
Solid		°K	*abs j deg^{-1} mole^{-1}*
°K	*abs j deg^{-1} mole^{-1}*	120	73.20
0	0.0	125	75.95
5	.33	130	78.90
10	2.64	135	82.07
15	7.94	140	85.46
20	14.79	142.00	[b] 86.85
25	21.29	Liquid	
30	26.91		
35	31.65		
40	35.60	142.00	[b] 105.02
45	38.94	145	106.11
50	41.92	150	106.36
55	44.62	155	106.72
60	47.11	160	107.15
65	49.44	165	107.65
70	51.55	170	108.20
75	53.61	175	108.82
80	55.74	180	109.49
85	57.86	185	110.22
90	59.92	190	111.01
95	61.82	195	111.85
100	63.88	197.53	112.31
105	66.02	200	112.77
110	68.26	205	113.75
115	70.65	210	114.79

[a] $C_{sat.}$ is the heat capacity of the condensed phase under its vapor pressure.
[b] Extrapolated.

5. Heat of Fusion

The determination of the heat of fusion involved continuous introduction of electrical energy from a temperature just below the triple point to just above it and the correction for the heat capacity of the sample and container. Also, a small premelting correction was applied. The results of the measurements are given in table 3. The values given in the fifth column are the total heats required to melt the 156.2694 g in the calorimeter. Taking into account the precision obtained, and other possible sources of error, the uncertainty in the heat of fusion is considered to be ±7 abs j mole^{-1}.

TABLE 3. *Molal heat of fusion of tetrafluoroethylene*

Molecular weight = 100.02, mass of sample = 156.2694 g, triple-point temperature = 142.00° K, °K = 273.16° + °C

Temperature interval	Heat input	Heat capacity	Premelting	ΔH	ΔH
°K	*abs j*	*abs j*	*abs j*	*abs j*	*abs j mole^{-1}*
137.7930 to 143.7828	13,374.1	1,326.9	6.5	12,053.7	7,715.0
136.3972 to 144.1509	13,755.1	1,707.4	4.9	12,052.6	7,714.2
137.4175 to 143.9957	13,504.5	1,457.7	5.9	12,052.7	7,714.3
Mean heat of fusion					7,714.5
Standard deviation					±0.2

6. Heat of Vaporization

The heat-of-vaporization experiments were made at the normal boiling point (197.53° K) as determined by the vapor-pressure measurements. The experimentally observed quantity γ, the energy input per mole of sample collected,[11] is related to the

[11] N. S. Osborne, BSJ. Research **4**, 609 (1930) RP168.

molal heat of vaporization, L, by the expression

$$L=\gamma-TV\frac{dp}{dT},$$

where V is the molal volume of the liquid, T, the absolute temperature, and p, the vapor pressure. The experimentally observed quantities, the value of the conversion term (second term to the right of the equality sign), and the heat of vaporization are given in table 4. The molal volume for the conversion term was obtained from the densities of tetrafluoroethylene reported by Ruff and Bretschneider (see footnote 9). Considering the precision and other sources of error, the uncertainty in the heat of vaporization is believed to be ± 10 abs j mole^{-1}. The heat of vaporization, computed from the Clapeyron equation by using the vapor-pressure equation obtained in this work, the liquid densities reported by Ruff and Bretschneider (see footnote 9), and the Berthelot equation of state, amounted to 16,850 abs j mole^{-1}. This is in fair agreement with the observed value. The constants for the Berthelot equation were reported by Renfrew and Lewis.[12]

TABLE 4. *Molal heat of vaporization of tetrafluoroethylene at 197.53° K (1-atm pressure)*

Molecular weight = 100.02, °K = 273.16° + °C

γ	$TV\frac{dp}{dT}$	L
abs j mole^{-1}	*abs j mole*$^{-1}$	*abs j mole*$^{-1}$
16,884	71	16,813
16,901	71	16,830
16,890	71	16,819
Mean		16,821
Standard deviation		±4

7. Vapor Pressure

As there was no provision to stir the sample in the calorimeter, several series of vapor-pressure measurements were made from 142° to 208° K going down the temperature scale as well as up to check the temperature equilibrium. The agreement in the results of the measurements, as shown in table 5, indicates that equilibrium conditions existed. The vapor-pressure equation fitted to the experimental values is given by

$$\log_{10}p_{\text{mmHg}}=4.71241-\frac{972.9810}{T}+4.816562$$

$$\times10^{-2}T-2.427347\times10^{-4}T^2+3.958793\times10^{-7}T^3$$

In table 5 are given the deviations of the calculated values, based on this equation, from the observed values. Although the deviations from the equation vary somewhat systematically, no attempt was made to obtain a closer-fitting equation.

The normal boiling point was taken to be 197.53 ±0.01° K, although the equation gives 197.525° K and the difference in the rounding can be measured by the thermometer and by the manometer. The dp/dT at the normal boiling point is about 41 mm Hg per degree.

[12] M. M. Renfrew and E. E. Lewis, Ind. Eng. Chem. **38**, 870 (1946).

TABLE 5. *Vapor pressure of tetrafluoroethylene*

°K = 273.16° + °C

T_{obs}	p_{obs}	p_{calc}	$p_{obs}-p_{calc}$
Series I			
°K	*mm* Hg	*mm* Hg	*mm* Hg
206.66	1,217.8	1,217.5	0.3
207.50	1,268.6	1,268.6	.0
208.41	1,325.1	1,325.8	−.7
Series II			
175.82	197.1	197.2	−0.1
179.23	249.9	250.2	−.3
182.01	301.0	301.3	−.3
184.37	350.8	351.0	−.2
186.54	402.2	402.2	.0
Series III			
182.96	320.4	320.6	−0.2
188.27	447.0	447.2	−.2
190.11	499.2	499.3	−.1
193.30	601.0	600.9	.1
196.06	701.8	701.5	.3
196.06	701.4	701.5	−.1
198.41	797.5	797.2	.3
200.61	895.8	895.8	.0
202.84	1,005.6	1,005.4	.2
205.44	1,146.1	1,146.2	−.1
206.99	1,236.3	1,237.4	−1.1
Series IV			
°K	*mm* Hg	*mm* Hg	*mm* Hg
147.70	16.7	16.6	0.1
152.92	28.6	28.5	.1
155.77	37.8	37.6	.2
158.89	50.5	50.3	.2
164.15	79.7	79.8	−.1
169.69	124.7	124.9	−.2
175.35	190.5	190.7	−.2
178.27	233.9	234.2	−.3
180.96	280.7	281.1	−.4
Series V			
142.00	8.7	8.7	0.0
147.98	17.1	17.1	.0
152.33	26.9	26.8	.1
159.34	52.5	52.4	.1
168.56	114.3	114.3	.0
172.90	159.2	159.4	−.2
178.02	229.8	230.2	−.4
180.23	267.3	267.7	−.4
191.74	549.1	549.4	−.3

8. Experimental Entropy

The experimental data were used to compute the entropy of the ideal gas tetrafluoroethylene at 197.53° K and 1 atm. In table 6 are summarized the entropy computations. The Berthelot equation of state and the critical constants reported by Renfrew and Lewis (see footnote 12) were used to compute the gas imperfection. The uncertainty of ±0.37 abs j deg^{-1} $mole^{-1}$ for the entropy of ideal gas C_2F_4 at 197.53° K and 1 atm was obtained by statistically combining the uncertainty in the entropy of liquid C_2F_4 at 197.53° K and in the entropy of vaporization. The uncertainty in the gas imperfection correction was considered negligible.

In terms of the thermochemical calorie (1 cal = 4.1840 abs j) the calorimetric entropy of the ideal gas tetrafluoroethylene becomes 64.55 ±0.09 cal deg^{-1} mole $^{-1}$.

TABLE 6. *Summary of the Molal entropy of tetrafluoroethylene*

Molecular weight = 100.02, °K = 273.16° + °C., 1 cal = 4.1840 abs j

	abs j deg $^{-1}$ mole $^{-1}$
$S_{0°}$ (Debye)	3.42
$\Delta S_{0°\ to\ 142.00°}$ solid, numerical integration	90.73
$\Delta S_{142.00°}$ fusion, 7714.5/142.00	54.33
$\Delta S_{142°\ to\ 197.53°}$, liquid, numerical integration	35.75
Entropy of the liquid at 197.53° K	184.23 ±0.37
$\Delta S_{197.53°}$ vaporization 16621/197.53	85.16 ±0.05
$\Delta S_{197.53°}$ gas imperfection	0.67
Entropy, ideal gas at 197.53° K and 1 atm	270.06 ±0.37

WASHINGTON, March 13, 1953.

9. Entropy From Molecular and Spectroscopic Data

The entropy due to the external rotation was computed from the molecular constants taken from the electron diffraction results of Karle and Karle [13] in which the C—F and C=C bond distances and the FCF angle were given as 1.313 ±0.010 A, 1.313 ±0.035 A, and 114 ±2°, respectively. The moments of inertia calculated were $I_x = 152.9 \times 10^{-40}$ g-cm^2, $I_y = 254.7 \times 10^{-40}$ g-cm^2, and $I = 407.6 \times 10^{-40}$ g-cm^2. The fundamental constants used in the computation were essentially those given in the National Bureau of Standards Circular 461.[14]

The vibrational contribution to the entropy was computed from the recent frequency assignments of D. E. Mann, N. Aquista, and E. K. Plyler at the Bureau.

The entropy computed from the molecular and spectroscopic data is summarized and compared with the calorimetric entropy in table 7. An excellent agreement is shown in the two results.

TABLE 7. *Molal entropy of tetrafluoroethylene at 197.53° K from molecular and spectroscopic data*

Molecular weight = 100.02, °K = 273.16° + °C., 1 cal = 4.1840 abs j.

	cal deg $^{-1}$ mole $^{-1}$
S, translation	37.67
S, external rotation	22.58
S, vibration	4.29
S, total, ideal gas at 197.53° K and 1 atm	64.54
S, calorimetric	64.55

[13] I. L. Karle and J. Karle, J. Chem. Phys. **18**, 963 (1950).
[14] F. D. Rossini, K. S. Pitzer, W. J. Taylor, J. P. Ebert, J. E. Kilpatrick, C. W. Beckett, M. G. Williams, and H. G. Werner, NBS Circular 461 (November 1947).

Journal of Research of the National Bureau of Standards Vol. 51, No. 2, August 1953 Research Paper 2433

Hydrothermal Preparation of Some Strontium Silicates

Elmer T. Carlson and Lansing S. Wells

A study was made of the formation of hydrated strontium silicates under hydrothermal conditions. Seven hydrated compounds, believed to have the following compositions, were prepared: $SrO \cdot 2SiO_2 \cdot H_2O$, $SrO \cdot SiO_2 \cdot H_2O$, $2SrO \cdot 2SiO_2 \cdot 3H_2O$, $3SrO \cdot 2SiO_2 \cdot 3H_2O$, $3SrO \cdot 2SiO_2 \cdot 4H_2O$, $2SrO \cdot SiO_2 \cdot H_2O$, and $3SrO \cdot SiO_2 \cdot 2H_2O$. The anhydrous compounds $SrO \cdot SiO_2$ and $2SrO \cdot SiO_2$ were obtained by hydrothermal synthesis at temperatures as low as 124° and 142° C., respectively. No evidence was found that the anhydrous strontium silicates possess hydraulic binding properties. X-ray powder diffraction patterns and some optical data are given for the various hydrates, and possible relationships with the calcium silicates are discussed.

1. Introduction

During the course of an investigation of the possibility of preparing compounds of the hydrogarnet type described by Flint, McMurdie, and Wells [1],[1] but with strontium substituted for calcium, it became necessary to identify the strontium silicates that were obtained in some of the experiments. In the absence of any specific data on the hydrated strontium silicates in the literature, a brief study was made of these compounds, and incidentally of the anhydrous silicates as well.

The anhydrous strontium silicates have been described by Eskola [2], who also worked out the phase diagram for the system $SrO \cdot SiO_2$. The meta- and orthosilicates, $SrSiO_3$ and Sr_2SiO_4, respectivel were the only compounds found in this system. The metasilicate is apparently hexagonal, but forms a solid-solution series with α-$CaSiO_3$ (pseudowollastonite) which is monoclinic, and may therefore be monoclinic also. An X-ray diffraction pattern for the orthosilicate Sr_2SiO_4 has been published by O'Daniel and Tscheischwili [3]. Heats of formation of both silicates from the oxides have been reported by Nacken [4].

Preparation of tristrontium silicate has recently been reported by Nurse [5], who also gives the X-ray diffraction pattern. The compound was found not to be isomorphous with tricalcium silicate.

The hydrated strontium silicates appear to have been studied very little. Jordis and Kantner [6], obtained a precipitate approximating a 1:1 molar ratio by the reaction between Na_2SiO_3 and a soluble strontium compound, and it was assumed that the product was a hydrated metasilicate. Zhuravlev [7] reports that Sr_2SiO_4 possesses binding properties but gives no details as to the composition of the hydrated product.

[1] Figures in brackets indicate the literature references at the end of this paper.

2. Anhydrous Strontium Silicates

Strontium metasilicate and orthosilicate were prepared from stoichiometric mixtures of $SrCO_3$ and silicic acid (reagent grade) by heating for an hour in an electric furnace at about 1,425° C. The composition was checked by analysis and found to be in close agreement with that calculated, but the microscope showed a little inhomogeneity in the metasilicate, and more in the orthosilicate.

The metasilicate preparation was considerably improved in homogeneity by fusion in an oxygen blast. This also increased the average crystal size. Crystals of better shape, however, were produced by hydrothermal means, as described later, and these were used for determination of optical characteristics. The interference figure indicated that the crystal is biaxial, with a very small optic axial angle; the symmetry, therefore, is not hexagonal. The refractive indices were found to be $\alpha = 1.597$, $\gamma = 1.637$, in good agreement with those given by Eskola [2]. The β-index is close to 1.597.

An X-ray powder diffraction pattern[2] for a hydrothermal preparation of $SrO \cdot SiO_2$ is given in table 1. So far as known, no pattern for this compound has hitherto been published. The sample prepared by fusion of the mixed oxides gave a similar pattern except that many of the lines appeared to be double, triple, or quadruple, instead of forming well-defined single peaks. The significance of this difference is not known. It might conceivably indicate the existence of two forms having slightly different symmetry, but no evidence of any phase transformation was observed on differential thermal analysis of the preparation. This is in agreement with the findings of Eskola.

The X-ray pattern resembles that of α-$CaO \cdot SiO_2$, indicating a relationship between the two as sug-

[2] X-ray diffraction patterns reported herein were made on an X-ray Geiger counter diffractometer, using Cu $K\alpha_1$ radiation.

TABLE 1. *Interplanar spacings and relative intensities of X-ray diffraction lines for the strontium silicates*

$SrO \cdot SiO_2$		$SrO \cdot 2SiO_2 \cdot H_2O$		$SrO \cdot SiO_2 \cdot H_2O$		$2SrO \cdot 2SiO_2 \cdot 3H_2O$	
d	*I*	*d*	*I*	*d*	*I*	*d*	*I*
5.07	18	7.02	12	5.25	16	7.31	10
3.57	65	4.27	10	4.26	100	4.60	10
3.37	38	3.67	32	3.85	5	3.68	15
2.92	100	3.44	100	3.64	31	3.55	15
2.53	17	3.29	44	3.27	71	3.23	100
2.07	68	3.16	10	2.96	40	3.09	47
1.914	33	3.03	53	2.80	39	2.64	15
1.783	10	2.78	19	2.76	18	2.41	20
1.759	3	2.73	18	2.72	31	2.23	33
1.686	17	2.65	38	2.63	39	2.05	17
1.603	13	2.31	7	2.57	35	1.967	32
1.527	17	2.24	22	2.40	7	1.932	19
1.460	17	2.17	34	2.28	28	1.770	9
1.350	5	2.07	70	2.18	26	1.750	12
1.307	17	1.92	10	2.13	10	1.729	12
.....	.....	1.87	13	2.08	25	1.632	11
.....	.....	1.83	18	1.96	12	1.576	9
.....	.....	1.76	39	1.93	31	1.502	7
.....	.....	1.66	14	1.88	17	1.475	7
.....	.....	1.61	22	1.81	11	.....	.....
.....	.....	1.52	18	1.76	8	.....	.....
.....	.....	.....	.....	1.75	4	.....	.....
.....	.....	.....	.....	1.66	9	.....	.....
.....	.....	.....	.....	1.64	21	.....	.....
.....	.....	.....	.....	1.56	7	.....	.....
.....	.....	.....	.....	1.50	9	.....	.....
.....	.....	.....	.....	1.44	11	.....	.....
.....	.....	.....	.....	1.42	9	.....	.....
.....	.....	.....	.....	1.38	11	.....	.....

$3SiO_2 \cdot 2SiO_2 \cdot 3H_2O$		$3SiO_2 \cdot 2SiO_2 \cdot 4H_2O$		$2SrO \cdot SiO_2 \cdot H_2O$		$3SrO \cdot SiO_2 \cdot 2H_2O$	
6.73	50	4.89	50	9.60	13	10.13	40
6.11	7	3.73	95	5.74	8	7.54	9
4.25	42	3.53	5	5.02	17	7.03	7
3.68	5	2.96	39	4.75	12	5.05	20
3.49	14	2.76	100	4.01	16	4.79	22
3.33	65	2.64	29	3.83	9	4.68	7
3.16	13	2.44	12	3.58	79	4.53	23
3.10	11	2.32	32	3.50	10	4.44	10
2.89	100	2.07	21	3.45	10	3.69	25
2.80	10	1.971	21	3.35	38	3.51	25
2.76	7	1.906	62	3.24	10	3.44	7
2.69	4	1.810	13	3.17	100	3.37	23
2.50	7	1.743	6	3.00	32	3.22	26
2.41	23	1.669	15	2.92	60	3.11	100
2.36	7	1.545	12	2.84	42	3.04	35
2.21	20	1.483	13	2.81	22	2.98	37
2.18	9	1.377	13	2.76	22	2.95	15
2.11	14	1.332	11	2.55	17	2.75	19
2.05	16	1.220	10	2.51	10	2.61	32
2.02	23	.....	.....	2.45	27	2.49	15
1.975	18	.....	.....	2.31	7	2.39	8
1.860	10	.....	.....	2.26	9	2.34	5
1.805	20	.....	.....	2.13	14	2.13	41
1.778	14	.....	.....	2.09	15	2.05	15
1.676	12	.....	.....	2.05	37	2.01	20
1.661	11	.....	.....	2.01	10	1.971	33
1.572	8	.....	.....	1.97	20	1.932	10
1.454	8	.....	.....	1.94	10	1.845	18
1.422	5	.....	.....	1.90	37	1.806	12
.....	.....	.....	.....	1.82	17	1.776	8
.....	.....	.....	.....	1.73	15	1.736	11
.....	.....	.....	.....	1.60	10	1.685	18
.....	.....	.....	.....	1.53	9	1.637	11
.....	.....	.....	.....	1.43	11	1.602	8
.....	.....	.....	.....	.....	.....	1.572	9

gested by Eskola. This is supported by the similarity in optical properties.

No attempt was made to prepare anhydrous tristrontium silicate.

3. Hydrated Strontium Silicates Prepared at Atmospheric Pressure

3.1. $3SrO \cdot 2SiO_2 \cdot 3H_2O$

The compound $3SrO \cdot 2SiO_2 \cdot 3H_2O$ was obtained by slowly adding sodium silicate solution (12 g $Na_2SiO_3 \cdot 9H_2O$ in a small amount of water) to a boiling solution of strontium hydroxide (30 g of the octahydrate in about 800 ml of water). Boiling was continued for an hour, and the mixture was kept on the steam bath overnight. The precipitate, apparently gelatinous at first, became completely crystalline. The crystals were very small, acicular or lath-shaped and slightly birefringent, with negative elongation. From the analysis of two separate preparations, the molar ratio was calculated to be $SrO:SiO_2:H_2O = 2.96:2:3.26$ [3] for the one, 2.97:2:3.17 for the other. From this the formula $3SrO \cdot 2SiO_2 \cdot 3H_2O$ is assumed to be correct. X-ray diffraction data are given in table 1.

Larger crystals of the same compound were subsequently obtained hydrothermally. Some of these are shown in figure 1. They were found to be biaxial, positive, with refractive indices: $\alpha = 1.602$; $\beta = 1.602$; $\gamma = 1.614$. The optic axial angle was very small.

Differential thermal analysis of this compound shows a large endothermic effect at about 340° C, corresponding to dehydration. Two small exothermic effects occur at 820° and 890° C, suggesting the possibility that the loss of water involves a break-down to the oxides, which subsequently recombine to form anhydrous silicates.

During the preparation of this material, the reactants were in such proportion as to provide a considerable excess of $Sr(OH)_2$, hence it may be assumed that no more basic hydrate may be formed by this method. An attempt to prepare a less basic compound by reducing the $Sr(OH)_2$ concentration to the same molar strength as the Na_2SiO_3 resulted in an amorphous product.

3.2. $3SrO \cdot 2SiO_2 \cdot 4H_2O$

By boiling a mixture of silica gel and strontium hydroxide solution for half an hour, a different compound was obtained. This consisted of distinctive dendritic or feathershaped crystals with moderate birefringence. From chemical analysis, the molar ratio $SrO:SiO_2:H_2O$ was calculated to be 3.04:2:4.06 from which it was concluded that the composition was $3SrO \cdot 2SiO_2 \cdot 4H_2O$. The differential heating curve on this material is similar to that of the 3:2:3 hydrate except that the dehydration break is double, with the first peak at 230° and a larger one at 300° C, indicating that the water is driven off in two stages. The exothermic breaks occur at 800° and 890°. It is concluded that the 3:2:4 hydrate first loses one molecule of water, forming the 3:2:3 hydrate, which is then decomposed on further heating. This conclusion is supported by results of hydrothermal experiments to be described later.

The 3:2:4 compound was also obtained in a large number of hydrothermal experiments. Figure 2 is a photomicrograph of one such preparation; the crystals are larger than those obtained by boiling, but exhibit the same habit of growth.

[3] The percentage of loss in weight on ignition at 1,100° was taken as the percentage of H_2O, with no correction for the slight amount of carbonate that may be assumed to have been formed from the CO_2 in the water and air in the reaction vessel.

FIGURE 1. *Crystals of* $3SrO{\cdot}2SiO_2{\cdot}3H_2O$ *(prismatic crystals), together with* $3SrO{\cdot}SiO_2{\cdot}H_2O$ *(faint needles).*

Magnification, ×190.

FIGURE 2. *Dendritic crystals of* $3SrO{\cdot}2SiO_2{\cdot}4H_2O$.

Magnification, ×700.

Comparison of the X-ray diffraction patterns of over 20 preparations in which this compound was identified showed that they were about equally divided into 2 types. The pattern given in table 1 is typical of the group arbitrarily designated type 1. In type 2 about half the lines were in substantially the same positions as in type 1, the rest being shifted distinctly to the right (that is, toward smaller spacings), except for the line at 2.07, which was shifted to 2.09. The significance of this is unknown. No correlation was observed between the X-ray pattern type and chemical analysis, presence of other phases, temperature of reaction, or refractive indices.

The indices also varied among the several preparations, but were difficult to determine precisely. The high index ranged from 1.627 to 1.637; the low index from 1.595 to 1.617.

The same compound was obtained by heating silica gel with strontium hydroxide solution on a steam bath overnight (temperature about 75° C), but the reaction was incomplete. Similar reaction mixtures held at 30° and at 50° for several months failed to develop any of the 3:2:4 compound. On the other hand, the product was not entirely amorphous in either case. An X-ray diffraction pattern of the material from the 30° test showed two rather diffuse lines. The 50° product showed the same lines somewhat sharper with the addition of a few others. Apparently conversion was only partial, and the crystalline product has not been identified.

4. Hydrothermal Reactions

4.1. Procedure

Strontium hydroxide and silica gel were the raw materials for most of the hydrothermal experiments. The strontium hydroxide was "CP" grade and contained a variable amount of carbonate, which was removed by a process of solution, filtration, and recrystallization. Four different lots of silica were used: (I) reagent grade "Silicic Acid" containing 0.16 percent of nonvolatile residue after treatment with hydrofluoric acid; (II) a commercial silica gel, extremely fine and highly reactive but containing 3 percent of nonvolatile residue, including 1.17 percent of Na_2O; (III) a commercial silica gel containing 0.45 percent of nonvolatile residue; (IV) a specially purified gel, relatively coarse and unreactive, containing 0.10 percent of nonvolatile residue. For other experiments, some of the strontium silicates were used as starting materials. The materials were mixed in the desired proportions, and a small quantity (usually about a gram), together with 1 to 2 ml H_2O, was placed in a small platinum crucible supported in a pressure bomb containing sufficient water to maintain a liquid phase at the desired temperature. The bomb was then kept in a controlled furnace for a period of several days. After the warming-up period, the maximum deviation from the reported temperature was about ±2° C. Upon removal from the furnace, the bomb was allowed to cool in front of a fan for about half an hour. Because of the slowness of the reactions, no significant changes are believed to have occurred during this cooling period.

4.2. Results of Hydrothermal Experiments

a. General

Table 2 gives the results of a number of hydrothermal experiments, selected to present the essential information. Confirmatory or supporting data have been omitted in the interest of brevity. The experiments are tabulated in the order of increasing basicity of reacting mixture, and will be discussed in that order. There are certain observations, however, that apply to the study as a whole.

TABLE 2. *Results of hydrothermal experiments in the system* SrO-SiO_2-H_2O

Expt. No.	Starting material [1]		Temperature	Time	Product
			°C	Days	
1	$1Sr(OH)_2{\cdot}8H_2O+8SiO_2$	(II)	150	7	$SiO_2{\cdot}nH_2O$; $3SrO{\cdot}2SiO_2{\cdot}4H_2O$; $SrO{\cdot}SiO_2$.
2			183	7	$SiO_2{\cdot}nH_2O$; $SrO{\cdot}2SiO_2{\cdot}H_2O$.
3			214	7	Cristobalite; $SrO{\cdot}2SiO_2{\cdot}H_2O$.
4			274	7	Do.
5	$1Sr(OH)_2{\cdot}8H_2O+5SiO_2$	(II)	216	6	Do.
6	$1Sr(OH)_2{\cdot}8H_2O+4SiO_2$	(II)	196	6	Do.
7			149	9	$3SrO{\cdot}2SiO_2{\cdot}4H_2O$; $SiO_2{\cdot}nH_2O$.
8	$1Sr(OH)_2{\cdot}8H_2O+3SiO_2$	(II)	202	6	$SrO{\cdot}2SiO_2{\cdot}H_2O$; cristobalite; $SrO{\cdot}SiO_2$.
9			255	9	$SrO{\cdot}2SiO_2{\cdot}H_2O$; cristobalite.
10			280	9	Do.
11	$2Sr(OH)_2{\cdot}8H_2O+5SiO_2$	(II)	196	6	$SrO{\cdot}2SiO_2{\cdot}H_2O$; cristobalite; $SrO{\cdot}SiO_2$.
12			300	6	Do.
13	$1Sr(OH)_2{\cdot}8H_2O+2SiO_2$	(II)	134	6	$3SrO{\cdot}2SiO_2{\cdot}4H_2O$; $SiO_2{\cdot}nH_2O$.
14		(II)	150	7	Do.
15		(IV)	160	7	$SrO{\cdot}2SiO_2{\cdot}H_2O$; $SrO{\cdot}SiO_2$; $SiO_2{\cdot}nH_2O$.
16		(II)	173	7	Do.
17		(II)	183	7	$SrO{\cdot}2SiO_2{\cdot}H_2O$; $SrO{\cdot}SiO_2$; cristobalite.
18		(III)	200	7	$SrO{\cdot}2SiO_2{\cdot}H_2O$; $SrO{\cdot}SiO_2$.
19		(II)	255	10	$SrO{\cdot}2SiO_2{\cdot}H_2O$; $SrO{\cdot}SiO_2$; cristobalite.
20		(II)	298	6	Do.
21		(II)	368	7	$SrO{\cdot}SiO_2$; quartz.
22	$2Sr(OH)_2{\cdot}8H_2O+3SiO_2$	(II)	126	7	$3SrO{\cdot}2SiO_2{\cdot}4H_2O$; $SiO_2{\cdot}nH_2O$.
23			159	7	$SrO{\cdot}2SiO_2{\cdot}H_2O$; $SrO{\cdot}SiO_2$.
24			247	7	Do.
25	$1Sr(OH)_2{\cdot}8H_2O+1SiO_2$	(II)	110	4	$3SrO{\cdot}2SiO_2{\cdot}4H_2O$; $SiO_2{\cdot}nH_2O$.
26		(I)	114	6	Do.
27		(IV)	120	4	$3SrO{\cdot}2SiO_2{\cdot}3H_2O$; $3SrO{\cdot}2SiO_2{\cdot}4H_2O$; $SiO_2{\cdot}nH_2O$.
28		(I)	123	5	$3SrO{\cdot}2SiO_2{\cdot}4H_2O$; $SiO_2{\cdot}nH_2O$.
29		(I)	128	13	$SrO{\cdot}SiO_2{\cdot}H_2O$; $SrO{\cdot}SiO_2$.
30		(II)	130	7	$3SrO{\cdot}2SiO_2{\cdot}4H_2O$; $SiO_2{\cdot}nH_2O$.
31		(III)	130	6	$3SrO{\cdot}2SiO_2{\cdot}4H_2O$; $SiO_2{\cdot}nH_2O$.
32		(I)	135	7	$SrO{\cdot}SiO_2{\cdot}H_2O$; $SrO{\cdot}SiO_2$.
33	$1Sr(OH)_2{\cdot}8H_2O+1SiO_2$	(II)	135	7	$SrO{\cdot}SiO_2{\cdot}H_2O$; $SrO{\cdot}SiO_2$; $3SrO{\cdot}2SiO_2{\cdot}4H_2O$ (trace).
34		(IV)	135	5	$3SrO{\cdot}SiO_2{\cdot}2H_2O$; $SiO_2{\cdot}nH_2O$.
35		(II)	136	7	$3SrO{\cdot}2SiO_2{\cdot}4H_2O$; $3SrO{\cdot}2SiO_2{\cdot}3H_2O$; $SiO_2{\cdot}nH_2O$.
36		(II)	137	6	$3SrO{\cdot}2SiO_2{\cdot}4H_2O$; $SiO_2{\cdot}nH_2O$.
37		(III)	142	6	$8SrO{\cdot}SiO_2$.
38		(I)	220	8	Do.
39	$8SrO{\cdot}SiO_2$		132	7	Do.
40	$3Sr(OH)_2{\cdot}8H_2O+2SiO_2$	(III)	122	5	$3SrO{\cdot}2SiO_2{\cdot}4H_2O$.
41		(I)	128	5	Do.
42		(III)	133	6	$3SrO{\cdot}2SiO_2{\cdot}4H_2O$; $3SrO{\cdot}2SiO_2{\cdot}3H_2O$.
43		(II)	138	5	$3SrO{\cdot}2SiO_2{\cdot}4H_2O$.
44		(II)	143	6	$3SrO{\cdot}2SiO_2{\cdot}4H_2O$; $2SrO{\cdot}SiO_2$.
45		(III)	145	6	$3SrO{\cdot}2SiO_2{\cdot}4H_2O$; $3SrO{\cdot}2SiO_2{\cdot}3H_2O$; $SrO{\cdot}SiO_2{\cdot}H_2O$.
46		(III)	152	7	$8SrO{\cdot}SiO_2$; $8SrO{\cdot}SiO_2{\cdot}H_2O$; $2SrO{\cdot}SiO_2$.
47		(II)	159	6	$8SrO{\cdot}SiO_2$; $2SrO{\cdot}SiO_2$.
48		(II)	248	5	Do.
49	$3SrO{\cdot}2SiO_2{\cdot}4H_2O$		126	2	$3SrO{\cdot}2SiO_2{\cdot}4H_2O$.
50			132	3	$3SrO{\cdot}2SiO_2{\cdot}4H_2C$; $3SrO{\cdot}2SiO_2{\cdot}3H_2O$.
51			134	4	$3SrO{\cdot}2SiO_2{\cdot}3H_2O$.
52			143	3	Do.
53			161	4	$3SrO{\cdot}2SiO_2{\cdot}3H_2O$; $2SrO{\cdot}SiO_2$.
54			174	4	$3SrO{\cdot}2SiO_2{\cdot}3H_2O$; $2SrO{\cdot}SiO_2$; $SrO{\cdot}SiO_2$.
55	$3SrO{\cdot}2SiO_2{\cdot}3H_2O$		106	3	$3SrO{\cdot}2SiO_2{\cdot}3H_2O$.
56			124	7	$2SrO{\cdot}2SiO_2{\cdot}3H_2O$; $SrO{\cdot}SiO_2$.
57			138	7	$8SrO{\cdot}SiO_2{\cdot}H_2O$; $SrO{\cdot}SiO_2$.
58			142	6	$8SrO{\cdot}SiO_2$; $3SrO{\cdot}2SiO_2{\cdot}3H_2O$.
59			164	7	$2SrO{\cdot}SiO_2$; $SrO{\cdot}SiO_2$.
60			250	7	Do.
61	$2Sr(OH)_2{\cdot}8H_2O+1SiO_2$	(I)	113	13	$3SrO{\cdot}2SiO_2{\cdot}4H_2O$; $Sr(OH)_2{\cdot}8H_2O$.
62		(I)	121	5	$3SrO{\cdot}2SiO_2{\cdot}4H_2O$; $3SrO{\cdot}2SiO_2{\cdot}3H_2O$; $Sr(OH)_2{\cdot}8H_2O$.
63		(III)	131	6	Do.
64		(IV)	136	8	$3SrO{\cdot}2SiO_2{\cdot}3H_2O$; $3SrO{\cdot}SiO_2{\cdot}2H_2O$; $Sr(OH)_2{\cdot}8H_2O$.
65		(II)	138	6	$3SrO{\cdot}2SiO_2{\cdot}4H_2O$; $Sr(OH)_2{\cdot}8H_2O$.
66		(I)	138	13	$2SrO{\cdot}SiO_2{\cdot}H_2O$.
67		(IV)	140	8	$3SrO{\cdot}2SiO_2{\cdot}3H_2O$; $3SrO{\cdot}SiO_2{\cdot}2H_2O$; $Sr(OH)_2{\cdot}8H_2O$.
68		(III)	145	6	$2SrO{\cdot}SiO_2{\cdot}H_2O$; $3SrO{\cdot}2SiO_2{\cdot}3H_2O$; $2SrO{\cdot}SiO_2$.
69		(III)	156	6	$2SrO{\cdot}SiO_2$.
70		(II)	256	9	Do.
71	$2SrO{\cdot}SiO_2$		140	7	Do.
72	$5Sr(OH)_2{\cdot}8H_2O+2SiO_2$	(III)	132	13	$2SrO{\cdot}SiO_2{\cdot}H_2O$; $3SrO{\cdot}2SiO_2{\cdot}3H_2O$; $Sr(OH)_2{\cdot}8H_2O$.
73	$3Sr(OH)_2{\cdot}8H_2O+1SiO_2$	(II)	118	4	$3SrO{\cdot}SiO_2{\cdot}2H_2O$; $3\ SrO{\cdot}2SiO_2{\cdot}4H_2O$; $Sr(OH)_2{\cdot}8H_2O$.
74		(III)	135	7	$2SrO{\cdot}SiO_2{\cdot}H_2O$; $3SrO{\cdot}SiO_2{\cdot}2H_2O$; $Sr(OH)_2{\cdot}8H_2O$.
75		(II)	142	4	$3SrO{\cdot}SiO_2{\cdot}2H_2O$; $2SrO{\cdot}SiO_2$; $Sr(OH)_2{\cdot}8H_2O$.
76		(II)	158	7	$3SrO{\cdot}SiO_2{\cdot}2H_2O$; $2SrO{\cdot}SiO_2$.
77		(II)	183	4	$3SrO{\cdot}SiO_2{\cdot}2H_2O$; $2SrO{\cdot}SiO_2$.
78		(II)	247	4	$2SrO{\cdot}SiO_2$; little unidentified material.
79		(II)	304	4	Do.
80	$4Sr(OH)_2{\cdot}8H_2O+1SiO_2$	(III)	136	5	$3SrO{\cdot}SiO_2{\cdot}2H_2O$; $Sr(OH)_2{\cdot}8H_2O$.

[1] Roman numerals indicate the particular lot of silica gel used: (I) Reagent silicic acid, (II) A commercial gel of high fineness and low purity, (III) A commercial gel of medium fineness and purity, (IV) A rather coarse gel of high purity.

The system was found to be rather complex. In addition to the 2 hydrated silicates described above, 5 new compounds were observed. All have been tentatively assigned formulas, but the compositions of some are not definitely established. This is due to the failure to obtain pure preparations. It may be that some of the compounds are metastable under all conditions, and have only a transitory existence.

Another notable aspect of the system is that the hydrated compounds occur only at relatively low temperatures. It is noteworthy that anhydrous compounds were formed hydrothermally at tempera-

mes as low as 124°, and that most of the hydrates decomposed below 150°. Because of the narrow range of stability, relatively small fluctuations in temperature or in rate of heating may have affected the results.

It will be noted that the results are not always in accord. Different products are sometimes obtained under apparently identical conditions. It was observed that different types of silica may give different results. For example, the compound $3SrO{\cdot}SiO_2{\cdot}2H_2O$ appeared unexpectedly in a 2:1 mixture (experiment 64) in which the relatively coarse-grained silica gel IV was used. In this case it may be assumed that the low reactivity of the silica resulted in a temporary excess of strontium hydroxide above the calculated ratio. In other cases the differences are harder to explain. The type of silica used in each case is recorded in the table, although no attempt was made to study their differences systematically.

At temperatures slightly above 100°, the primary reaction product in all cases appeared to be $3SrO{\cdot}2SiO_2{\cdot}4H_2O$, irrespective of the proportion in which the oxides were present. Crystals having the same distinctive shape were frequently observed in reaction products that had been held at much higher temperatures, but it was found by X-ray diffraction and refractive index determinations that these had undergone decomposition without losing their over-all appearance. It must be assumed that the hydrate was formed initially, possibly during the warming-up period, and subsequently was decomposed at the higher temperatures.

Anhydrous strontium metasilicate ($SrO{\cdot}SiO_2$) and orthosilicate ($2SrO{\cdot}SiO_2$) were formed at temperatures as low as 124° and 142°, respectively. In general, there was evidence of intermediate formation of one or more of the hydrates, but the metasilicate occasionally appeared in the form of spherical aggregates, as if it had formed directly at the surface of the silica grains. More often it occurred as well-defined tabular crystals of hexagonal shape, as shown in figure 3. These were found to be optically biaxial, with a very small optic axial angle. The compound thus is shown to be pseudohexagonal, as suggested by Eskola [2].

The rest of the products were obtained over a narrower range of oxide ratio in the reaction mixture, and will be considered in the following sections in relation to that ratio.

b. Mixtures Less Basic Than $1SrO:1SiO_2$

Hydrothermal treatment of mixtures ranging in $SrO:SiO_2$ ratio from 1:8 to 2:3 initially produced the 3:2:4 hydrate. Continued treatment resulted in anhydrous $SrO{\cdot}SiO_2$, together with an unknown compound. In the highly siliceous mixtures the excess silica was converted to cristobalite above 180°, and to quartz in one case at 368°. The new compound was first detected by means of its X-ray diffraction pattern. It was subsequently observed under the microscope in the form of extremely fine, round, nearly isotropic grains, usually in relatively

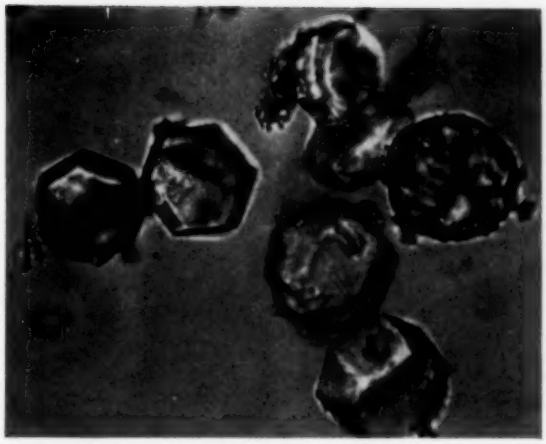

FIGURE 3. *Crystals of* $SrO{\cdot}SiO_2$, *formed under hydrothermal conditions.*

Magnification, ×700.

large aggregates. The mean index of refraction appeared to be about 1.574, but this figure is subject to considerable uncertainty. Many of the grains seemed to have a much lower index, but this is believed to have been due to a shell of cristobalite surrounding a core of the silicate. The existence of solid solution appears unlikely in view of the constancy of the X-ray pattern.

Because the new compound was not obtained pure, it was necessary to arrive at its composition indirectly. Mixtures of $1SrO:2SiO_2$ yielded the new phase together with small amounts of both cristobalite and $SrO{\cdot}SiO_2$. Increasing the strontium to a ratio $2SrO:3SiO_2$ resulted in the new phase plus $SrO{\cdot}SiO_2$ but no cristobalite, indicating that the compound in question is richer in SiO_2 than the reaction mixture. For mixtures more siliceous than $1SrO:2SiO_2$, the results are less easy to interpret. $SrO{\cdot}SiO_2$ appeared in 1:3 mixtures, and even in one instance in a 1:8 mixture, at 150°. Bearing in mind the fact mentioned above, that the hydrate $3SrO{\cdot}2SiO_2{\cdot}4H_2O$ is formed initially even in the highly siliceous mixtures, it is possible that the subsequent decomposition of this hydrate leads most readily to the formation of the anhydrous metasilicate. The latter is known to be relatively stable and, once formed, would have little tendency to react further; hence, it might occur in compositions far removed from a 1:1 ratio. Both cristobalite and $SrO{\cdot}SiO_2$ were formed in small amounts from the $2SrO:5SiO_2$ mixtures, but the proportion of cristobalite was estimated to be higher than that of the $SrO{\cdot}SiO_2$. Thus the ratio for the new compound appears to lie between 2:5 and 2:3; it is therefore assumed to be 1:2. Ignition loss determinations on several preparations indicated an average content of about 0.7 mole of water. Allowing for the anhydrous impurities present, the new compound is thus believed to have the composition $SrO{\cdot}2SiO_2{\cdot}H_2O$.

c. Molar Ratio 1SrO:1SiO_2

Equimolar mixtures of strontium hydroxide and silica gel, like the more highly siliceous mixtures, reacted to form $3SrO{\cdot}2SiO_2{\cdot}4H_2O$ at the lowest temperatures used (110° to 114°). At 142°, and higher, the reaction product was always the anhydrous metasilicate, $SrO{\cdot}SiO_2$. At intermediate temperatures, the nature of the product appeared to depend on the type of silica gel used, but the results were not always consistent even with a single type of gel. For example, table 2, experiments 30, 35, and 36, reveals that both $3SrO{\cdot}2SiO_2{\cdot}4H_2O$ and $3SrO{\cdot}2SiO_2{\cdot}3H_2O$ were formed at 136° but only the former at 130° and 137° in mixtures containing gel II. The trihydrate was formed from gel IV at 120° (experiment 27), but not from gel I at any temperature. The formation of the highly basic compound, $3SrO{\cdot}SiO{\cdot}2H_2O$, in experiment 34 has already been mentioned.

In experiments 29, 32, and 33 a new phase appeared. This consisted of minute flakes with low birefringence and a mean index of 1.604. Repeated efforts to produce this compound reasonably free from other phases met with failure. The best preparation, No. 33, contained 0.99 mole of H_2O per mole of $SrO{\cdot}SiO_2$, while No. 32, with a higher proportion of anhydrous material, contained 0.74 mole of H_2O. On the basis of this meager evidence the formula $SrO{\cdot}SiO_2{\cdot}H_2O$ has been assigned to this compound. The X-ray pattern is given in table 1.

Treatment of anhydrous $SrO{\cdot}SiO_2$ at 132° left the material apparently unchanged, although this is within the temperature range in which the various hydrates were formed from the hydrated oxides.

d. Molar Ratio 3SrO:2SiO_2

Mixtures of strontium hydroxide and silica gel in 3:2 ratio reacted as did the equimolar mixtures, except that the increase in SrO resulted in the formation of the anhydrous orthosilicate, $2SrO{\cdot}SiO_2$, at the higher temperatures. This compound always appeared as irregular masses of small particles, often pseudomorphic after $3SrO{\cdot}2SiO_2{\cdot}4H_2O$. Unlike the metasilicate, it was never found as well-defined crystals. In this, as in the preceding series, the results within a small temperature range are varied and inconsistent.

In two series of experiments the starting materials were the 3:2:4 and 3:2:3 hydrates described above. From the results in table 2, it may be seen that the 3:2:4 hydrate was converted to the trihydrate at temperatures of 132° C and higher. For reasons unknown, this result was not consistently obtained from mixtures of the hydrated oxides in the same molar ratio. At 161° and above, anhydrous compounds were formed.

The trihydrate behaved differently in that two additional hydrates were formed, at 124° and 138°, respectively. In the latter case, the compound was $SrO{\cdot}SiO_2{\cdot}H_2O$, described in the previous section. The new phase formed at 124° proved to be very elusive. It was obtained in small amounts in a few other experiments not included in the table, but never free of other phases. It appeared in the form of very fine needles with an average refractive index about 1.60. It could be distinguished from $SrO{\cdot}SiO_2{\cdot}H_2O$ only by its X-ray diffraction pattern (see table 1). Although this compound was not obtained hydrothermally sufficiently pure for chemical analysis, a preparation obtained at a lower temperature, by a method to be described later, was found to have the following oxide ratio: $SrO:SiO_2:H_2O = 0.96:1:1.44$. The formula $2SrO{\cdot}2SiO_2{\cdot}3H_2O$ is suggested as a possibility on the basis of this analysis.

It is worthy of note that although the 3:2:4 hydrate was converted to the 3:2:3 by raising the temperature to 132° or higher, the reverse reaction was not obtained by holding the 3:2:3 hydrate at 106° (experiment 55).

e. Molar Ratio 2SrO:1SiO_2 and 5SrO:2SiO_2

An increase in SrO to the 2:1 ratio gave rise to two new hydrated compounds. One of these, the tristrontium compound, will be discussed in the next section. The other appeared, along with other crystalline products, at 132° to 148° C. Analyses of preparations 66 and 72, which appeared to be most nearly homogeneous, gave the following molar ratios, respectively: $SrO:SiO_2:H_2O = 1.86:1:0.98$ and 1.86:1:1.09. The formula $2SrO{\cdot}SiO_2{\cdot}H_2O$ fits the data reasonably well.

This compound occurred as small lath-shaped crystals, with parallel extinction and negative elongation. It is biaxial positive in character, with low and high indices of 1.638 and 1.641, respectively. The X-ray powder diffraction pattern is given in table 1.

At 156° and above, the anhydrous orthosilicate, $2SrO{\cdot}SiO_2$, was formed. Attempts to reverse the reaction by holding the anhydrous compound at 140° and below were unsuccessful.

f. Molar Ratio 3SrO:1SiO_2 and Higher

Mixtures of strontium hydroxide and silica gel in 3:1 ratio produced a new compound that has been referred to in the previous section. As in the case of the other hydrothermal preparations, it was always contaminated with one or more other phases. Analyses of three preparations gave the following $SrO:SiO_2:H_2O$ ratios: No. 76, 2.9:1:2.2; No. 75, 2.7:1:1.7; No. 80, 3.1:1:2.7. The first of these preparations contained a small amount of $2SrO{\cdot}SiO_2$, the second somewhat more. The third was prepared from an original 4:1 mixture and contained a small amount of $Sr(OH)_2{\cdot}8H_2O$, which probably accounts for the higher H_2O content. On the basis of these analyses, it is concluded that the compound has the composition $3SrO{\cdot}SiO_2{\cdot}2H_2O$. It was observed as very thin needles or plates (see fig. 1), often joined in spherulites. They were birefringent, with indices $\alpha = 1.575$, $\gamma = 1.595$, and showed parallel extinction and positive elongation. The X-ray diffraction pattern given in table 1 is a composite of five patterns on different preparations.

This hydrate was formed together with $3SrO{\cdot}2SiO_2{\cdot}4H_2O$ at 118° C. At higher temperatures the less basic hydrate was changed to the anhydrous $2SrO{\cdot}SiO_2$, which frequently retained the peculiar shape of the original crystals. The tristrontium compound was formed at temperatures as high as 183°, but at 247° and above only $2SrO{\cdot}SiO_2$ could be identified.

A sample of the tristrontium silicate hydrate, after being heated to 1,200°, was found to have decomposed to $2SrO{\cdot}SiO_2$ and SrO.

5. Action of Water on the Strontium Silicates

The behavior of the various strontium silicates in the presence of water was not studied thoroughly in this investigation, but because of the possibility of hydraulic properties [7] it was considered desirable to make a few exploratory tests.

A small quantity of the anhydrous metasilicate, $SrO{\cdot}SiO_2$, was mixed with enough water to form a paste, which was then packed into a vial and allowed to stand in a moist atmosphere for several days. No evidence of setting was observed. The orthosilicate, $2SrO{\cdot}SiO_2$, behaved in the same manner, the only difference being that it became warm immediately on mixing with water. This may have been due to the presence of a little uncombined SrO in the preparation used. This experiment fails to support the statement of Zhuravlev [7] that $2SrO{\cdot}SiO_2$ possesses hydraulic properties. Negative results were likewise obtained when the pastes were kept at steam-bath temperature. Subsequent microscopic examination failed to reveal any change in appearance. As shown in table 2, the anhydrous silicates also were unaffected by water at temperatures just below those at which they are formed hydrothermally.

The two anhydrous silicates were likewise unaltered after being shaken with an excess of water and allowed to stand 3 days at room temperature. Titration of the filtrates showed that a little strontium hydroxide had gone into solution, but the concentration was far less than the solubility of pure $Sr(OH)_2$ at the same temperature.

A single solubility test at 30° C was made on each of the two hydrated silicates that were produced by boiling; namely, $3SrO{\cdot}2SiO_2{\cdot}4H_2O$ and $3SrO{\cdot}2SiO_2{\cdot}3H_2O$. The strontium hydroxide concentration was determined by titration after 1 day, and gravimetrically at the end of 10 weeks. There was no significant difference between the two values. The tetrahydrate residue was apparently unchanged during this period, and was in equilibrium with solution containing 0.745 g of SrO and 0.304 g of SiO_2 per liter. For the purpose of comparison, the solubility of strontium hydroxide at the same temperature is about 10 g of SrO per liter. The trihydrate gave a solution of almost the same concentration, namely, 0.762 g of SrO and 0.303 g of SiO_2 per liter, but in this case the solid residue had been partially converted to the compound tentatively designated $2SrO{\cdot}2SiO_2{\cdot}3H_2O$, and the $SrO{:}SiO_2$ ratio in the residue had fallen to 1.26. Another sample of the trihydrate, kept in contact with water on the steam bath for 10 weeks, was completely converted to the same compound. The analysis of this material was the basis for the proposed formula. Progress of the transition was manifested by a curling of the acicular crystals, some of which developed a helical shape, as seen under the microscope.

The glass containers used for the solubility experiments were strongly attacked by the solution, especially at steam-bath temperature. This probably is the source of the additional silica required for the change from the 3:2:3 to the 2:2:3 compound.

6. Relationship Between the Silicates of Strontium and Calcium

It is of interest to consider possible relationships between the hydated silicates of strontium and those of calcium. The latter have been studied extensively by a number of investigators, including Flint, McMurdie and Wells [8], and the subject has recently been reviewed thoroughly by Taylor and Bessey [9].

If the oxide formulas of the strontium silicate hydrates described above are compared with a list of the reported calcium silicate hydrates, analogs will be noted for the 1:1:1, 2:2:3, 3:2:3, 2:1:1, and 3:1:2 compounds. Whether any of these are actually isomorphous cannot be known without an analysis of the crystal structure. Visual comparison of the X-ray patterns of $3SrO{\cdot}2SiO_2{\cdot}3H_2O$ and $3CaO{\cdot}2SiO_2{\cdot}3H_2O$ (afwillite) reveals considerable similarity. The refractive indices, birefringence, and crystal form also indicate the possibility of a relationship between these two compounds. To a lesser extent, resemblances may be observed between the compound designated $2SrO{\cdot}2SiO_2{\cdot}3H_2O$ and the mineral crestmoreite, for which the formula $2CaO{\cdot}2SiO_2{\cdot}3H_2O$ has been given [8]. On the basis of refractive indices alone, it appears possible that the 1:1:1 and 3:1:2 strontium silicates may be related to the corresponding calcium silicates reported by Flint, McMurdie, and Wells [8]. In the case of the 2:1:1 compounds, the relationship, if any, is probably with the calcium silicate having a refractive index of 1.64, sometimes designated the γ-hydrate. In these cases the data on crystal form are lacking, and the X-ray patterns are too complex for superficial comparison.

7. Summary

Hydrothermal treatment of mixtures of strontium hydroxide and silica gel in various proportions and at various temperatures produced seven hydrated strontium silicates, as well as the anhydrous meta- and orthosilicates. Table 3 gives the probable compositions of the hydrates, and their optical properties, so far as the latter could be determined. The X-ray powder diffraction patterns, together with that of $SrO{\cdot}SiO_2$, are given in table 1. Formulas given for the compounds having the oxide ratios 3:2:3 and 3:2:4 are believed to be correct, and the 2:1:1 and 3:1:2 formulas probably are correct,

TABLE 3. *Some optical properties of the strontium silicate hydrates*

Composition	Refractive indices			Character	Sign	Elongation	Crystal habit
	α	β	γ				
$SrO \cdot 2SiO_2 \cdot H_2O$	.....	1.574	.....	.....	.....	.....	Round grains.
$SrO \cdot SiO_2 \cdot H_2O$	.....	1.604	.....	.....	.....	.....	Irregular flakes.
$2SrO \cdot 2SiO_2 \cdot 3H_2O$	.....	1.60	.....	.....	.....	.....	Irregular.
$3SrO \cdot 2SiO_2 \cdot 3H_2O$	1.602	1.602	1.614	Biaxial	+	−	Flat prisms.
$3SrO \cdot 2SiO_2 \cdot 4H_2O$	1.595	.....	1.627	do	+	.....	Dendritic.
	1.617	.....	1.637				
$2SrO \cdot SiO_2 \cdot H_2O$	1.638	.....	1.641	do	+	−	Lath-shaped prisms.
$3SrO \cdot SiO_2 \cdot 2H_2O$	1.575	.....	1.595	.....	.....	+	Needles or plates.

while the other 3 are somewhat in doubt. Both anhydrous compounds were formed hydrothermally at temperatures below 150°. The hydrates $3SrO \cdot 2SiO_2 \cdot 3H_2O$ and $3SrO \cdot 2SiO_2 \cdot 4H_2O$ were prepared at boiling temperature as well as under hydrothermal conditions.

The anhydrous silicates did not appear to be strongly attacked by water, and no evidence of hydraulic binding properties was found.

The X-ray patterns and photomicrographs were prepared by Barbara Sullivan and G. M. Ugrinic, thermal analyses were made by E. S. Newman, and many of the chemical analyses were performed by T. J. Chaconas. The writers are indebted to these people for their valuable assistance.

8. References

[1] E. P. Flint, H. F. McMurdie, and L. S. Wells, J. Research NBS **26,** 13 (1941) RP1355.
[2] P. Eskola, Am. J. Sci. [5] **4,** 331 (1922).
[3] H. O'Daniel and L. Tscheischwili, Z. Krist. **104,** 348 (1942).
[4] R. Nacken, Zement **19,** 818, 847 (1930).
[5] R. W. Nurse, J. Applied Chem. **2,** 244 (1952).
[6] E. Jordis and E. H. Kantner, Z. anorg. Chem. **35,** 82 (1903).
[7] V. F. Zhuravlev, Tsement, No. 8, 41 (1939).
[8] E. P. Flint, H. F. McMurdie, and L. S. Wells, J. Research NBS **21,** 617 (1938) RP1147.
[9] H. F. W. Taylor and G. E. Bessey, Mag. Concrete Research (London) No. 4, 15 (1950).

WASHINGTON, May 21, 1953.

Journal of Research of the National Bureau of Standards Vol. 51, No. 2, August 1953 Research Paper 2434

Ultraviolet Spectral Radiant Energy Reflected From the Moon

Ralph Stair and Russell Johnston

Results are given of some measurements on the ultraviolet and short-wavelength visible spectral radiant energy reflected from the surface of the full moon, made from October to December 1952, at Washington, D. C. Although the reflected lunar spectrum contains all the Fraunhofer bands as found in direct sunlight with approximately the same relative intensities in the visible spectrum, intense absorption occurs for some of the ultraviolet wavelengths. Selective absorption for wavelengths in the spectral regions of 380 to 390 millimicrons and less than 360 millimicrons indicates the possibility of a lunar reflecting surface similar to that of powdered glassy silicates.

1. Introduction

Man has long speculated about the moon—its origin, its surface features, and its path in space. This interest has stimulated the search for facts regarding the exact nature and origin of the surface panorama visible through the telescope.

It is, however, generally agreed that the lunar surface features have been sculptured by catastrophic agents (either meteoric or volcanic, or both) [1 to 10, inclusive].[1] The resulting surface features differ greatly from anything on the earth, except for a certain resemblance to the few known terrestrial meteor craters. Because gravity on the moon is only about one-sixth that on the earth and there is an absence of an atmosphere, the lunar craters are probably 25 to 50 times as large [11] as would result on the earth.

As the result of the absence of an atmosphere and moisture and, hence, of the usual types of weathering and erosion, the moon has retained records of many of its early catastrophic experiences. During its history about 16 times as many meteorites have collided with the earth, but their records have been largely erased [1], unless we conclude that the encounters with the larger ones resulted in some of the geologic transitions indicated by abrupt changes between certain layers of the earth's strata.

The surface of the moon does change, however. It is affected by the sun's rays, by gravity, and by tidal forces, by the temperature change from about 250° F [15 to 18, inclusive] during the lunar day to about −150° F during its night, and by attrition due to falling meteorites, estimated at over one million per day [2]. These effects combine to produce a pulverization of the surface layer, which acts as the efficient insulating surface indicated by the character of the temperature changes on the moon's surface observed during solar eclipses [19].

The blackening of the old surface areas, or "maria", may be due in part to exposure of the surface materials to high frequency (short wavelength) radiant energy. Oxygen, ozone, and other components of the earth's atmosphere act as a blanket that prevents the earth from receiving ultraviolet and other solar radiant energy of wavelengths shorter than about 295 mμ. Laboratory experiments show that many crystalline and glassy substances on the earth darken upon exposure to wavelengths within the spectral range incident on the moon. The collection of a thin layer of fine meteoric material containing iron and other dark substances may be expected also to darken the lunar surface.

The study of the moon through measurement of its effect upon reflected sunlight may be approached from several angles: through changes in intensity or polarization [11 to 14, inclusive] of the reflected radiant energy as a function of the angle of incidence, or through changes in the reflected spectrum caused by the lunar surface. This report deals with the integrated ultraviolet spectral intensities reflected for the fixed angular incidences corresponding to near full moon and with the moon near its most northern position in the sky.

The observed relative spectral distribution of ultraviolet radiant energy reflected from the moon is very similar in quality to that emitted by the sun itself. All the Fraunhofer lines appear and with approximately the same relative intensities. Any differences in the two spectra result from selective optical absorption by the lunar surface. Except for a slight yellowing of the lunar image and for variations in the ultraviolet and visible spectrum over its surface features [20], nothing has been reported in the available literature noting any other differences between the two spectra.

2. Instruments and Procedure

The apparatus employed in this investigation consists of a Carl Leiss double quartz-prism mirror spectrometer, using an RCA 1P28 photomultiplier as a detector. The light beam is modulated at 510 c/s, and the output of the photomultiplier is fed into a tuned amplifier [21] and recorder (see fig. 1). A siderostat was employed for reflecting the beam of light from the moon into the spectroradiometer in a manner similar to that previously used with sunlight [22].

No condensing lens or mirror was employed, so that the resultant measurement was that for the integrated surface of the moon. The spectral-energy-response characteristic of the complete instrument, including the siderostat and photomultiplier, was determined by using a special tungsten-filament-in-quartz lamp [21, 23], together with a number of optical filters to reduce the lamp energy for the various parts of the spectrum (see fig. 2) to values approximating that of the moonbeam at the spectrometer slit. The radiant energy from the

[1] Figures in brackets indicate the literature references at the end of this paper.

lamp was reflected into the spectrometer by the same siderostat mirrors, so that the spectral energy calibration for the moonbeam reduced to a simple comparison of the recorder indications in the two cases.

The high sensitivity of the detecting and recording equipment permitted the use of relatively narrow slit widths (spectral width approximately 1 mμ at 310 mμ and 2 to 3 mμ at longer wavelengths). These values are comparable to those employed in previous work with sunlight [24], so that the Fraunhofer structure of the measured radiant energy in the two cases is quite similar (see fig. 5), although different spectroradiometers were employed.

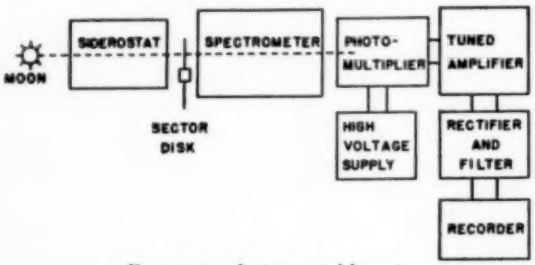

FIGURE 1. *Instrumental layout.*

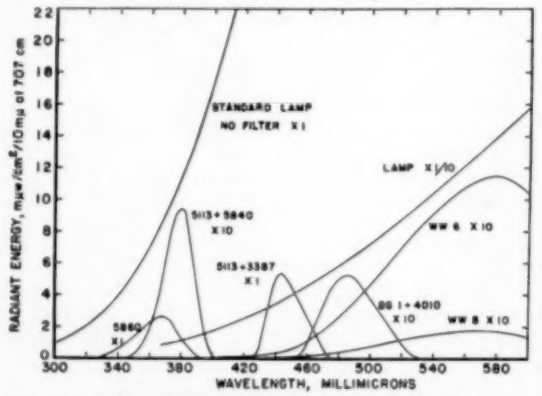

FIGURE 2. *Spectral energy distribution of the standard lamp through the filters used in the calibration of the instrument.*

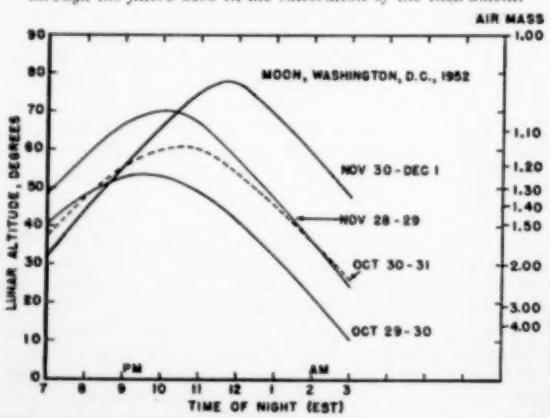

FIGURE 3. *Changes in air mass for the ascent and descent of the moon for the different evenings.*

Measurements were made during four nights near the ends of October and November 1952, when the moon was near its full phase and also near its maximum northern position, hence near its highest altitude at the latitude of Washington, D. C. The best data were obtained during the night of November 30–December 1, when the moon was not only nearest its full phase but was also at the highest altitude for any night during the series of measurements. Also, the atmosphere was entirely free of clouds and showed least dust or haze scattering on this night. Data on the lunar altitude and air mass for the four nights were calculated in the usual manner by means of the celestial triangle through the use of the pertinent data published in the American Ephemeris and Nautical Almanac for 1952 for the solar and lunar positions. The resulting data are charted in figure 3.

3. Spectral Radiant Energy Reflected From the Moon

The spectral radiant energy reflected from the moon depends upon the optical and other physical characteristics of the lunar surface. Changes in the solar radiant energy are admittedly small [25] for all wavelengths penetrating the terrestrial atmosphere. Variations at the moon as a function of time may be considered insignificant. In view of the fact that previous observers have found a marked variation in the light reflected from the moon as a function of the angles of incidence and reflection [11, 15], a similar behavior might be expected for the ultraviolet rays. However, at present the amount of this effect is unknown. Furthermore, variations in ultraviolet intensities over the lunar surface are known to be appreciable [20]. Future studies for specific areas of the moon and at various angles of incidence and reflection should be interesting and informative.

Terrestrial atmospheric absorption further modifies the lunar reflected radiant energy. Mean spectral values (for ascending and descending moon) for a lunar altitude of 65 degrees (air mass 1.10) are given in figure 4. When spectral radiant energy data are taken over a range of ascending (or descending) positions of the moon and plotted logarithmically [24] as a function of air mass and extrapolated to air mass equals 0, the intercepts represent the logarithms of the spectral intensities outside the terrestrial atmosphere. The data illustrated in figure 5 were obtained in this manner.

In order to illustrate better the similarity between the spectral radiant energy reflected from the moon as compared with that emitted by the sun, the data obtained for the sun at Climax, Colorado, in September 1951, are taken from the previous publication [24] and reproduced in figure 5. Although these data were obtained with different spectroradiometers at different times and places, the similarity in the two curves is striking. This is partly because the dispersions for the two instruments were not appreciably different. However, slight differences re-

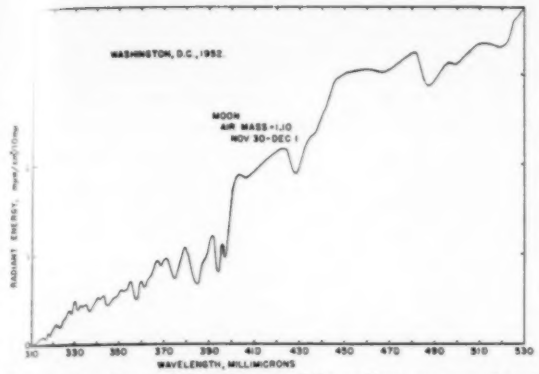

FIGURE 4. *Spectral distribution of the radiant energy reflected from the moon.*

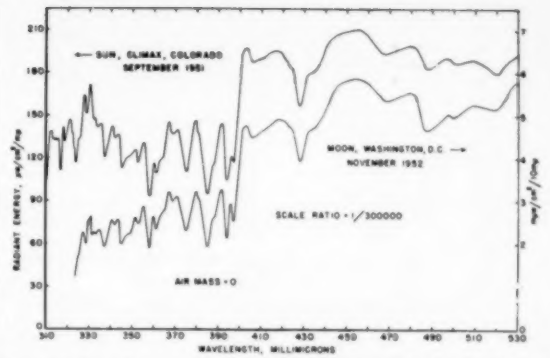

FIGURE 5. *A comparison between the spectral distribution of the radiant energy from the sun and the reflected energy from the moon.*

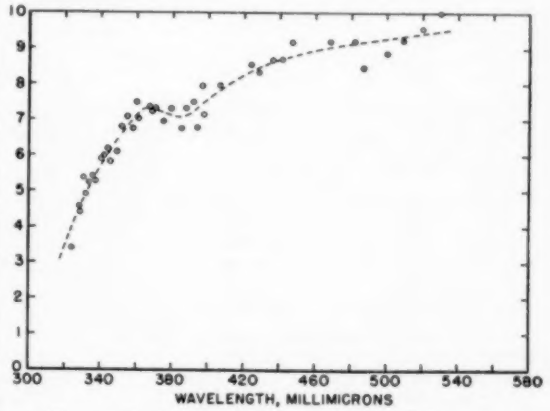

FIGURE 6. *Relative spectral reflectivity of the moon.*

sult in greater scattering of the data plotted in figure 6.

An inspection of the lunar relative to the solar radiant energy curve (fig. 5) discloses greater differences between the two toward the shorter wavelengths. A quantitative plot of this ratio (fig. 6) gives the relative spectral reflectivity of the lunar surface. Much of the scatter of the data, as indicated above, results from slight differences in the dispersions of the two spectroradiometers, inasmuch as a close inspection of the individual plotted points discloses that the higher values result from ratios between peaks on the curves, whereas the lower values are associated with the Fraunhofer absorption bands.

Three important characteristics of this reflectivity curve are worthy of note. First, the curve decreases in ordinate value with wavelength, thus indicating that the lunar surface has a lower reflectivity for the shorter wavelengths. Second, the band at 380 to 390 mμ indicates selective absorption of the lunar surface materials. Third, the sharp cutoff beginning at about 360 mμ may be considered indicative of some special composition.

If the three special characteristics of the lunar reflectivity curve are considered in terms of possible materials present, and other known factors about the moon, such as its albedo, polarization, and heat conductivity are kept in mind, it appears not unlikely that a yellowish glass-like composition could be responsible for the observed phenomena. Certain silica glasses [26] have an ultraviolet cutoff corresponding closely with the observed curve. In a splintered or crushed form they would reflect a measurable amount of radiant energy after transmittance through an appreciable thickness of material. A small iron content would result in selective absorption at 380 to 390 mμ and would give the material a slightly yellowish color. A pulverized glassy silicate lunar surface would be highly insulating and would produce characteristics compatible with temperature measurements obtained during eclipse and with lunar phase changes [15, 16, 19]. The low average albedo [7, 27 to 30, inclusive], about 7.3 percent, corresponds closely to the expected reflectivity from glassy material. Although measurements of the albedo of the moon are not precise, most of them fall below about 12 percent. Hence, the surface of the moon may be composed, at least in part, of powdered glassy silicates. Incidentally, the high percentage of SiO_2 in the earth's crust might suggest the possibility of a terrain similar to that of the moon had not air, water, erosion, etc., been present.

The observations on polarization at the surface of the moon by Wright [12] indicate reflection by a fine texture and "point to pumiceous substances high in silica, to powders of transparent substances and to quartz porphyries and possibly to trachytes and granites as the materials we see at the moon's surface." Similarly, the relative spectral reflectivity curve for the moon obtained in the present investigation points to the possibility that the surface materials are, at least in part, composed of powdered glassy silicates. Further refinements in the observations of this interesting satellite are needed, however, before definitive conclusions can be drawn.

4. Atmospheric transmittance and ozone

The atmospheric transmission curve depicted in figure 7 is plotted in the usual way in terms of the

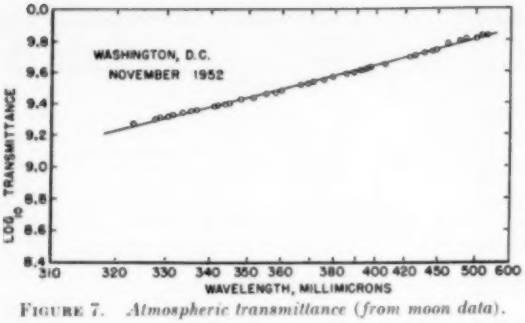

FIGURE 7. *Atmospheric transmittance (from moon data).*

logarithm of the observed transmittances of unit atmosphere (at Washington) for the different wavelengths as a function of the wavelengths. This, in turn, is expanded [31] according to the function $-(\mu-1)^2\lambda^{-4}$ of the Rayleigh law of molecular scattering,

$$\log Tr = -\frac{32\pi^3(\mu-1)^2 H \log e}{3N\lambda^4},$$

in which λ is the wavelength of the radiant energy, and μ is the index of refraction of the atmosphere. Since, for the zenith position the atmospheric depth, H, and the molecular density, N, are constant, the resulting plot of the logarithm of the atmospheric transmittances becomes a straight line in those spectral regions wherein the Rayleigh law of pure molecular scattering is applicable. In as much as appreciable ozone absorption occurs only at wavelengths shorter than about 330 mμ, the data herein recorded are inadequate for use in ozone determinations. Between 300 and 330 mμ (fig. 4), the observed intensities were extremely low and the instrumental noise levels relatively high. With certain improvements in the equipment, it is hoped to reach sensitivities adequate for use of the apparatus in ozone determinations at night. As an alternative, the use of a condensing lens or mirror may be advantageous in supplying sufficient radiant energy from the moon for this purpose.

5. Summary and Conclusions

This report presents the first observed ultraviolet photometric curve of moonlight from data obtained primarily on a single night, although measurements were made on three additional nights when the moon was near its full phase and at high altitudes. Despite the fact that the measurements were made through the dense blanket of atmosphere over a sea-level station, interesting information was obtained having a bearing on the composition of the lunar surface. Further nighttime measurements at higher altitude stations with improved equipment should result in additional information not only on lunar reflectivity but also on ozone concentration.

The extremely high sensitivity of the equipment lends its usefulness in other fields of research, in particular to stellar investigations. With telescopic magnification sufficient radiant energy from many stars, and also from small areas on the moon should be available to permit precise determinations of ultraviolet spectral intensities. Preliminary tests already made of weak fluorescent sources, reflections from dull surfaces, and of radiant energy from small sky areas (even during rainfall or after sundown) indicate a wide range of possible application for the equipment.

6. References

[1] Ralph E. Baldwin, The face of the moon (University of Chicago Press, Chicago, Ill., 1949).

[2] L. J. Spencer, Meteorites and craters on the moon, Nature, **139,** 655 (1937).

[3] R. A. McIntosh, Origin of lunar features, J. Roy. Astronom. Soc. Can. **37,** 24 (1943).

[4] S. J. Hacker and J. Q. Stewart, Lunar ray craters, Astrophys. J. **81,** 37 (1935).

[5] Allan O. Kelly, The geology of the moon, Popular Astron. **55,** 530 (1947).

[6] A. C. Gifford, The mountains of the moon, New Zealand J. Sci. Technol. **7,** 129 (1924).

[7] Henry Norris Russel, Raymond Smith Dugan, and John Quincy Stewart, Astronomy (Ginn & Co., Chicago, Ill., 1926).

[8] Robert H. Baker, Astronomy (D. Van Nostrand Co, New York, N. Y., 1950).

[9] Fred L. Whipple, Earth, moon and planets (Blakiston Co., Philadelphia, Pa., 1941).

[10] W. S. Krogdahl, The astronomical universe (Macmillan Co., New York, N. Y., 1952).

[11] F. E. Wright, The surface features of the moon, Sci. Monthly **40,** 101 (1935).

[12] F. E. Wright, Polarization of light reflected from rough surfaces with special reference to light reflected by the moon, Proc. Nat. Acad. Sci. **13,** 535 (1927).

[13] F. E. Wright, The surface of the moon, Carnegie Inst., Wash., Pub. No. 501, p. 59 (1938).

[14] B. Lyot, Etude des surfaces planetaires par la polarization, Compt. rend. **177,** 1015 (1923).

[15] Edison Pettit, Lunar radiation as related to phase, Astrophys. J. **81,** 17 (1935).

[16] Edison Pettit and Seth B. Nicholson, Lunar radiation and temperature, Astrophys. J. **71,** 102 (1930).

[17] Donald H. Menzel, Water-cell transmissions and planetary temperatures, Astrophys. J. **58,** 65 (1923).

[18] W. W. Coblentz, Further tests of stellar radiometers and some measurements of planetary radiation, BS Sci. Pap. **18,** 535 (1922) S460.

[19] Edison Pettit, Radiation measurements on the eclipsed moon, Contr. Mt. Wilson Obs. No. 627, **26,** 165 (1940).

[20] R. W. Wood, The moon in ultraviolet light, and spectroselenography, Popular Astron. **18,** 67 (1910).

[21] Ralph Stair, Photoelectric spectroradiometry and its application to the measurement of fluorescent lamps, J. Research NBS **46,** 437 (1951) RP2212.

[22] R. Stair and W. O. Smith, A tungsten-in-quartz lamp and its application in photoelectric radiometry, J. Research NBS **30,** 449 (1943) RP1543.

[23] Ralph Stair, Ultraviolet spectral distribution of radiant energy from the sun, J. Research NBS **46,** 353 (1951) RP2206.

[24] Ralph Stair, Ultraviolet radiant energy from the sun observed at 11,190 feet, J. Research NBS **49,** 227 (1952) RP2357.

[25] Donald H. Menzel, Our sun (Blakiston Co., Philadelphia, Pa., 1949).

[26] Ralph Stair, Spectral-transmissive properties and use of eye-protective glasses, NBS Circular 471 (1948).

[27] Henry Norris Russell, On the albedo of the planets and their satellites, Astrophys. J. **43,** 173 (1916).

[28] G. Rougier, Photometric comparison of moon and sun, Photoelectric albedo of the moon, Compt. rend. **202,** 463 (1936).

[29] Edison Pettit, The co-albedo of the moon, Contr. Mt. Wilson Obs. No. 705, **28,** 173 (1945).

[30] Handbuch der Astrophysik **2,** part 1, Verlag von Julius Springer, Berlin, 1929).

[31] Edison Pettit, Spectral energy-curve of the sun in the ultraviolet, Astrophys. J. **91,** 159 (1940).

WASHINGTON, May 15, 1953.

Phase Equilibria in the System MgO-TiO_2

L. W. Coughanour and V. A. DeProsse

The phase relations in the system MgO-TiO_2 were studied by means of solid-phase reactions between the components and by observing the fusion characteristics of specimens within the system. The existence of three binary compounds in the system was confirmed. From the data obtained, an equilibrium diagram for the system is suggested.

1. Introduction

A study of phase-equilibrium relationships in the system MgO-ZrO_2-TiO_2 has been initiated in connection with a fundamental study of ceramic dielectrics.[1] A survey of the literature pertinent to the problem revealed several discrepancies in the published data on the subordinate binary systems. It was, therefore, considered essential that a preliminary study of the binary systems be made.

An equilibrium diagram for the MgO-TiO_2 system was first published in 1932 by von Wartenberg and Prophet [1].[2] Two compounds, $2MgO$-TiO_2 and MgO-$2TiO_2$, were postulated. The subsequent work of other investigators [2] showed, however, that there are three binary compounds in the system. They are the two listed by von Wartenberg plus MgO-TiO_2. This compound occurs in nature as the mineral geikielite.

The existence of three compounds in the system was confirmed in the present work by means of solid-phase reactions between the components MgO and TiO_2. These reactions took place at various temperatures between 1,200° and 1,550° C. The completeness of reaction and compound formation was observed petrographically and by means of X-ray diffraction patterns of the fired samples.

The determination of the fusion point of each of the three compounds and of the solidus and liquidus temperatures at various points across the system supplied data from which a revised equilibrium diagram was constructed.

2. Sample Preparation and Test Methods

The following materials were used as components in the preparation of samples for this study.

MgO—Water-clear crystals of Norton Co. artificial periclase of nominal purity over 99 percent were selected. The crystals were ground with a mullite mortar and pestle to pass a 325 mesh screen. A spectrogram of the ground material showed only weak lines for the principal impurities, Al, Si, and Ti.

TiO_2—Highly purified titania of nominal purity over 99.9 percent was used. This material was secured from the Titanium Division of the National Lead Co. A spectrogram indicated that the principal impurities, Si, Cu, and Al, were present in amounts less than 0.01 percent.

Calculations of weight composition were made to ± 0.01 percent, no correction being made for the percentage of purity of the components.

The components in sufficient amounts to make a 10 g sample were weighed to the nearest milligram and mixed in the dry condition by shaking in a large container. They were then mixed with approximately 5 percent by weight of a 5-percent soluble-starch solution binder, and 1-in. diameter disks were formed in a hardened steel mold at a pressure of 5,000 lb/in.^{2}. The pressed disks were calcined for 4 to 16 hr at 1,200° C. During heating the disks rested on platinum foil. Oxidizing conditions were maintained by the use of platinum-wound or Globar resistor air-atmosphere furnaces. After cooling, the disks were pulverized using a mullite mortar and pestle, the powdered material was remixed with starch solution binder, and repressed at 5,000 lb/in.^{2}. The repressed disks were then refired for 4 to 5 hr at 1,350° C, again under oxidizing conditions. Petrographic examination, supplemented by X-ray analysis, showed that solid-phase reactions between the components were essentially complete after these two heat treatments.

Following the second calcination the disks were reground, remixed with binder, and disks about ¼ in. high were formed at 15,000 lb/in.^{2} in a ½-in.-diameter mold. From these disks the actual fusion test specimens were ground in the form of small four-sided pyramids, grooved on each side [3]. The fusion tests and softening-range tests were carried out in a thoria-resistor furnace [4]. The specimens were placed in the furnace on a disk of a platinum-rhodium alloy. The metal disk was, in turn, on a support of ThO_2 or BeO. The heating rate during the tests was about 3 deg C/min until the solidus temperature was approached, when it was reduced to about 2 deg C/min. Oxidizing conditions were maintained by slight convection currents of air through the furnace. The temperature and the fusion characteristics of the specimens were observed with an optical pyrometer calibrated at the National Bureau of Standards. The melting point of pure platinum wire was observed as a spot check on the pyrometer calibration. Agreement within 2 deg C of the accepted value of 1,769° C on the 1948 International Temperature Scale was obtained.

In the determination of the solidus and liquidus temperatures of the test specimens, the first sign of liquid formation, rounding of the corners of the test pyramid, was recorded as the solidus temperature. The temperature of complete fusion, as observed through the optical pyrometer, was considered to be the liquidus temperature.

[1] This fundamental study is sponsored by the Department of the Army, Office of Ordnance Research.

[2] Figures in brackets indicate literature references at the end of this paper.

In such determinations, there are several possible sources of error. These include the slight deviation from black-body conditions, the introduction of minute quantities of impurities in the forming and grinding of the specimens, the slight reduction of the TiO_2 on heating, and the inherent difficulty in the visual observation of fusion characteristics.

In the oxide-resistor furnaces used for the fusion tests, black-body conditions were rather closely approached. In order to render the grooved pyramid specimen visible in outline, it was necessary to have a slightly concave surface on the metal disk on which the sample rested during heating. This concave metal surface reflected less light to the pyrometer than the sample did, giving the disk the appearance of being slightly cooler than the specimen.

Partial reduction of the titanates was observed in compositions richer in TiO_2 than $MgO \cdot TiO_2$ when the specimens were quenched or cooled rapidly. It is probable, therefore, that at high temperatures and during the fusion tests there was some loss of oxygen from the samples. This loss might be thought of as introducing a minute quantity of a third component, or impurity, into the samples. It is believed that the error introduced into the fusion-point measurements by this reduction is not significant. Neither by petrographic nor X-ray methods was it possible to detect any evidence of the formation of a lower oxide of titania, even in specimens that had been quenched and were a dark-gray color. This would tend to indicate that the amount of reduction is small. Agamawi and White [5] conducted a weight-loss test on rutile at various temperatures up to 1,550° C. They reached the conclusion that the oxygen loss, on heating rutile in air, is practically negligible. Likewise, Moore [6] showed that, for single crystals of rutile, less than 0.1-percent reduction caused a marked color change.

Probably the largest source of error in the fusion-point measurements was in the problem of selecting the solidus and liquidus points by visual observation. The accuracy would depend upon the viscosity of the melts, the composition, and its relation to a eutectic point or compound, and the experience and judgment of the observer. In this particular system, the fusion of compositions richer than $2MgO \cdot TiO_2$ in MgO was difficult to observe due to the high viscosity of the melts.

Considering these various factors, it is believed that the recorded temperatures are correct to ± 10 deg C.

After the fused specimens had cooled in the furnace, they were analyzed with the petrographic microscope. Such examination was facilitated by the wide difference in the optical properties of the various compounds in the system, and by the fact that large well-formed crystals were obtained. The optical properties of the compounds may be tabulated as follows:

Compound	Optical character	Approximate indices of refraction
MgO	Isotropic	$\eta = 1.736$
$2MgO \cdot TiO_2$	do	$\eta = 1.959$
$MgO \cdot TiO_2$	Uniaxial negative.	$\epsilon = 1.95$, $\omega = 2.28$
$MgO \cdot 2TiO_2$	Biaxial negative.	$\alpha = 2.11$, $\beta = 2.19$, $\gamma = 2.23$
TiO_2	Uniaxial positive.	$\epsilon = 2.903$, $\omega = 2.616$

TABLE 1. *Fusion characteristics of compositions in the system* MgO-TiO_2

Compositions				Effect of heating		Results of petrographic examination (Specimens examined were not quenched and the phases observed may not be those in equilibrium at the liquidus).
Mole		Weight		Fusion started	Fusion completed	
MgO	TiO_2	MgO	TiO_2			
%	%	%	%	°C	°C	
90	10	81.95	18.05	----	----	$MgO + 2MgO \cdot TiO_2$.
80	20	66.87	33.13	1,708	1,741	Do.
77	23	63.63	36.37	1,705	1,727	Do.
75	25	60.22	39.78	1,708	1,726	Do.
73	27	57.24	42.76	1,707	1,728	Do.
70	30	54.23	45.77	1,709	1,727	Do.
66.7	33.3	50.24	49.78	1,732	1,732	$2MgO \cdot TiO_2 + MgO \cdot TiO_2$(trace).
63	37	46.37	53.63	1,580	1,726	$2MgO \cdot TiO_2 + MgO \cdot TiO_2$.
60	40	43.08	56.91	1,587	1,685	Do.
57	43	40.23	59.77	1,581	1,600	Do.
53	47	36.41	63.59	1,583	1,615	Do.
50	50	33.55	66.45	1,629	1,631	$MgO \cdot TiO_2 + MgO \cdot 2TiO_2$(trace).
47	53	31.04	68.96	1,589	1,611	$MgO \cdot TiO_2 + MgO \cdot 2TiO_2$.
43	57	27.69	72.31	1,591	1,598	Do.
40	60	25.17	74.83	1,592	1,619	Do.
37	63	22.97	77.03	1,594	1,635	Do.
33.3	66.7	20.15	79.86	1,652	1,652	$MgO \cdot 2TiO_2$.
30	70	17.87	82.13	1,608	1,642	$MgO \cdot 2TiO_2 + TiO_2$.
27	73	16.33	83.67	1,605	1,639	Do.
25	75	14.39	85.61	1,608	1,628	Do.
23	77	12.85	87.15	1,607	1,638	Do.
20	80	11.20	88.80	1,608	1,622	Do.
18	82	9.72	90.28	1,607	1,615	Do.
15	85	8.22	91.78	1,605	1,612	Do.
12	87	6.44	93.56	1,609	1,635	$MgO \cdot 2TiO_2 + TiO_2$.

For the biaxial compound $MgO{\cdot}2TiO_2$, $2V$ was estimated, from interference figures, to be 70° to 75°. Calculation of $2V$ from the indices of refraction gave a value of 68°.

The results of the fusion tests and of the petrographic analysis of the nonquenched specimens are listed in table 1.

3. Results and Comparisons With Previous Work

The equilibrium diagram for the system as determined by von Wartenberg is shown in figure 1. That constructed from the results of the present study is shown in figure 2. Comparison of the two diagrams shows that, apart from the introduction of the third compound, the major difference between the two is the lower fusion points obtained in the present study. It is believed that these temperature differences are explained simply by the greater refinement of the methods used in the study covered by this report.

Other fusion-point data published on the system are extremely limited in extent. The fusion point of the compound $MgO{\cdot}2TiO_2$ was determined by Sigurdson and Cole [2,e] to be 1,645° C under oxidizing conditions. This is in excellent agreement with the presently determined value of 1,652° C. St. Pierre [7] determined the fusion point of highly purified TiO_2 to be 1,840° ±10° C, again under oxidizing conditions. This value, also, is in excellent agreement with the value 1,839° C observed in the present study.

Büssem, et al. [2,a] conducted an X-ray investigation of the system. They did not determine an equilibrium diagram, but they did obtain results that indicated, to them, the existence of a high-temperature solid solution of MgO in $2MgO{\cdot}TiO_2$. They selected compositions in the area between MgO and $2MgO{\cdot}TiO_2$ and heated them to approximately 1,460° C. They then compared the X-ray powder patterns of the cooled samples with the patterns of mechanical mixtures of the same over-all compositions, the mechanical mixtures being prepared from the components MgO and $2MgO{\cdot}TiO_2$. They noted that the diffraction lines of MgO were sharper and clearer for the mixtures than for the heated compositions. This effect they attributed to a high-temperature solid solution of MgO in $2MgO{\cdot}TiO_2$ with an unmixing or exsolution reaction on cooling. The unmixing was thought to result in extreme subdivision of the MgO grains with the subsequent lack of sharpness in the MgO diffraction lines.

A similar test was made during the present study on the composition $4MgO{:}TiO_2$. The results obtained were negative, there being no significant differences in the diffraction patterns of the heated sample and of the mechanical mixture.

Several attempts were made in the present study to detect solid-solution formation in the system. Particular attention was given to the high MgO portion of the system, in order to verify or disprove the existence of the high-temperature solid solution of MgO in $2MgO{\cdot}TiO_2$ postulated by Büssem. In one method, samples high in MgO content ($9MgO{:}TiO_2$, $4MgO{:}TiO_2$, $3MgO{:}TiO_2$) which had been previously calcined were used. Portions of the calcines were heated for 2 hr at 1,400° C and for ½ hr at 1,650° C and were cooled slowly. The cooled samples were examined petrographically and by means of X-rays. The petrographic examination showed that the index of refraction of MgO, and of $2MgO{\cdot}TiO_2$, had not deviated from its normal value in either case. In addition, the MgO grains did not have the appearance of having undergone an unmixing reaction. X-ray diffraction patterns showed no significant intensity variations or parameter changes.

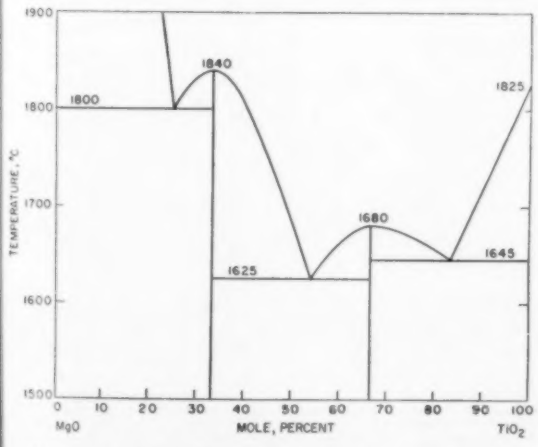

FIGURE 1. $MgO{-}TiO_2$ *system; after von Wartenberg, reference* [1].

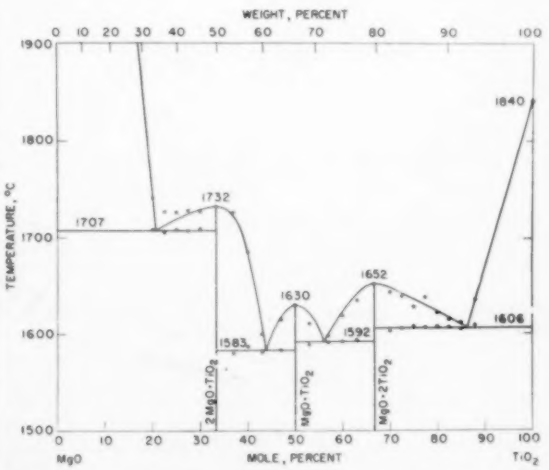

FIGURE 2. *Proposed diagram for the* $MgOTi{-}O_2$ *system.*

In another attempt to verify any solid-solution formation, specimens of the same compositions were heated to 1,460° or 1,500° C and the temperature was maintained constant for 3 hr. The specimens were then quenched in water. Again, petrographic examination of the quenched specimens showed no change in the index of refraction of either MgO or $2MgO \cdot TiO_2$. The results of these tests indicate that there is no solid-solution formation between $2MgO \cdot TiO_2$ and MgO. Index of refraction measurements of these two compounds were accurate to about 2 units in the third decimal (± 0.002). With this degree of accuracy, solid solution formation to the extent of 1 percent could have been detected.

Similar tests at various points on the diagram failed to indicate any solid solutions in the system. Finally, the fact that the solidus lines obtained are horizontal is indicative of the absence of solid-solution formation.

4. Summary and Conclusions

Twenty-six compositions in the system $MgO \cdot TiO_2$ were prepared. They were studied from the standpoints of solid-phase reactions and fusion behavior. The existence of three binary compounds in the system was confirmed. They are $2MgO \cdot TiO_2$, $MgO \cdot TiO_2$, and $MgO \cdot 2TiO_2$. Their melting points were determined to be 1,732°, 1,630°, and 1,652° C, respectively. Four eutectic points were located as follows: 21-mole percent of TiO_2, and 1,707° C; 44-mole percent of TiO_2, and 1,583° C; 56-mole percent of TiO_2 and 1,592° C; and 86-mole percent of TiO_2 and 1,606° C. No evidence of solid-solution formation was obtained. From these data an equilibrium diagram for the system is suggested.

This work was sponsored by the Office of Ordnance Research, Department of the Army.

All X-ray analyses for the project were performed by R. S. Roth.

5. References

[1] H. von Wartenberg and E. Prophet, Z. anorg. Chem. **208,** 373 (1932).

[2] (a) W. Büssem, C. Schusterius, and A. Ungewiss, Ber. deut. keram. Ges. **18,** 433 (1937);
(b) W. Jander and K. Bunde, Z. anorg. Chem. **239,** 418 (1938);
(c) Y. Tanaka, Bul. Chem. Soc. Japan **60,** 212 (1939);
(d) H. A. McKinstry, C. F. Hocker, W. R. Ricker, W. H. Earhart, N. R. Thielke, and E. C. Henry, Quarterly Progress Report on the Investigation of Refractory Materials, School of Mineral Industries, Pennsylvania State College (May 15, 1949);
(e) H. Sigurdson and S. S. Cole, J. Metals **1,** No. 12, Trans. 905 (1949).

[3] R. F. Geller, P. J. Yavorsky, B. L. Steierman, and A. S. Creamer, J. Research NBS **36,** 277 (1946) RP1703.

[4] (a) R. F. Geller, J. Research NBS **27,** 555 (1941) RP1443.
(b) S. M. Lang and R. F. Geller, J. Am. Ceram. Soc. **34,** 193 (1951).

[5] Y. M. Agamawi and J. White, Trans. Brit. Ceram. Soc. **51,** 293 (1951).

[6] C. H. Moore, Jr., Trans. Am. Inst. Mining Met. Eng. **184,** 194 (1949); Mining Eng. **1,** 194 (1949); Tech. Pub. No. 2617.

[7] P. O. S. St. Pierre, J. Am. Ceram. Soc. **35,** 188 (1952).

WASHINGTON, May 7, 1953.

Journal of Research of the National Bureau of Standards Vol. 51, No. 2, August 1953 Research Paper 2436

Pairs of Normal Matrices With Property L

Helmut Wielandt [1]

A short proof is given, under weaker assumptions, of the following theorem first proved by N. Wiegmann: If the eigenvalues α_i, β_i of two normal $n\times n$ matrices A, B may be numbered in such a way that the eigenvalues $\gamma_i(z)$ of $C(z)=a+zb$ are given by $\gamma_i(z)=\gamma_i+z\beta_i$ (for $i=1, \ldots, n$ and all complex values of z), then $AB=BA$.

Two $n\times n$ matrices A, B are said [2] to have property L if their eigenvalues α_k, $\beta_k (k=1, \ldots, n)$ may be ordered in such a way that the eigenvalues of $\alpha A+\beta B$ are given by $\alpha\alpha_k+\beta\beta_k$ for all complex numbers α, β. Though every pair of commuting matrices has property L, the converse is not true.[2] However, if A and B have property L and are normal, then $AB=BA$ according to a theorem of Wiegmann.[3] We wish to show that the assumptions of Wiegmann's theorem may be weakened considerably. We begin by proving the following lemma which has some interest in itself.

LEMMA: *Let A and B be arbitrary $n\times n$ matrices. Then the set Z of all points z in the complex plane for which $A+zB$ is normal, is either the whole plane, a straight line, a circle, or it contains, at most, two points. If B is normal, neither the circle case nor the two-point case may enter. If Z is the entire plane then $AB=BA$.*

PROOF: $A+zB$ is normal if, and only if,

$$(A+zB)(A^*+\bar{z}B^*)-(A^*+\bar{z}B^*)(A+zB)=0. \quad (1)$$

If $z=x+iy$, (1) is equivalent to a set of $2n^2$ real linear equations in x,y, and (x^2+y^2). Each of these $2n^2$ equations defines either the whole plane, a circle, a straight line, or else, at most, one point. The intersection of these $2n^2$ point sets obviously is one of the six types described in the lemma. That all these types may indeed occur is shown by the following matrices $A+zB$:

$$(1+z),\quad \begin{pmatrix}1 & z\\ z & 0\end{pmatrix},\quad \begin{pmatrix}0 & z\\ 1 & 0\end{pmatrix},$$

$$\begin{bmatrix}0 & z & 0\\ 0 & 0 & z\\ z & 0 & z-1\end{bmatrix},\quad \begin{pmatrix}0 & z\\ 0 & 0\end{pmatrix},\quad \begin{pmatrix}0 & 1\\ 0 & 0\end{pmatrix}.$$

In case B is normal, the terms of (1) containing $z\bar{z}$ cancel, hence Z is determined by linear equations in x and y only. So Z is neither a circle nor a pair of points.

In case Z is the entire plane (1) holds for every z, hence the coefficient of z vanishes, that is, $BA^*-A^*B=0$. Since B commutes with A^*, it also commutes with every polynomial $f(A^*)$, hence, with A itself. (If A is normal, then $A=f(A^*)$ for some polynomial f. This well-known fact follows by transforming A into diagonal form by means of a unitary transformation.) The lemma being proved, we turn to the generalization of Wiegmann's theorem.

THEOREM: *If the eigenvalues α_k, β_k of two normal matrices $A=(a_{ik})$, $B=(b_{ik})$ may be ordered in such a way that the eigenvalues $\gamma_k(z)$ of $A+zB$ satisfy the inequalities*

$$\sum_{k=1}^{n}|\gamma_k(z)|^2\geqq\sum_{k=1}^{n}|\alpha_k+z\beta_k|^2 \quad (2)$$

for some values $z=z_\lambda$ $(\lambda=1, \ldots, l)$ which are the vertices of a polygon containing 0 in its interior, then $AB=BA$. (This obviously contains Wiegmann's theorem since if A and B have property L then (2) holds even with equality sign for every z.)

PROOF: According to a theorem of Schur,[4] we have

$$\sum_{i,k}|a_{ik}+zb_{ik}|^2\geqq\sum_{k}|\gamma_k(z)|^2 \quad (3)$$

for every z, where the equality holds if, and only if, $A+zB$ is normal. From (3) and (2) we have for $z=z_\lambda$

$$\sum_{i,k}|a_{ik}+zb_{ik}|^2\geqq\sum_{k}|\alpha_k+z\beta_k|^2 \quad (4)$$

which reduces to

$$\sum_{i,k}(a_{ik}\bar{z}\bar{b}_{ik}+\bar{a}_{ik}zb_{ik})-\sum_{k}(\alpha_k\bar{z}\bar{\beta}_k+\bar{\alpha}_kz\beta_k)\geqq 0 \quad (5)$$

since $\sum|a_{ik}|^2=\sum|\alpha_k|^2$ and $\sum|b_{ik}|^2=\sum|\beta_k|^2$ in view of the fact that A and B are normal. Since the left-hand side of (5) is linear and homogeneous in x and y, (5) defines either a half plane containing 0 on its boundary or the left-hand side of (5) vanishes identically. The former case cannot occur, for the half plane contains $z_1, \ldots, z_l$, hence it contains 0 in its interior. So in (5), and hence in (4), equality holds for every z. Combining this with (2) and (3) we

[1] American University and University of Tübingen. This paper was prepared under a National Bureau of Standards contract with The American University.

[2] T. S. Motzkin and O. Taussky, Pairs of matrices with property L, Trans. Am. Math. Soc. **73**, 108–114 (1952).

[3] N. Wiegmann, Pairs of normal matrices with property L, Proc. Am. Math. Soc. 4, 35–36 (1953).

[4] I. Schur, Über die charakterischen Wurzeln einer linearen Substitution mit einer Anwendung auf die Theorie der Integralgleichungen, Math. Ann. **66**, 488–510 (1909); Theorem II. The theorem of Schur has recently been used in a related problem by H. Schneider, Theorems on normal matrices, Quart. J. Math. Oxford [2] **3**, 241–249 (1952).

conclude that in (3) equality holds for $z=z_k$, hence $A+z_kB$ is normal. Since $z_1,\ldots,z_l$ are not collinear and B is normal, the lemma asserts that $A+zB$ is normal for every z, hence $AB=BA$.

REMARK: The theorem is best possible in the sense that there exist noncommuting normal matrices A, B such that inequality (2) holds for every z of a closed half plane containing 0 on its boundary (and for a fixed suitable ordering of the eigenvalues α_k,β_k). An example is given by

$$A=\begin{pmatrix} 1 & 0 & 0 & 0 \\ 0 & -1 & 0 & 0 \\ 0 & 0 & i & 0 \\ 0 & 0 & 0 & -i \end{pmatrix}, \qquad B=\begin{pmatrix} 0 & 0 & 0 & 0 \\ 0 & 0 & 0 & 0 \\ 0 & 0 & 0 & 1 \\ 0 & 0 & -1 & 0 \end{pmatrix}$$

with the ordering $\alpha_k=1,\ -1,\ i,\ -i;\ \beta_k=i,\ -i,\ 0,\ 0$. Here we have $\gamma_k(z)=1,\ -1,\ (-1-z^2)^{\frac{1}{2}},\ -(-1-z^2)^{\frac{1}{2}}$, hence $\sum|\gamma_k(z)|^2\geqq\sum|\alpha_k+z\beta_k|^2$ for every z with $\Im z\geqq 0$ (though $\gamma_k(z)=\alpha_k+z\beta_k$, $k=1,\ldots,4$ is valid for $\Im z=0$ only).

WASHINGTON, April 17, 1953.

Heat Capacity of Gaseous Hexafluoroethane[1]

John S. Wicklund, Howard W. Flieger, Jr., and Joseph F. Masi

An accurate flow calorimeter has been used to measure the heat capacity (C_p) of gaseous hexafluoroethane (C_2F_6) at $-50°$, $-20°$, $+10°$, $+50°$, and $+90°$ C and at 0.5-, 1.0-, and 1.5-atmosphere pressure. The results are believed to be accurate to ± 0.1 percent.

The values of C_p have been extrapolated to zero pressure at each temperature; the ideal-gas heat capacities thus obtained at the five temperatures are, respectively, 20.99, 22.79, 24.43, 26.45, and 28.24 calories mole^{-1} degree^{-1}. Calculated results, using recent frequency assignments and molecular data, were 0.4 to 0.7 percent higher than the experimental results.

The values of the pressure coefficient of heat capacity at the five temperatures have been used in conjunction with literature data to obtain an equation of state for hexafluoroethane at low pressures.

1. Introduction

Accurate measurements of gas heat capacity over a range of low pressures and at several temperatures provide important information about both the ideal gas and the low-pressure equation of state. The flow calorimeter used in this investigation has been previously described.[2, 3] This measures the heat capacity of gases with an accuracy of the order of 0.1 percent, from $-50°$ to $+100°$ C, and up to about 1.5 atm.

The heat capacity of gaseous hexafluoroethane is of particular interest because of the question of the size of the potential barrier to internal rotation. Pace and Aston [4] made calorimetric measurements on the solid and liquid, and obtained third-law entropies of the ideal gas; comparison with certain spectroscopic calculations led them to a value of 4,350 calories mole^{-1} for the potential barrier.

2. Experimental Procedure

2.1. Material

A specially purified sample of C_2F_6 was obtained from Minnesota Mining & Manufacturing Corp. It was further purified by evaporation at the temperature of a slush of dry ice in a 50–50 mixture of $CHCl_3$ and CCl_4, and subsequent condensation in a trap surrounded by liquid nitrogen, while pumping with a high-vacuum apparatus. Approximately 385 g of final sample were obtained in this manner.

A mass-spectrographic analysis of the sample as used indicated a purity of 99.4 mole percent or better, with a maximum of 0.1 mole percent CO_2, 0.5 percent N_2, and/or CO, and a trace of a hydrocarbon. A separate test with a phosphoric acid conductimetric method indicated only 0.02 mg of water per liter of sample.

2.2. Apparatus and Method

The construction of the flow calorimeter and its operation have been described in detail elsewhere (footnote 2); a brief résumé has also been published (footnote 3).

A new electronic control system, designed and built at the National Bureau of Standards, was used successfully to control the temperature of the radiation shield to within ± 0.01 deg C of the average temperature of the tube containing the heated gas. This control is to be described in a future publication.

The heat capacity was determined at a number of different flow rates at each temperature and pressure, so that any residual heat leak could be eliminated by extrapolation to the zero of reciprocal rate. "Blank" determinations were made at several rates at each temperature and pressure to measure the amount of cooling, δT, experienced by the gas in passing through the calorimeter when no heat was applied. A total of 67 heat-capacity experiments and 75 blank experiments were made.

3. Results

3.1. Heat Capacity of Hexafluoroethane

If W is the power supplied to the heater, F is the rate of flow of gas, ΔT is the observed rise in temperature, and δT is the fall in temperature in a corresponding blank experiment, the apparent heat capacity is calculated by

$$C = \frac{WF^{-1}}{\Delta T + \delta T} \quad (1)$$

The values of C were corrected for the deviation of the observed mean pressure and mean temperature from the nominal values. These corrections were small in all cases. The corrected heat capacity, called C_p (observed), was plotted against the reciprocal of the rate of flow at each temperature and pressure and straight lines were fitted to the points by the method of least squares.

The least-square lines had very small slopes; moreover, the slopes were not constant with pressure at some of the temperatures. An analysis of variance was performed to test the significance of the slopes obtained. As a result, it was decided to abandon, in this case, the usual linear extrapolation to infinite rate, and to obtain the final values of heat capacity by simple averaging of the C_p (observed) at each temperature and pressure. The results of this process are listed in table 1, converted to calories mole^{-1} degree^{-1}. (The calorie is 4.1840 j, the molecular weight is 138.02, and 0° C=273.16° K). Each of the experimental values listed in table 1 is the mean of at least four determinations. Following each tabular value is the standard deviation of the experiments from the mean; the average of these deviations is

[1] This work was supported by the Ordnance Corps, Department of the Army.
[2] J. F. Masi and B. Petkof, J. Research NBS 48, 179 (1952). RP2303.
[3] J. F. Masi, J. Am. Chem. Soc. 74, 4738 (1952).
[4] E. L. Pace and J. G. Aston, J. Am. Chem. Soc. 70, 566 (1948).

TABLE 1. *Heat capacity of gaseous hexafluoroethane*

Summary of results

Temperature, °C	−50.00	−20.00	10.00	50.00	90.00
	C_p, calories mole^{-1} degree^{-1}				
Pressure:					
1.50 atm	21.803, ±0.005	23.234, ±0.003	24.718, ±0.011	26.615, ±0.009	28.367, ±0.011
1.00 atm	21.539, ±0.009	23.072, ±0.007	24.617, ±0.009	26.547, ±0.016	28.333, ±0.008
0.50 atm	21.257, ±0.010	22.938, ±0.009	24.526, ±0.010	26.506, ±0.006	28.283, ±0.019
C_p^0, observed	20.99	22.79	24.43	26.45	28.24
C_p^0, spectroscopic	21.13	22.90	24.56	26.56	28.36
$\Delta C_p/\Delta P$, cal mole^{-1} deg^{-1} atm^{-1}	0.546	0.296	0.192	0.109	0.084

±0.037 percent compared with ±0.036 percent for the corresponding precision index in the case of least-square lines fitted to the experiments.

The final values of heat capacity at finite pressures in table 1 were extrapolated linearly to zero pressure at each temperature, and the results are given as "C_p^0, observed." It is believed that these heat-capacity values for the ideal gas C_2F_6 are reliable to better than ±0.15 percent.

An assignment of the fundamental frequencies of C_2F_6 was made by Nielsen, Richards, and McMurry.[5] Pace and Aston (footnote 4) have used this assignment in conjunction with their experimental third-law entropies at 176.61° and 194.87° K to obtain a value of 4,350 calories mole^{-1} for the barrier to internal rotation. A recent note by Mann and Plyler [6] puts the lowest frequency (ν_9) at 220 cm^{-1} by direct observation in the infrared, and suggests new estimates for the interatomic distances. The barrier energy becomes 3,920 cal on the basis of these changes. The heat capacity has been calculated from this slightly revised assignment, for the harmonic-oscillator, rigid-rotator approximation, and the results at the temperatures of the present experiments are given in table 1 as "C_p^0, spectroscopic." They are seen to be 0.4 to 0.7 percent higher than the observed values.

3.2. Equation of State of Hexafluoroethane

It is assumed here that in the low-pressure region covered by these experiments the equation of state of C_2F_6 is of the form

$$PV=RT+BP, \tag{2}$$

where B is a function of the temperature. The thermodynamic relation

$$\left(\frac{\partial C_p}{\partial P}\right)_T=-T\left(\frac{\partial^2 B}{\partial T^2}\right)_P \tag{3}$$

must be satisfied by the second derivative of the second virial coefficient B. The values of $\Delta C_p/\Delta P$ listed in the last line of table 1 were taken to be the left-hand member of eq (3), and B was assigned the form proposed by Hirschfelder, McClure, and Weeks:[7]

$$B=b-ce^{a/T}. \tag{4}$$

The values of c and a were then chosen to fit the data of this experiment, whereas b was obtained from the vapor-density data of Pace and Aston (see footnote 4) at 25° C. The final expression for the virial coefficient in eq (2) was

$$B=91-58.2e^{495/T}\ \text{cm}^3\ \text{mole}^{-1}. \tag{5}$$

The experimental values of $\Delta C_p/\Delta P$ are plotted as as circles in figure 1. The calculated values obtained by differentiating eq (5) are indicated by the solid curve, whereas the dashed curve is calculated from the Berthelot equation, using the critical constants given by Pace and Aston (see footnote 4). Table 2 shows that eq (5) reproduces the results of Pace and Aston's calculation of B from vapor pressure and heat of vaporization measurements, at least as well as the Berthelot equation.

TABLE 2. *Comparison between equations of state of gaseous hexafluoroethane*

Temperature, T	Value of B		
	Data of Pace and Aston (see footnote 4)	Berthelot equation	Equation (5)
°K	cm^3 mole^{-1}	cm^3 mole^{-1}	cm^3 mole^{-1}
179.96	−837	−822	−820
180.22	−815	−819	−816
188.30	−758	−738	−715
190.05	−766	−721	−696
194.87	−641	−678	−647
194.90	−653	−678	−647
195.10	−611	−676	−646
195.21	−624	−675	−644
298.16	−215 (avg)	−268	(−215)

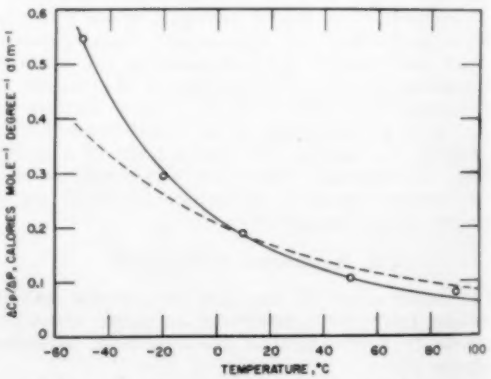

FIGURE 1. *Pressure coefficient of heat capacity of hexafluoroethane.*

○, this research; ————, equation 5; — — — —, Berthelot equation.

WASHINGTON, May 7, 1953.

[5] J. R. Nielsen, C. M. Richards, and H. L. McMurry, J. Chem. Phys. **16**, 67 (1948).
[6] D. E. Mann and E. K. Plyler, J. Chem. Phys. **21**, 1116 (1953).
[7] J. O. Hirschfelder, E. T. McClure, and I. F. Weeks, J. Chem. Phys. **10**, 201 (1942).

Journal of Research of the National Bureau of Standards Vol. 51, No. 2, August 1953 Research Paper 2438

Effective Circuit Bandwidth for Noise with a Power-Law Spectrum

Philip R. Karr

The effective bandwith of tuned circuits for noise with a power-law spectrum is derived and discussed. Comparison is made with the usual case of "flat" noise.

The noise bandwidth of tuned (RLC) circuits for "white," or "flat," noise is well known.[1] However, corresponding results for noise with other types of spectra have apparently not been discussed very much. In connection with some noise-measurement work currently going on at the National Bureau of Standards, the writer worked out the effective noise bandwidth in the case of an f^α spectrum (f being the frequency). The ratio between the effective bandwidth for the noise and the half-power bandwidth is, in some cases, appreciably different from the well-known factor 1.57 that applies to flat noise; in other cases, the correction is quite small. These results are offered for publication in the belief that this knowledge will be of value to others engaged in noise work. Spectra of this form are encountered in transistor noise, resistor current noise, flicker effect noise, etc.

We consider a random noise current whose spectral intensity (often called power spectrum) follows the law f^α, driving a circuit consisting of the parallel [2] elements R, L, C.

The impedance Z of such a stage is

$$Z=\frac{Rd}{d+j\left(\frac{f}{f_0}-\frac{f_0}{f}\right)}, \tag{1}$$

where $f_0=(2\pi LC)^{-1/2}$ is the resonance frequency, and

$$d=\frac{1}{2\pi f_0 RC}=\frac{1}{Q}=\frac{2\pi f_0 L}{R}=\frac{1}{R}\sqrt{\frac{L}{C}}$$

is the dissipation factor or reciprocal of Q. It is easily shown that df_0 is the frequency difference between the half-power points of the circuit; that is, it is the bandwidth b.

The mean-square output voltage of the circuit when driven by the noise is, with an obvious normalization,

$$\langle V^2\rangle=\int_0^\infty f^\alpha|Z|^2\,df \tag{2}$$

$$=bdf_0^\alpha R^2 I, \tag{2a}$$

where

$$I=\int_0^\infty \frac{x^\alpha dx}{d^2+\left(x-\frac{1}{x}\right)^2}. \tag{3}$$

The main task before us then is the evaluation of I. This evaluation is facilitated by the change of variable $y=x^2$, which gives

$$I=\tfrac{1}{2}\int_0^\infty \frac{y^{\frac{1+\alpha}{2}}dy}{y^2+2y\cos\lambda+1},$$

where

$$\cos\lambda\equiv\frac{d^2}{2}-1.$$

This integral may now easily be evaluated by contour integration in the complex plane. Omitting the details, the result is

$$I=\frac{\pi}{2\sin\left(\frac{1+\alpha}{2}\right)\pi}\,\frac{\sin\left(\frac{1+\alpha}{2}\right)\lambda}{\sin\lambda}, \tag{4}$$

if $-3<\alpha<1$ and $-\pi\angle\lambda<\pi$.

The restrictions on α and λ must be carefully adhered to. If values of α outside the specified range are used, the integral will diverge. Thus the device of assuming that the spectral law is constant for all frequencies, which appears to be justified in many cases when the integral will converge, cannot be used when $\alpha\geq 1$ or ≤ -3.

Now we may define the effective bandwidth as

$$B=\frac{\langle V^2\rangle}{R^2 f_0^\alpha} \tag{5}$$

so that

$$B=bdI. \tag{6}$$

For flat noise we insert $\alpha=0$ in (4), obtaining $I=\pi/2d$, so that

$$B_0=\frac{\pi}{2}b, \tag{7}$$

which is the well-known result for flat noise. The subscript refers to the case $\alpha=0$.

[1] See e. g., Valley and Wallman, Vacuum tube amplifiers, p. 109 (McGraw-Hill Book Co., Inc., New York, N. Y., 1948).

[2] The results may be easily applied to the series RLC case.

Using (7), (4), and (6), we may now write

$$\frac{B}{B_0}=\frac{d}{\sin\frac{\pi}{2}(1+\alpha)}\,\frac{\sin\frac{\lambda}{2}(1+\alpha)}{\sin\lambda}. \tag{8}$$

B/B_0 is the correction factor for the effective noise bandwidth resulting from the deviation of α from 0.

The correction factor B/B_0 is an even function of $\alpha+1$, that is for example, it is the same for $\alpha=0$ as it is for $\alpha=-2$. (Therefore, we have the interesting result that the effective bandwidth for $\alpha=-2$ is the same as it is for flat noise.)

A plot of B/B_0 versus α for fixed d would take the form of a U-shaped curve with the bottom of the U occuring at $\alpha=-1$: The curve is symmetrical about $\alpha=-1$. B/B_0 is less than 1 in the range $-2<\alpha<0$, is equal to 1 for $\alpha=-2$ and $\alpha=0$, and is greater than 1 outside this range; it increases toward infinity as α approaches 1 from the left or -3 from the right.

A family of curves for B/B_0 may be plotted without difficulty. However, a quick idea of the magnitude of the correction may be obtained from the following formulas to which (8) reduces in special cases:

$$\left.\begin{aligned}
&\alpha=0,\ 2;\ \frac{B}{B_0}=1\\
&\alpha=\frac{1}{2},-2\frac{1}{2};\ \frac{B}{B_0}=\sqrt{1+\frac{d}{2}}+\frac{d}{2}\,\frac{1}{\sqrt{1+\frac{d}{2}}}\\
&\alpha=-\frac{1}{2},-1\frac{1}{2};\ \frac{B}{B_0}=\frac{1}{\sqrt{1+\frac{d}{2}}}\\
&\alpha=-1;\ \frac{B}{B_0}=\frac{1-\frac{1}{\pi}\sin^{-1}d\sqrt{1-\frac{d^2}{4}}}{\sqrt{1-\frac{d^2}{4}}}
\end{aligned}\right\} \tag{9}$$

For example, for $d=0.1$, $\alpha=-1$, we find immediately $B/B_0\approx 1-d/\pi\approx 0.97$.

Thus for reasonably high values of $Q(=1/d)$, the corrections in the range $-2<\alpha<0$ are rather small. Outside this range the corrections may be large.

Washington, May 19, 1953.

Journal of Research of the National Bureau of Standards Vol. 51, No. 2, August 1953 Research Paper 2439

Penetration of X- and Gamma Rays to Extremely Great Depths[1]

U. Fano[2]

Earlier work on the asymptotic trend of the X-ray intensity at great distances from a source is reviewed and completed in various aspects. The asymptotic law is shown to be the same as in the "straight-ahead" approximation (which disregards deflections) whether the primary energy is higher or lower than the energy of minimum absorption, provided a constant is replaced by the eigenvalue of a suitable Wick equation. The penetration in directions oblique to the source direction hardly ever attains its asymptotic trend when the source energy is lower than the energy of minimum absorption. This situation raises a difficult problem regarding the penetration law in the range of great depths where the asymptotic trend is being approached very slowly.

1. Introduction

The deep penetration of X-rays, or gamma rays, in an infinite, homogeneous medium are discussed. Much fundamental understanding of this phenomenon derives from the work of Wick [1][3] on the analogous phenomenon of neutron penetration. Vice versa, the present work might contribute additional clarification to neutron problems as well as some background for still unsolved problems of charged-particle penetration.

This paper constitutes a final report of developments since 1948. It includes a review of preliminary reports [2, 3, 4] and new material that was required to complete the initial program. Some concepts and techniques developed in the course of the study but not utilized in the eventual solution are nevertheless reported briefly.

The assumption of an infinite, homogeneous medium disregards the effect of boundaries and inhomogeneities, which constitutes a separate, still largely unsolved, problem.

The very deep penetration of X-rays depends primarily on the course of multiple Compton scattering under conditions where photoelectric absorption and pair production are comparatively unimportant. At the low-energy end of the spectrum, for example, below 50 kev, where the energy shift of the scattered photons can be disregarded or treated as a small correction, the diffusion of photons has been studied by Chandrasekhar [5], but without specific reference to very deep penetrations. (Notice that photons below 50 kev disappear rapidly by photoelectric effect, in most materials.)[4] At the high-energy end, where large amounts of X-rays are regenerated by electrons, a complete study of X-ray penetration would require a treatment of the whole cascade shower process. The X-ray regeneration remains moderate for secondary electrons up to 10 Mev in lead, and up to 100 Mev in light materials, and may be treated, if necessary, in this energy range as a secondary source. The present paper disregards the regeneration of X-rays by electrons and treats pair production as a mechanism of outright absorption. Nevertheless, its results apply to the penetration of the tail end of showers that is controlled by photons below 10 Mev in lead and below 100 Mev in light elements.

We shall deal primarily with photons from 50 kev to 50 Mev which experience concurrent processes of energy degradation and multiple scattering terminating in outright absorption. Repeated Compton scattering of the "primary" radiation emitted by a source gives rise to "secondary" X-rays of lower energy traveling in all directions. In a medium of low atomic weight, a photon may be scattered 5 or 10 times, on the average, before eventual absorption by photoelectric effect. The main complication in our study arises from the generation of this complex radiation.

[1] Work supported by the Office of Naval Research and by the Atomic Energy Commission Reactor Division.

[2] Appendix C is by L. V. Spencer.

[3] Figures in brackets indicate the literature references at the end of this paper.

[4] This consideration applies also to the further development of Chandrasekhar's method that was carried out by O'Rourke [21] in connection with the X-ray penetration problem.

This complication and the complicated dependence of the cross sections on the photon energy preclude a fully analytical treatment of the problem. Therefore, the analytical treatment that is developed in this paper does not lend itself readily to direct numerical applications. However, its results provide one of the footings for a practical method of numerical calculation [6] whose range of application extends to very large distances from the source. The analytical laws of intensity variation versus depth also serve to extrapolate the results of numerical calculations to still greater distances from the source.

Throughout the present investigation, much reliance has been placed on gaining an initial qualitative understanding of the factors that control the process of degradation, scattering, and penetration of X-rays. Such an understanding enables one to adapt the mathematical procedure to the conditions affecting each specific problem. In this respect our work departs from other work in the same field that has been characterized by the initial adoption of less flexible procedures. For example, the X-ray distribution has been resolved into "orders of scattering" (that is, into once-, twice-, thrice-, . . ., scattered photons) [7, 8, 9]. The expansion converges poorly where the photons experience protracted scattering and its application becomes cumbersome. However, at least in some instances, adequate calculations of penetration have been made [8]. Semiempirical improvements to the procedure have also been introduced [9]. Alternatively one may schematize the scattering and degradation process in such a way that the corresponding basic equations are sufficiently simplified to allow analytic solution [7, 9, 10, 11]. These simplifications, however, seem generally to involve considerable limitations in the applications of the theory and may delete some characteristic features of the phenomenon. Finally, calculations by the "Montecarlo" sampling methods are possible [12] but do not yet appear convincingly successful, at least in their application to very deep penetrations, which requires the use of "biased sampling".

Our treatment will be limited to X-ray distributions having a plane symmetry, that is, which vary in one direction of space only and are generated by sources having the same symmetry. The study of spherically symmetrical distributions is essentially equivalent to that of plane-symmetrical ones. The relationship between these types of distributions is well known [1] and will be indicated in Appendix A. We shall also assume that the source is concentrated on a single plane, which implies no additional restriction owing to the linearity of the problem. Notice that plane symmetry may always be attained by considering, instead of the X-ray flux at each point and in each direction, only the integral or the average flux over all points of a plane and over all directions forming the same angle with the plane. The reason is that this plane integral flux generated by a localized source is equal to the localized flux generated by a plane distribution of sources.

The most general type of source may be regarded as an aggregate of point monodirectional sources. The study of X-ray penetration under conditions of plane symmetry may serve as a first step for the treatment of point monodirectional sources. This approach has been exploited in the study of X-ray penetration to small or moderate distances from a source [13].

2. Survey of the Problem

This section contains a qualitative analysis of the deep penetration of X-rays, with the purpose of pointing out the specific problems that require a detailed mathematical treatment.

2.1. Transient Processes and Equilibrium States

The layers of material near an X-ray source are traversed almost exclusively by primary radiation because it takes a certain thickness of material to generate a substantial amount of secondary radiation. Therefore, one expects the intensity of secondary radiation to build up rapidly from one layer to the next near the source in a sort of transient process. Vice versa, at greater depth within a material one may hope to find some sort of steady state in which the secondary radiation is present in substantial amounts. The nature of this steady state is the main object of this investigation.

A typical steady state in which a softer radiation continually arises from a harder one is commonly called a state of radiative "equilibrium." The X-ray penetration problem does not lead to a typical state of equilibrium, but it is helpful to review first the properties of such a state. Equilibrium involves, in general, three different features, namely: (1) The ratio of the intensity of the secondary to the intensity of the primary radiation approaches asymptotically a maximum value, as the depth of penetration increases. (2) The quality of the secondary radiation also becomes independent of the depth of penetration, because the intensities of its various spectral components bear a constant asymptotic ratio to the primary intensity. (3) Therefore, the intensity of the whole radiation is controlled by the progressive attenuation of the primary radiation, which follows an exponential law in the case of X-rays. If these circumstances applied, they would greatly simplify the study of penetration. The maximum values of intensity ratios mentioned in (1) and (2) are determined by the ratios between the attenuation coefficients [5] μ of the X-rays of various energies. The depth of penetration at which the intensity ratio between any two X-ray components attains a value within, say 10 percent of the maximum, turns out to be inversely related to the difference between the attenuation coefficients of those components.

2.2. State of Limited Equilibrium

The approach to a steady state under the conditions of hard X-ray penetration presents the following characteristic departure from the more familiar equilibrium conditions. In the Compton effect, some of the X-rays have very nearly the same energy, the same direction, and the *same attenuation coefficient* after as before the scattering. In fact, the attenuation coefficient of some among the secondary X-ray components *differs only infinitesimally* from the attenuation coefficient of the most penetrating X-rays that are present. This circumstance does not merely slow down the approach to equilibrium, it actually suppresses the features (1) and (3) in that the intensity ratio of secondary X-ray components to a monochromatic primary may *grow beyond any limit.*

At the same time one may expect that, within a finite thickness of shield, some sort of equilibrium should be attained among those components of the secondary X-ray spectrum, whose attenuation coefficient differs from that of the most penetrating component by a sufficiently large amount. In fact, the relative intensity of most secondary components and, therefore, the average "quality" of most of the secondary radiation turn out to approach a limiting value within the thickness of a finite shield, as indicated in feature (2). On the other hand, features (1) and (3) do not obtain. The intensity ratio of this secondary radiation to the primary X-rays does not approach a maximum value, but it keeps increasing; the attenuation of the primary radiation alone does *not* control the attenuation of the secondary radiation.

In a hypothetical state of true equilibrium, the flow of radiation at great depths within a shield is described as the product of an exponential function of the depth and of a function of the energy and direction of each secondary radiation component. In the sort of steady state that is actually achieved, the flow of *most* of the secondary radiation at great depths is described as a product of a *nonexponential* function of the depth and of a function of the energy and direction of each component. Calling x the depth of penetration, measured from the source, E the energy of a photon, and θ the angle that its direction of travel forms with the x axis, E_0 the energy of the primary photons, the flux of photons of various energies and directions $\Phi(x,E,\theta)$ takes then the form

$$\Phi(x, E, \theta) \sim f(x)g(E, \theta) \tag{1}$$

when x is sufficiently large and E sufficiently smaller than E_0.

At large depths most of the energy is carried by the softer secondary components. One can, therefore, use the approximate form of the flux to evaluate the quantities of practical interest. These quantities vary, as a function of depth, in proportion to $f(x)$.

[5] The term "attenuation coefficient" is used instead of "absorption coefficient" to make it clearly understood that μ includes the effect of removal of X-rays from a narrow beam by Compton effect in addition to their true absorption by photoelectric effect or pair production.

2.3. Intensity Variation at Great Depth

The over-all attenuation of the radiation does not follow an exponential law because the most penetrating secondary components never approach an equilibrium. The determination of the over-all course of attenuation, which is described by the function $f(x)$, requires, therefore, a study of the ever developing transient process of formation and destruction of the hardest secondaries. This study constitutes the main topic of the present paper.

By centering one's attention on the formation and absorption of the most penetrating secondaries, one attains a substantial simplification of the problem. The secondaries that need be considered cover only a narrow spectral range. Therefore, the variations of the scattering and absorption cross sections within this spectral range can be treated as small quantities. Furthermore, the greatest contribution to the deep penetration arises from secondaries directed in a very narrow beam perpendicular to the source plane.[6]

However, the small differences of attenuation coefficient and of direction among the most penetrating components cannot be disregarded, even in the first approximation. On the contrary, it is just *these differences that control* the relative intensity of the various components and thereby the over-all *course of attenuation* at great depths. The following argument indicates that small changes of attenuation coefficient and of direction have comparable importance. Radiation of wavelength λ, which travels in a direction forming an angle ϑ with the axis of penetration, x, travels a distance $\Delta/\cos\vartheta$ as its distance from the source plane increases from x to $x+\Delta$. Therefore, its intensity decays along x with an effective attenuation coefficient $\mu(\lambda)/\cos\vartheta$. Compton scattering of a photon, with a wavelength shift of $\delta\lambda$ Compton units, results in a change of both $\mu(\lambda)$ and $\cos\vartheta$. If a photon starts with a wavelength λ_0 in a direction with $\theta_0=0$, $\cos\theta_0=1$, after one scattering its direction changes, according to the Compton law, to $\vartheta=\arccos[1-\delta\lambda]$ and its effective absorption coefficient from $\mu(\lambda_0)/\cos\vartheta_0=\mu(\lambda_0)$ to $\mu(\lambda_0+\delta\lambda)/[1-\delta\lambda]\sim\mu(\lambda_0)+(d\mu/d\lambda)_0\delta\lambda+\mu(\lambda_0)\delta\lambda$. The corrective term $(d\mu/d\lambda)_0\delta\lambda$ arises from the change of μ, the term $\mu(\lambda_0)\delta\lambda$ from the change of $\cos\vartheta$. The ratio of the two corrective terms is $d\log\mu/d\lambda$, with λ in Compton units, which is a number of the order of 1 for most materials and wavelengths of interest.

The importance of the small deflections was not appreciated in the early stages of the investigation, which disregarded altogether the changes of direction experienced by the most penetrating radiation components, that is, relied on the "straight-ahead approximation." The results obtained in this manner, which are reported in [2, 3] and reviewed in section 5, proved useful, nevertheless, because the effect of small deflections does not change the analytical form of the intensity variation but only the value of certain numerical constants. This simple mode of action of the deflections emerges as a result of the analytical treatment of section 7 and may be visualized as follows. Photons that travel in directions oblique to the direction of maximum penetration are selected-against in the course of deep penetration, much as if they had, in effect, a larger attenuation coefficient $\mu(\lambda)$ (see above). The selection operates simultaneously in favor of photons with near-minimum μ and near-minimum, that is, near-zero, obliquity ϑ. As a result, photons of each wavelength are concentrated in a cone of directions whose aperture is the narrower the nearer to the minimum is μ. This is to say that the effect of small obliquity merely parallels and amplifies the effect of small variations of the attenuation coefficient. Indeed, the two effects result in a fixed ratio to one another (see sections 6 and 7), so that the study of the effect of variations of μ alone, in the straight-ahead approximation, gives the correct analytical form for the trend of the total intensity at great depths.

Two different analytical forms for this trend result under different circumstances, depending on the type of variation of the attenuation coefficient among the most penetrating components. As long as the energy of the primary X-rays is not too large, none of the secondary X-rays is more penetrating than the primary X-rays. The hardest secondaries are then simply those whose energy is just a little lower than the energy of the primaries. The progressive accumula-

[6] When the whole primary radiation travels in directions oblique to the source plane, there occurs a more complicated situation that will be discussed in section 2.6 and in section 8.

ion of secondary components under these conditions has been studied in [2] under the straight-ahead approximation and in [4], taking into account the deflection effects. The intensity distribution law $f(x)$ is shown there, and in section 9, to be of the form

$$f(x)=x^K \exp(-\mu_0 x). \tag{2}$$

Here μ_0 is the attenuation coefficient of the primary X-rays and K is a number, usually of the order of 1; K depends on the cross section for Compton scattering and on the first derivative of the attenuation coefficient with respect to energy, evaluated at the energy of the primary X-rays. (For numerical values of K and the parameters on which it depends, see appendix C, tables 1 and 2.) The exponential factor represents the usual effect of attenuation of the primaries, whereas the factor x^K represents the effect of accumulation of hard secondaries and is called the "buildup factor". Numerical values of K are given in appendix C.

At very high energies, absorption by pair production increases so rapidly that higher energy X-rays are actually less penetrating than lower energy ones. Therefore, in the case of high-energy primaries, some of the secondary X-rays are more penetrating than the primaries. The attenuation of the total radiation depends upon the formation and decay of the most penetrating secondary components, whose photon energies may be much lower than that of the primaries (in lead the hardest photons have about 3-Mev energy). This phenomenon has been treated in [3] in the straight-ahead approximation, but the effect of small deflections has not been taken into account in previous papers. Both treatments are given in sections 5, 7, and 9 and show the intensity distribution law $f(x)$ to be of the form

$$f(x)=x^{-5/6} \exp[H(\mu_m x)^{\frac{1}{2}}]\exp(-\mu_m x). \tag{3}$$

Here μ_m indicates the minimum value of the attenuation coefficient, that is, the attenuation coefficient of the most penetrating X-rays in the material under consideration. The factor $\exp(-\mu_m x)$ represents the attenuation of these X-rays. The factor $x^{-5/6} \exp[H(\mu_m x)^{\frac{1}{2}}]$ is the buildup factor, corresponding to x^K in (2), and H is a constant that depends on the cross section for Compton scattering and on the values of the attenuation coefficient and of its second derivative, evaluated at the energy of the most penetrating X-rays. (For values of μ_m and H, see appendix C, table 3.)

2.4. Numerical Methods Combined With Analytical Results

The analytical results, (2) and (3), represent limiting forms of the intensity distribution, valid at extremely great depths, where the distribution depends on the generation and attenuation of an extremely narrow range of secondary spectral components. Those results must be supplemented in two directions. In the first place, one must find not only the relative X-ray intensity at different positions but the absolute intensity, particularly of lower energy components traveling in various directions, that is, the function $g(E,\vartheta)$ of eq (1). In the second place, one must be able to carry out calculations without excessively stringent limitations on the important range of secondary spectral components.

Various partially successful attempts were made to develop methods of successive approximation to take into account successively higher derivatives of the cross sections in the important spectral range. However, much greater success was eventually achieved by the semiasymptotic numerical method of Spencer [6], which fulfills both of the requirements indicated above. Additional numerical results for the X-ray distribution at moderate depths are provided by polynomial method of calculation [13].

Reliance on numerical methods to the extent of solving the transport equation numerically was dictated by the complicated dependence of the cross sections upon the X-ray energy. At the same time, since the transport equation involves three independent variables (namely distances from the source, photon energy, and direction of propagation), the reduction of the numerical burden to manageable proportion requires much guidance from qualitative analysis and as much help from analytical development as conveniently possible. Spencer has stressed

the rapid gain in computational efficiency that can be derived from general information on the desired solution [6, 14]. Economy also arises from suitable substitutions of the variables of the problem (see, for example [13]).

The space variable, depth of penetration from the source, can be separated from the other variables by a Fourier-Laplace transform. This transformation has the additional advantage of replacing the depth of penetration, which varies over a wide range, with a transform variable whose important range is narrow. As will be seen in section 4, the analytical treatment that determines the intensity distribution laws (2) and (3) deals specifically with the behavior of the distribution function at a singular point of the transform variable. The numerical method holds only for values of the transform variable at a finite distance from the singular point. The analytical treatment serves as an essential complement to determine the critical behavior at infinitesimal distances from the singularity. Furthermore, the knowledge of this analytical behavior and of the resulting behavior of the corresponding inverse transform, (the function $f(x)$ of eq (1), (2), and (3)), serves as a guide for the inverse transform procedure that is also required in the numerical work.

The two remaining variables, photon energy and direction of propagation, can be separated only within the limits of application of the analytical treatment, that is, for extremely deep penetration and narrow range of photon energies (section 7). Otherwise, the interlinkage of energy and direction offers the most serious difficulty to the solution of the problem. The difficulty has been overcome in the numerical work by learning how to take into account this interlinkage without excessive complication [6]. This is done by describing the directional distribution adequately by means of a few parameters; namely, moments when the distribution is peaked, and coefficients of a Legendre expansion when it is flat. The interlinkage of energy and direction is reviewed briefly in section 6. Numerical methods have to complement the analytical treatment even when the separation of variables succeeds in order to work out the directional distribution (section 7 and appendix B).

2.5. Verification of the Qualitative Analysis

The introductory qualitative picture of the X-ray penetration, which has led to the results indicated by eq (1), (2) and (3), has been verified to a considerable extent by experimentation and by independent numerical calculations.

Two experiments dealt with a point source of Co^{60} γ-rays surrounded by a mass of water. In the first experiment [15] ionization-chamber and Geiger-counter measurements of total intensity were made at various distances from the source. The results of these measurements should be represented, in terms of the approximate eq (1), by $f(x)\int_0^\pi 2\pi \sin\vartheta d\vartheta \int_0^\infty g(E,\vartheta)r(E)dE$, where $r(E)$ indicates the response of the measuring instrument. In the absence of information on $g(E,\vartheta)$, the plot of the measurement versus the depth of penetration x should follow the trend of the function $f(x)$. The plot does, in fact, take up the trend of (2) at great distance from the source (1.5 to 2.5 m of water), with a value of K equal to that predicted by the detailed theory of [4] and of section 7.

In the second experiment [16], the spectrum of the secondary electrons in the water was measured at various distances from the source. The plot of the number of electrons of various energies ϵ, should be represented according to eq (1) by $f(x)\int_0^\pi 2\pi \sin\vartheta d\vartheta \int_0^\infty g(E,\vartheta)R(E,\epsilon)dE$, where $R(E,\epsilon)$ indicates the probability of production of an electron of energy ϵ by a photon of energy E. Qualitatively, the shape of the plot becomes independent of the penetration depth x at great depths as predicted by (1).

Equation (1) gives no information about the shape or the absolute magnitude of $g(E,\vartheta)$. However, rather detailed calculations of the complete distribution function $\Phi(x,E,\vartheta)$, for all depths of penetration covered by the experiments can be made by the independent method of polynomial expansion [13]. These calculations have successfully predicted the quantitative results of the two experiments.

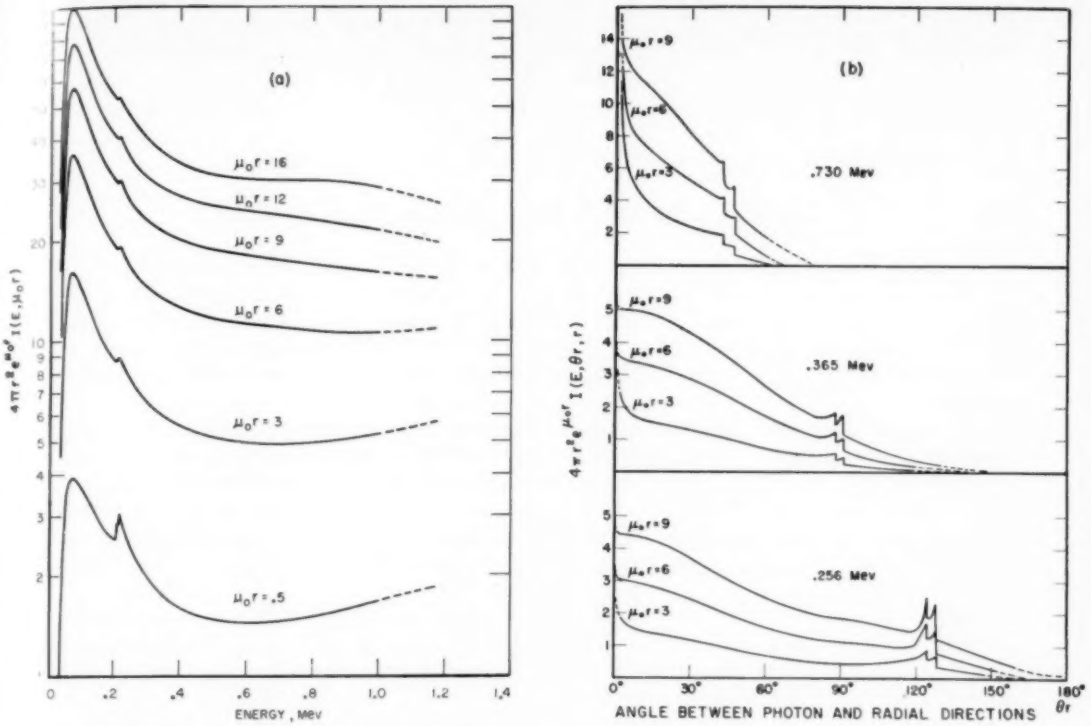

FIGURE 1. (a) *Differential spectra* $I(E,\mu_0 r)$ *of the X-ray intensity at various distances r from a* Co–60 *point isotropic source in water.*

The higher energy portions of the spectra have been omitted for clarity. The parallelism of the curves on the left side of this semilogarithmic plot indicates the trend towards equilibrium.

(b) *Directional distribution* $I(E,\vartheta_r,r)$ *of the X-ray intensity for photons of several energies E at several distances r from a point isotropic source of* Co–60 *in water.*

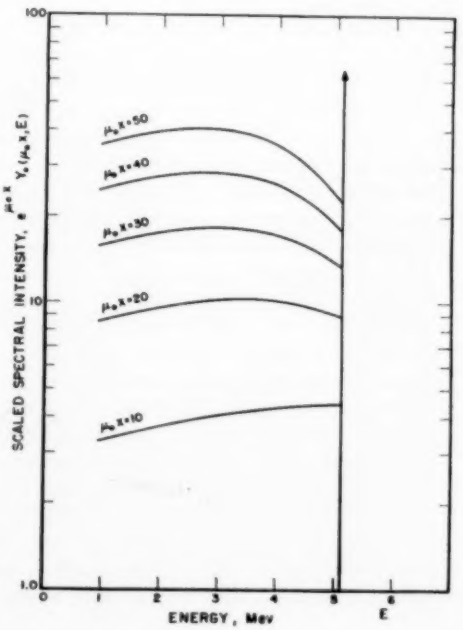

FIGURE 2. *Differential spectra* $Y_0(\mu_0 x,E)$ *at various distances x from a plane monodirectional source of 5.11 Mev photons in* Fe.

Notice the trend to parallelism on the left side as in figure 1, a.

In addition, the results of these calculations for moderately great depths provide a semi-quantitative check of the predictions of the theory of penetration to very great depths. These predictions find good verification. In particular, the trend toward an equilibrium distribution for the lower-energy secondary X-rays is clearly displayed both with respect to the spectral [13] and to the directional [17] distributions (see fig. 1). The emergence of an equilibrium state at lower energies, while the higher energy components persist in a state of nonequilibrium is most clearly displayed in the results of semiasymptotic calculations [6] (see fig. 2).

2.6. Influence of the Source Direction on the Penetration Law

Previous theoretical work on the penetration of radiation from plane sources has dealt only with isotropic sources and with sources concentrated in a direction perpendicular to the source plane. In general, one may want to deal with source radiation aimed in directions that form a fixed skew angle with the source plane. However, this new problem raises questions that are largely unsolved and that will be indicated briefly here and discussed somewhat further in section 8.

At the outset one must distinguish between the conditions where the energy of the primary X-rays lies below and above the energy of minimum attenuation (corresponding to eq (2) and (3), respectively). In the first event the penetration law is controlled by secondary X-rays of energies *just below* the source energy. The overwhelming majority of these secondary X-rays travel in directions *very nearly as oblique* as those of the primary X-rays. Therefore, the obliquity of the source has a very major influence on the intensity distribution at very great depths.

In the second case, when the source energy exceeds the energy of the most penetrating secondaries by a substantial amount, the obliquity of these secondaries is less immediately related to the obliquity of the primaries. It will be shown in section 8 that the penetration is controlled by the accumulation of secondaries that have been degraded by steps to the energy of minimum attenuation and simultaneously deflected to directions nearly perpendicular to the source plane. The absolute intensity of these secondaries depends, of course, on the obliquity of the source but their rate of accumulation and, hence, the law of deep penetration are independent thereof.

Therefore, the main difficulties arising from source obliquity occur only when the energy of the primaries lies below the energy of minimum attenuation. If ϑ_0 indicates the angle formed by the source direction with the x direction, perpendicular to the source plane, the "effective attenuation coefficient" of the primary X-rays of wave length λ_0 is $\mu(\lambda_0)/\cos\vartheta_0$ (see section 2.3). After one Compton scattering with a wavelength shift $\delta\lambda$, the obliquity ϑ is given by $\cos\vartheta=\cos\vartheta_0[1-\delta\lambda]+\sin\vartheta_0[2\delta\lambda-\delta\lambda^2]^{1/2}\cos\varphi$, where φ may have any value. Minimum effective attenuation after one scattering is obtained when $\varphi=0$, but this minimum value $\mu(\lambda_0+\delta\lambda)/<\cos\vartheta>_{max}$ may be larger or smaller than the initial value $\mu(\lambda_0)/\cos\vartheta_0$, depending on the values of $d\mu/d\lambda$ and of ϑ_0. The most favorable reduction of the effective attenuation coefficient is brought about by a succession of scatterings with infinitesimal $\delta\lambda$'s, all directed so as to reduce ϑ. An infinite sequence of such scatterings would eventually bring about a deflection all the way to $\vartheta=0$ without any finite increase of μ, but the probability of such an event is, of course, infinitesimal of a high order. Nevertheless, an unlikely process of this kind must determine the penetration at extremely great depths. That is the penetration will be eventually controlled by the scanty accumulation of secondary X-rays with energies very near the primaries and direction nearly perpendicular to the source plane, that is, with effective attenuation coefficients near μ_0. The course of accumulation of secondary X-rays that are effectively more penetrating than the primaries because of reduced obliquity has not yet been studied. Knowledge of the limiting trend at extremely great depths may not be very important because it may not even become recognizable except under unrealistic conditions. Nevertheless, lack of understanding of this process may undermine the effectiveness of the semiasymptotic and polynomial methods of calculation, whose application is now being planned.

If the source emits X-rays of various obliquities, some of which travel initially in the direction perpendicular to the source plane, it will be just the X-rays in this direction and their secondaries that achieve great penetration. Deeper and deeper penetrations arise from narrower and narrower bundles of primary X-rays. Therefore, a source with a broad distribution of directions contributes less and less toward deep penetration, as compared to a source aimed exactly in the direction perpendicular to the source ($\vartheta_0=0$). This argument will be confirmed by the analytical treatment of section 8. In particular an isotropic source, or any source with practically uniform distribution in directions nearly perpenducilar to the source plane, yields an intensity distribution law in accordance with eq (2) but with a value of K lower by 1 than the value for a source concentrated at $\vartheta_0=0$ [6].

3. Transport Equation

The following symbols will be used:

$\boldsymbol{r}=(x,y,z)=$coordinates of a point of a medium.

$\lambda=$wavelength of a photon in Compton units (h/mc).

$\boldsymbol{u}=(u_x,u_y,u_z)=(\vartheta,\varphi)=$unit vector indicating a photon direction.

$\mu(\lambda)=$total (narrow-beam) attenuation coefficient of the medium for photons of wavelength λ.

$\mu_{Th}=$Thomson scattering coefficient (probability per unit path) of the medium= low energy limit of the integral Klein-Nishina coefficient.

$k(\lambda',\lambda)=(3/8)\mu_{Th}[\lambda'/\lambda+\lambda'^3/\lambda^3+(\lambda'/\lambda)^2(\lambda-\lambda'-2)(\lambda-\lambda')]=$Klein-Nishina differential scattering coefficient of the medium for Compton scattering with a wavelength change from λ' to λ, per unit λ, for $\lambda'\leq\lambda\leq\lambda'+2$.

$Y(\boldsymbol{r},\boldsymbol{u},\lambda)=$number of photons per unit volume, per unit solid angle and per unit λ.

$\delta(\xi)=$Dirac's delta function.

$\lambda_0=$ wavelength of the source photons (if monochromatic).

$\mu_0=\mu(\lambda_0)$.

$\lambda_s=$wavelength of the photons whose attenuation coefficient has the lowest value in the range of integration from λ_0 to λ.

$\mu_s=\mu(\lambda_s)$.

$\lambda_m=$wavelength of the photons whose attenuation coefficient is the absolute minimum in the medium under consideration.

$\mu_m=\mu(\lambda_m)$.

The degradation, penetration, and diffusion of X-rays is governed by a transport equation. This equation represents the rate of change of the density of photons with a specified direction and wavelength, from one point to the next in the direction of propagation, as the sum of three terms namely: (a) the attenuation of the photon density as a result of absorption and scattering, (b) the addition of photons that take up the specified direction and wavelength as a result of Compton scattering, (c) the addition of photons with the specified direction and wavelength from the source. The equation is:

$$\boldsymbol{u}\cdot\boldsymbol{grad}\,Y(\boldsymbol{r},\boldsymbol{u},\lambda)=-\mu(\lambda)\,Y(\boldsymbol{r},\boldsymbol{u},\lambda)$$
$$+\int_{\lambda-2}^{\lambda}d\lambda' k(\lambda',\lambda)\int_{4\pi}d\boldsymbol{u}'\;(2\pi)^{-1}\delta(1-\boldsymbol{u}\cdot\boldsymbol{u}'-\lambda+\lambda')\;Y(\boldsymbol{r},\boldsymbol{u}',\lambda')+S(\boldsymbol{r},\boldsymbol{u},\lambda), \qquad (4)$$

where $S(\boldsymbol{r},\boldsymbol{u},\lambda)$ represents the source, that is, the density of photons produced at $\boldsymbol{r}$ with the direction $\boldsymbol{u}$ and the wavelength λ. The δ-function represents the Compton law which requires λ to equal $\lambda'+(1-\boldsymbol{u}\cdot\boldsymbol{u}')$.

Following the plan indicated in the introduction, we assume that the source distribution has a plane symmetry, that is, that it does not depend on y and z, nor on the component φ of $\boldsymbol{u}$, (but only on $\vartheta=\arccos u_x$). As a result, Y will be similarly independent of y,z and φ. We also

assume that the source is concentrated on the plane $x=0$ and at a wavelength $\lambda=\lambda_0$, but this constitutes no real restriction owing to the linearity of the equation. Accordingly, we have $S(\boldsymbol{r},\boldsymbol{u},\lambda)=\delta(x)\delta(\lambda-\lambda_0)f(u_x)$ and the equation reduces to

$$u_x\partial Y(x,u_x,\lambda)/\partial x=-\mu(\lambda)Y(x,u_x,\lambda)$$
$$+\int_{\lambda-2}^{\lambda}d\lambda' k(\lambda',\lambda)\int_{4\pi}d\boldsymbol{u}'(2\pi)^{-1}\delta(1-\boldsymbol{u}\cdot\boldsymbol{u}'-\lambda+\lambda')Y(x,u_x',\lambda')+\delta(x)\delta(\lambda-\lambda_0)f(u_x). \quad (5)$$

Notice that the kernel $k(\lambda',\lambda)$ of this equation may be multiplied by any ratio $g(\lambda')/g(\lambda)$, provided Y is suitably renormalized.

4. Fourier-Laplace Transform

The transform method involves a separation of variables. It represents the X-ray distribution as a superposition of components, each of which has a certain angular and spectral distribution *uniform* over all the space. The intensity of each component varies exponentially or sinusoidally from point to point according to $\exp(-px)$, where p may be complex.[7]

The transform and its inverse are:

$$y(p,u_x,\lambda)=\int_{-\infty}^{\infty}\exp\,(px)Y(x,u_x,\lambda)dx, \quad (6)$$

$$Y(x,u_x,\lambda)=(2\pi i)^{-1}\int_{-i\infty}^{+i\infty}\exp\,(-px)y(p,u_x,\lambda)dp. \quad (7)$$

The transform method of analysis consists of two steps: (a) A study of the directional and spectral distribution $y(p,u_x,\lambda)$ for various values of p, (b) an evaluation of the inverse transform integral (7).

The evaluation of the integral may proceed by the path of steepest descent. Whether this method is eventually followed or not, an analysis of the "topography" of the transform $y(p,u_x,\lambda)$, that is, of the distribution of its absolute values over the complex plane p proves very useful. This analysis indicates what region of the plane yields the largest contribution to the integral when the steepest descent method is followed. The determination of $y(p,u_x,\lambda)$ in this region, which is often very limited, proves anyhow to be very efficient for evaluating the inverse transform.

The equation that governs the directional and spectral distribution $y(p,u_x,\lambda)$, for each value of p, derives from (5) by means of the transformation (6), that is, by multiplication by $\exp(px)$ followed by integration. This equation is:

$$[\mu(\lambda)-pu_x]y(p,u_x,\lambda)=\int_0^{\lambda}d\lambda' k(\lambda',\lambda)\int_{4\pi}d\boldsymbol{u}'(2\pi)^{-1}\delta(1-\boldsymbol{u}\cdot\boldsymbol{u}-\lambda+\lambda')y(p,u_x',\lambda')+\delta(\lambda-\lambda_0)f(u_x). \quad (8)$$

The source term in this equation does not depend on p because the source term in (5) is concentrated on the plane $x=0$.

Because the wavelength of a photon increases as a result of Compton scattering, the distribution of photons of each wavelength λ depends on the distribution of photons of shorter wavelengths λ' but not on that of longer wavelength photons. If one knows the photon distribution (in spectrum and direction) at all wavelengths $\lambda'<\lambda$, one can evaluate the integral in (8) and thereby find the distribution $y(p,u_x,\lambda)$ on the left side of the equation. Thus eq (8) may be solved in principle stepwise, proceeding from the source wavelength λ_0 to longer and longer wavelengths. This procedure, which reflects the course of the physical process of energy degradation, points to an important effect. If the intensity of X-rays of a certain wavelength builds up to a high value, Compton scattering of these X-rays *builds up*, in turn, the intensity of *all longer wavelength* radiation.

---

[7] Notice that p has here a sign opposite to that which is most common in the literature. The convention adopted here proves convenient in problems of penetration and straggling.

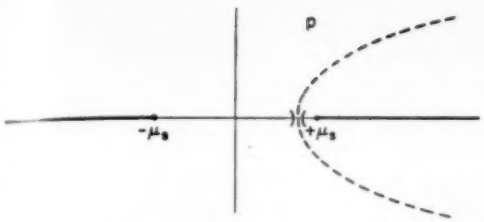

FIGURE 3. *Elements of a relief map diagram of the transform distribution y on the plane of the complex variable p.*

——, Lines over which $y(p)$ is singular; – – –, trend of the steepest descent line of $y(p)\exp(-px)$ for positive p;) (, approximate position of the saddle-point.

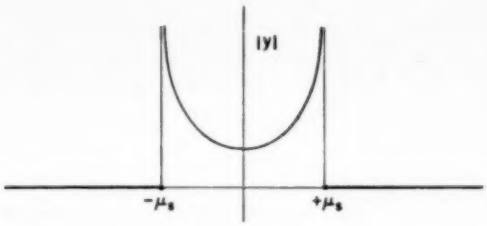

FIGURE 4. *Diagram of a plot of $|y(p)|$ along the real axis of figure 3.*

Equation (8) shows that $y(p,u_x,\lambda)$ becomes infinitely large when $\mu(\lambda)-pu_x$ vanishes. Furthermore, y grows rapidly for those combinations of p,u_x and λ for which $\mu(\lambda)-pu_x$ is particularly small. These combinations of variables are critical in various respects. We just mentioned that once $y(p,u_x,\lambda)$ has become very large for certain values of u_x and λ, it remains correspondingly large for all longer wavelengths. We also know that the distribution of large values of $y(p,u_x,\lambda)$ determines the path of steepest descent of the integral (7). Finally, the process of numerical integration becomes increasingly difficult as the rate of rise of $y(p,u_x,\lambda)$ increases, so that one may want to utilize, at least locally, analytical methods of solution.

The coefficient $\mu(\lambda)-pu_x$ of (8) vanishes only for positive real values of p larger than $\mu(\lambda)$ or for negative real values smaller than $-\mu(\lambda)$. Therefore, eq (8) becomes singular only for values of the complex variable p which are confined to the sections of the real axis marked heavily in figure 3. The lines terminate at $p=\pm\mu_s$, where μ_s indicates the smallest value of $\mu(\lambda')$ in the range of wavelengths from λ_0 to λ. There appears to be no other point in the plane p where $y(p,u_x,\lambda)$ diverges.

Figure 4 shows a schematic plot of $|y|$ against real values of p. The plot rises to infinity at $p=\pm\mu_s$, where the equation has become singular for $u_x=1$ and for the wavelength $\lambda_s\leq\lambda$ at which μ takes its smallest value μ_s.

The integrand of (7) equals $y(p,u_x,\lambda)$ times $\exp(-px)$. The factor $\exp(-px)$, regarded as a function of p, slopes down to the right for positive values of x and to the left for negative values. The slope increases in proportion to the distance from the source, $|x|$. Therefore the integrand has a minimum, for real p, where $\partial \log y(p,u_x\lambda)/\partial p=x$, that is, at a point that approaches $p=\mu_s$ when x is large and positive, or $p=-\mu_s$ when x is large and negative.

This lowest point of $\exp(-px)y(p,u_x\lambda)$ against *real* values of p constitutes the one and only saddle point along the steepest descent path when $\exp(-px)y(p,u_x,\lambda)$ is integrated with respect to the *complex* variable p (see fig. 3).

The minimum and the saddle are sharp when $|x|$ is large. Under these conditions, a knowledge of $y(p,u_x,\lambda)$ over a narrow range of *real* values of p suffices to evaluate the integral (7) and thus to calculate the total distribution of X-rays far from the source. The main object of this paper is just to study the trend of y for real values of p near μ_s (or $-\mu_s$). Section 9 deals with the actual evaluation of the integral (7).

For smaller values of the depth of penetration x, the saddle point lies nearer to $p=0$. The direct calculation of $Y(x,u_x,\lambda)$ at moderate depths also provides convenient expansions of y in powers of p, or of related variables like $p/(\mu_s-p)$ and $p^2/(\mu_s^2-p^2)$ [13]. This information may serve to interpolate y between the proximity of $p=0$ and of $p=\pm\mu_s$.

5. Special Analytical Solutions—Straight-ahead Approximation

In order to study the trend of y for real values of p near μ_s, we seek approximate analytical solutions of the transform equation (8) valid for values of $\lambda\sim\lambda_s$ and of $u_x\sim1$. This search will be conducted first in the straight-ahead approximation even though this approximation is inadequate.

The straight-ahead approximation consists of setting $u_x=1$ on the left side of (5) or (8). This procedure is equivalent to the replacement of the depth of penetration x in (5) with the path length traveled by the photons, irrespective of the obliquity of penetration [18]. The variables u_x and $\boldsymbol{u}$ that still remain in the eq (8) can then be eliminated by integrating over $\boldsymbol{u}$. Setting

$$\int_{4\pi} d\boldsymbol{u}\, y(p,u_x,\lambda)=\Phi(p,\lambda), \tag{9}$$

we obtain the straight-ahead approximation equation

$$[\mu(\lambda)-p]\Phi(p,\lambda)=\int_{\lambda_0}^{\lambda} k(\lambda',\lambda)\Phi(p,\lambda')d\lambda'+\delta(\lambda-\lambda_0)\mathrm{I}, \tag{10}$$

where $\mathrm{I}=\int_{4\pi} f(u_x)d\boldsymbol{u}$.

Because we are interested in an approximate solution valid over a narrow range of variation of λ, we disregard the variations of the differential scattering coefficient k over an interval $\lambda'\sim\lambda$ and take

$$k(\lambda',\lambda)\sim k(\lambda,\lambda)=(3/4)\mu_{Th}=C, \tag{11}$$

in agreement with the definition of k (see section 3).

Before entering this approximation into (10), we must distinguish two different situations, as in section 2.3. (a) If the primary radiation is the most penetrating one, that is, if $\mu_x=\mu(\lambda_0)=\mu_0$, the range of approximate integration over λ is right next to the source wavelength λ_0. (b) If the most penetrating radiation is that of wavelength λ_m, for which μ has its absolute minimum value $\mu_m=\mu(\lambda_m)$, that is, if $\lambda_0<\lambda_m$, the range of approximate integration cannot run all the way from λ_0 to λ_m. In this event, we do not attempt to solve the inhomogeneous equation (10), but only the corresponding homogeneous equation, in the range of $\lambda\sim\lambda_m$.

Therefore, we seek the solution of

$$[\mu(\lambda)-p]\Phi(\lambda,p)=C\int_{\lambda_0}^{\lambda}\Phi(\lambda',p)d\lambda'+\mathrm{I}\,\delta(\lambda-\lambda_0)$$

for

$$\lambda\sim\lambda_0>\lambda_m, \tag{12a}$$

and of

$$[\mu(\lambda)-p]\Phi(\lambda,p)=C\int^{\lambda}\Phi(\lambda',p)d\lambda'$$

for

$$\lambda\sim\lambda_m>\lambda_0. \tag{12b}$$

These equations reduce to differential form, if a derivative is taken with respect to λ, and their solutions are

$$\Phi(\lambda,p)=\mathrm{I}(\mu_0-p)^{-1}C\,[\mu(\lambda)-p]^{-1}\exp\left\{C\int_{\lambda_0}^{\lambda}d\lambda'/[\mu(\lambda')-p]\right\} \tag{13a}$$

$$\Phi(\lambda,p)=C\,[\mu(\lambda)-p]^{-1}\exp\left\{C\int^{\lambda}d\lambda'/[\mu(\lambda')-p]\right\}. \tag{13b}$$

These solutions are derived as special cases of a more general procedure in [18 section 11b].

We are interested in the behavior of these solutions when p approaches the singular point μ_s, that is, μ_0 in (13a) and μ_m in (13b).

In case (a) the first derivative of $\mu(\lambda')$ at the singular point μ_0, $(d\mu/d\lambda')_0=\dot{\mu}_0$, is different from zero. Therefore, the integral in the exponent of (13a) has a logarithmic singularity. In case (b) the first derivative of $\mu(\lambda')$ vanishes at $\mu(\lambda')=\mu_m$, $\lambda'=\lambda_m$. Therefore the integral in the exponent of (13b) over an interval of $\lambda'\sim\lambda_m$ is of the arctangent type and its singularity has the form $(\mu_m-p)^{-1/2}$. If $\mu(\lambda')$ is regarded as linear in case (a) and parabolic in case (b), the solutions (12) take the characteristic singular forms [3]:

$$\Phi(\lambda,p)\sim \mathrm{I}(\mu_0-p)^{-1}C\,[\mu(\lambda)-p]^{-1}\exp\left\{\frac{C}{\dot{\mu}_0}\log\frac{\mu(\lambda)-p}{\mu_0-p}\right\}=\mathrm{I}C\,[\mu(\lambda)-p]^{C/\dot{\mu}_0-1}[\mu_0-p]^{-C/\dot{\mu}_0-1} \quad (14a)$$

$$\Phi(\lambda,p)\sim C\,[\mu(\lambda)-p]^{-1}\exp\{2\pi C/[2\ddot{\mu}_m(\mu_m-p)]^{1/2}\}, \quad (14b)$$

where $\ddot{\mu}_m=(d^2\mu/d\lambda^2)_{\lambda m}$.

Even though the solution of the transform equation (10) for values of $\lambda>>\lambda_s$ cannot be obtained in this simple manner, its dependence on p, as p approaches μ_s, is described by (14) for the following reason. As soon as λ is sufficiently larger than λ_s so that $\mu(\lambda)-p>>\mu_s-p$, p may be replaced in the equation by μ_m. This implies that the further variations of $\Phi(\lambda,p)$, as λ keeps increasing, are independent of p, that is, that a state of limited equilibrium, within the meaning of section 2.2, has been achieved. As p approaches μ_s, λ need depart from λ_s less and less, before the condition $\mu(\lambda)-p>>\mu_s-p$ is adequately fulfilled. Therefore the approximations made in the derivation become increasingly good.

The inversion of Laplace transforms with the singularities (14a) and (14b) will be considered in section 9. However, we anticipate here that the inverse transforms behave, respectively, as (2) and (3) for large depths of penetration x.

For the sake of completeness, we mention yet another situation, which combines the features of (a) and (b), namely, the case where $\lambda_0<\lambda<\lambda_m,\lambda_s=\lambda$. Here the pertinent form of the equation is (12b) and its solution (13b). However, the derivative $(d\mu/d\lambda)_s$ at $\lambda=\lambda_s$ is different from zero. Hence, the integral in the exponent of (13b) has a logarithmic singularity and we find, instead of (14b),

$$\phi(\lambda,p)\sim C\,[\mu(\lambda)-p]^{C/\dot{\mu}_s-1}. \quad (14c)$$

Various attempts were made in the past to develop methods of successive approximations, starting from the approximate solutions (13) and (14), to solve the straight-ahead equation (9) for all values of λ. Direct numerical integration eventually proved superior [6], even for values of p rather near μ_s, despite the fact that the rapid rise of y along λ, for λ near λ_s, requires small steps of numerical integration.

6. Possible Treatments of the Obliquity of Penetration

As pointed out in section 2.3, the deep penetration of X-rays is influenced to a substantial extent by the small obliquity of the most penetrating components. In order to evaluate this effect, one must, in principle, work out the directional distribution of the X-rays of each wavelength, that is, solve the complete two-variable equation (8). In practice, one may want to learn about the distribution-in-angle only the least amount necessary to evaluate the effect on the trend of penetration.

In order to analyze this situation, one may expand the distribution-in-angle of $y(p,u_x,\lambda)$ into Legendre polynominals $P_l(u_x)$,

$$y(p,u_x,\lambda)=\sum_l(2l+1)(4\pi)^{-1}y_l(p,\lambda)P_l(u_x). \quad (15)$$

with

$$y_l(p,\lambda)=\int_{4\pi}d\boldsymbol{u}P_l(u_x)y(p,u_x,\lambda). \quad (16)$$

Equation (6) multiplied by each of the P_l's and integrated, reduces to the system of equations

$$\begin{aligned}
&\mu(\lambda)y_0(p,\lambda)-py_1(p,\lambda)=\int_{\lambda_0}^{\lambda}k(\lambda',\lambda)y_0(p,\lambda')d\lambda'+\delta(\lambda-\lambda_0)\int_{4\pi}f(u_x)d\boldsymbol{u}\\
&\quad\cdots\cdots\cdots

The first equation of this system has the same form as the straight-ahead equation (10), except for the fact that y_1 appears in the second term on the left side instead of y_0. If there were a way of guessing the ratio

$$y_1(p,\lambda)/y_0(p,\lambda)=\int_{4\pi} u_z y(p,u_z,\lambda)d\boldsymbol{u}/\int_{4\pi} y(p,u_z,\lambda)d\boldsymbol{u}=\bar{u}_z(p,\lambda), \tag{18}$$

y_1 could be replaced with $\bar{u}_z(p,\lambda)y_0(p,\lambda)$ in the first eq. (17), which could then be solved as a single-variable-straight-ahead equation. Thus a knowledge of $\bar{u}_z(p,\lambda)$, or of an equivalent parameter, embodies all the information about the directional distribution that is immediately relevant to the penetration problem.

Instead of $\bar{u}_z$ one may want to use the equivalent parameter [6]

$$g_1(p,\lambda)=1-\bar{u}_z(p,\lambda)=\int_{4\pi}(1-u_z)y(p,u_z,\lambda)d\boldsymbol{u}/\int_{4\pi} y(p,u_z)d\boldsymbol{u}, \tag{19}$$

which represents the first moment of the angular distribution. If we set $y_1=(1-g_1)y_0$ in (17), the first equation becomes

$$[\mu(\lambda)-p+pg_1(p,\lambda)]y_0(p,\lambda)=\int_{\lambda_0}^{\lambda} k(\lambda',\lambda)y_0(p,\lambda')d\lambda'+\delta(\lambda-\lambda_0)\int_{4\pi} f(u_z)d\boldsymbol{u}. \tag{20}$$

Thus, $g_1(p,\lambda)$ is seen to measure the departure of the eq (20) from the straight-ahead eq (10).

In the critical range of wavelengths, $\lambda\sim\lambda_s$, the solution of (20) may be expressed in a manner similar, for example, to (13b), that is,

$$y_0(p,\lambda)\sim C[\mu(\lambda)-p+pg_1(p,\lambda)]^{-1}\exp\left\{C\int^{\lambda} d\lambda'/[\mu(\lambda')-p+pg_1(p,\lambda')]\right\}$$

$$=\frac{C[\mu(\lambda)-p]^{-1}}{1+pg_1(\lambda,p)/[\mu(\lambda)-p]}\exp\left\{\int^{\lambda}\frac{C}{1+pg_1(p,\lambda')/[\mu(\lambda')-p]}\frac{d\lambda'}{\mu(\lambda')-p}\right\} \tag{21}$$

The last expression differs from (13b) in that C is now divided by $1+pg_1(\lambda,p)/[\mu(\lambda)-p]$. We shall see in the next section that this factor tends to a constant limit as p approaches the singular point μ_s.

If the ratio $\bar{u}_z=y_1/y_0$ is assumed to be known, y_0 can be calculated, and thereby y_1 becomes also known. The second equation (17) yields then y_2 directly, the third yields y_3, and so on, that is, the whole system of equations unravels automatically. It was pointed out by Wick [1], and also by Waller [19], that the set of values thus obtained for the y_l, diverges, in general, unless the correct value of $\bar{u}_z$ was chosen at the start. Thus the solution of the system (17) takes the character of an eigenvalue problem. (This property is common to all systems of which the first n equations contain $n+1$ unknowns).

A simple trial and error procedure on the choice of $\bar{u}_z=y_1/y_0$ in (17) is impractical in the critical range of λ where the directional distribution is sharply peaked forward and the successive coefficients y_l, y_{l+1} . . . are nearly equal, so that the trend of the sequences y_l evolves exceedingly slowly. In other words, the angular distribution cannot be characterized in this range by just a few Legendre coefficients. Therefore Wick [1] replaced the sequence of the y_l's with a continuous function and the expression $[(l+1)y_{l+1}+ly_{l-1}]/(2l+1)-y_l$ in (17) with the second derivative of the function. In this manner the problem of determining the value of $\bar{u}_z=y_1/y_0$ was reduced to a problem of differential equations. An approximate determination of the eigenvalue by variational methods offers little difficulty and was carried out by Wick for a constant μ (λ) and for a linear $\mu(\lambda)$ [1].

Whereas variational methods are well suited for deriving rapidly an approximate eigenvalue, they tend to yield poorer approximations to the eigenfunctions and generally do not appear convenient as a basis for higher approximations. In fact, Wick effectively characterizes the angular distribution of radiation by a single adjustable parameter, in the first approxima-

ion. A substantially better approximation is required to take into account more general variations of μ (λ) as well as variations of the kernel k (λ', λ). Extensions of Wick's procedure in this direction have been developed but they appear cumbersome.

When the directional distribution is sharply peaked, as it is in the critical range, $\lambda \sim \lambda_s$, it can be characterized conveniently by its set of moments, which in this case tend to converge far more quickly than the set of Legendre coeffcients y_l. The moments, $m_0 = y_0$, $m_1 = g_1 y_0 = y_1 - y_0$, . . . $m_n = \int_{4\pi} (1-u_z)^n y(p, u_z, \lambda) d\boldsymbol{u}$ are linear combinations of the Legendre coefficients. Determinations of g_1 by trial and error procedures based on calculations of the m_n's should be more practical than procedures based on the y_l's.

Spencer eventually developed an efficient iteration procedure that permits to determine g_1 by trial and error, utilizing only a very few—as few as two—of the equations for the moments [6]. This method has superseded all previously attempted approaches.

One point, which emerged in the course of earlier attempts, might be worth mentioning because of its possible more general interest. The testing of trial values of $g_1(p,\lambda)$ becomes particularly easy when the obliquity of penetration is less effective than the variations of $\mu(\lambda)$ in shaping the X-ray spectrum, that is, according to section 2.3, when $d \log \mu / d\lambda < 1$. In this event, an incorrect initial assumption regarding g_1, not only causes the sequence of moments $m_1, m_2 \ldots m_n \ldots$ eventually to diverge, but quickly to assume a grossly erratic trend. This critical instability appears to be a general property of systems that may be called "strongly nonself-adjoint." It is discussed in appendix B.

7. Effects of Small Deflections on Special Analytical Solutions

As mentioned in section 6, Wick did the basic work on the effect of small deflections on penetration [1], for two typical situations, namely, constant $\mu(\lambda)$ and linear $\mu(\lambda)$. Either of these assumptions about μ, together with the assumption (11) of a constant kernel $k(\lambda', \lambda)$, makes it possible to separate the direction variable u_z from the energy variable λ in the transform equation (8).

Specifically, the homogeneous part of the equation thus simplified has solutions that are products of a function of λ and of a function of $(1-u_z)p/[\mu(\lambda)-p]$. This to say that the directional distribution maintains a constant *shape* as λ varies, but it contracts in width, as $\mu(\lambda)-p$ grows smaller, in proportion to $[\mu(\lambda)-p]/p$. As a result, the factor $1+pg_1(\lambda,p)/[\mu(\lambda)-p]$ in (21) remains *independent of* λ *and* p. Therefore, the dependence of the photon number on λ and p, irrespective of direction, which is given by (21), has *the same analytical form as the straight-ahead* approximation (13b), except that C is replaced with the constant $C/\{1+pg_1/(\mu-p)\}$. There is a whole set of solutions of the homogeneous equation, with different values of $pg_1/(\mu-p)$.

Wick superposes solutions of this set so as to construct a solution of the inhomogeneous equation with the $\delta(\lambda-\lambda_0)$ source. The component solution with the smallest value of $pg_1/(\mu-p)$ predominates over the other components as p approaches μ_s and as λ increases through the critical range $\lambda \sim \lambda_s$. Therefore, the singularity of the Laplace transform is characterized by the variation of $\mu(\lambda)-p$ in (21) (or in (13b)) as p approaches μ_s and by the smallest value of $pg_1/(\mu-p)$.

The application of this procedure to the X-ray problem is straightforward when the primary radiation is the most penetrating one ($\lambda_0 > \lambda_m$, $\mu_s = \mu_0$) [4], since in the very proximity of λ_0 the variations of $\mu(\lambda)$ may well be regarded as linear, $\mu(\lambda) \sim \mu_0 + \dot{\mu}_0(\lambda-\lambda_0)$, and those of $k(\lambda', \lambda)$ may be disregarded.

The applicability is less clear when the primary radiation is not the most penetrating one ($\lambda_0 < \lambda_m$), that is, when $\mu(\lambda)$ goes through a minimum in the critical range. However, one may surmise that the problem at the minimum ($\lambda \sim \lambda_m$) can be treated by assuming the same value of $pg_1/(\mu-p)$ *as though* $\mu(\lambda)$ were constant. This assumption, which has not been discussed previously, implies that the singularity of the transform is given by the straight-ahead formula (14b) with C replaced with the value of $C/\{1+pg_1/(\mu-p)\}$ corresponding to a constant μ.

We present here first a qualitative argument and then a more detailed treatment which confirm the correctness of the surmise.

The trend of the solution of the transform equation in the critical range depends on the variations of the attenuation coefficient $\mu(\lambda)$ and on the effect of small deflections. We want to show that the deflection effects predominate over the variations of $\mu(\lambda)$, in the limit as p approahces μ_m, so that the deflection effects may be treated as though $\mu(\lambda)$ had the constant value μ_m.

Obliquity of penetration effectively impedes the build-up of photons if the value of $\mu - pu_x$ in (7) becomes substantially larger than the corresponding "straight-ahead" value $\mu - p$. Therefore, the main build-up is confined to photons for which $1-u_x \leq (\mu-p)/p$. Compton scattering of photons within this range of directions corresponds to wavelength shifts $\delta\lambda \leq 1-u_x \leq (\mu-p)/p$.

On the other hand, variations of the absorption coefficient that affect the asymptotic behavior must be of the order $\Delta\mu \sim \mu_m - p$. These variations may be described, in the neighborhood in the minimum, as $\Delta\mu \sim \frac{1}{2}\ddot{\mu}_m \Delta\lambda^2$ (where $\ddot{\mu}_m = (d^2\mu/d\lambda^2)_m$). Therefore, the wavelength change $\Delta\lambda$ required to bring about a substantial change of μ is of the order of magnitude $[2(\mu_m - p)/\ddot{\mu}_m]^{1/2}$.

Hence, in the limit for $\mu_m - p \to 0$, this shift $\Delta\lambda$ becomes proportionately much larger than the shift $\delta\lambda$ required to bring about substantial effects of obliquity.

Proceeding beyond this qualitative argument, a complete treatment of the problem would consist of solving the transform equation (8) by a procedure of successive approximations, whose first step should yield the Wick-type results. Efforts in this direction have yielded rather cumbersome developments. In practice such a complete treatment has been made unnecessary by the development of the semiasymptotic numerical method [6] (see section 2.4), which requires, as an analytical complement, only a knowledge of the singularity at $p=\mu_s$, $u_x=1$. One possible approach to the remaining problem would be to seek a special solution of the eq (8) for the case when the primary radiation is *not* the most penetrating one, that is, when $\lambda_0 < \lambda_m$, $\mu_s = \mu_m$, since Wick has already solved the problem for $\lambda_0 > \lambda_m$, $\mu_s = \mu_0$. Whereas Wick assumed a linear variation of μ, near $\lambda = \lambda_0$, we should assume here a parabolic variation near $\lambda = \lambda_m$, that is, $\mu(\lambda) \sim \mu_m + \frac{1}{2}\ddot{\mu}_m(\lambda - \lambda_m)^2$. Instead of following this approach, we shall take a somewhat more general one, namely, to seek special solutions of the equation valid "in the asymptotic limit"

$$[\mu(\lambda) - p]/p \to 0, \tag{22}$$

that is, for $\lambda \sim \lambda_s$, $u_x \sim 1$. This will be done without utilizing any initial approximation about $\mu(\lambda)$ or $k(\lambda', \lambda)$ but the approximations considered above will result automatically from the consistent application of the limit process.

The first step of our treatment consists in choosing instead of u_x a new direction variable that measures the effect of obliquity on penetration. Equation 21 shows that this effect is proportional to the mean value of $p(1-u_x)/[\mu(\lambda)-p]$. Accordingly, we replace the unit space vector $\boldsymbol{u} = (\vartheta, \varphi)$ with a homolographic projection variable that is represented in plane polar coordinates by the vector

$$\boldsymbol{v} = ([2p(1-u_x)/(\mu-p)]^{1/2}, \varphi) \sim ([p/(\mu-p)]^{1/2}\vartheta, \varphi). \tag{23}$$

(The approximate equality corresponds to the small angle approximation $\vartheta << 1$, which we need not utilize at this point.) The inverse transformation of (23) is

$$u_x = 1 - \tfrac{1}{2}v^2[\mu(\lambda) - p]/p, \qquad \boldsymbol{u}(\boldsymbol{v}, \lambda) = (\arccos u_x, \varphi). \tag{24}$$

It is also convenient, though not essential, to renormalize the dependent variable $y(p, u_x, \lambda)$ by multiplication with $\mu(\lambda) - p$, that is, to take

$$w(v, \lambda) = [\mu(\lambda) - p]y(p, u_x, \lambda). \tag{25}$$

The dependence of w on p will not be indicated explicitly.

The transform equation (8) takes now the form

$$(1+\tfrac{1}{2}v^2)w(v,\lambda)=(2\pi p)^{-1}\int_0^\lambda d\lambda' k(\lambda',\lambda)\int d\boldsymbol{v}'\delta(1-\boldsymbol{u}\cdot\boldsymbol{u}-\lambda+\lambda')w(v',\lambda')+\mathrm{I}\,\delta(\lambda-\lambda_0)f(u_x)$$

$$=(2\pi p)^{-1}\int d\boldsymbol{v}' k(\lambda-\Lambda[\lambda,\boldsymbol{v},\boldsymbol{v}'],\lambda)w(v',\lambda-\Lambda[\lambda,\boldsymbol{v},\boldsymbol{v}'])+\mathrm{I}\,\delta(\lambda-\lambda_0)f(1-\tfrac{1}{2}v^2(\mu_0-p)/p), \tag{26}$$

where Λ stands for $1-\boldsymbol{u}\cdot\boldsymbol{u}'$. Since $\boldsymbol{u}$ is given by (24) as a function of $\boldsymbol{v}$ and λ, and similarly $\boldsymbol{u}'$ as a function of $\boldsymbol{v}'$ and $\lambda'=\lambda-\Lambda$, $\Lambda(\lambda,\boldsymbol{v},\boldsymbol{v}')$ is defined as the root of the equation

$$\Lambda=1-\boldsymbol{u}(\boldsymbol{v},\lambda)\cdot\boldsymbol{u}'(\boldsymbol{v}',\lambda-\Lambda). \tag{27}$$

We are now interested in the solutions of (26) in the critical region $\lambda\sim\lambda_s$, $\mu(\lambda)\sim\mu_s$ and in the asymptotic limit $[\mu(\lambda)-p]/p\sim 0$. Following Wick, we seek here solutions of the homogeneous equation corresponding to (26), that is, of

$$(1+\tfrac{1}{2}v^2)w(v,\lambda)=(2\pi p)^{-1}\int d\boldsymbol{v}' k(\lambda-\Lambda,\lambda)w(v',\lambda-\Lambda), \tag{28}$$

and leave it for the next section to superpose solutions of (28) in such a manner as to fulfil the inhomogeneous equation (26) at the source where $\lambda=\lambda_0$.

Our knowledge of the straight-ahead solution and the discussion of section 6 on the effect of small deflection suggest that we split off from $w(v,\lambda)$ a factor $\exp\left\{\overline{C}\int^\lambda d\lambda'/[\mu(\lambda')-p]\right\}$, where $\overline{C}$ remains to be determined, with the intention of showing that this factor contains the whole singularity of w in the asymptotic limit. Thus we set

$$w(v,\lambda)=\chi(v,\lambda)\,\exp\left\{\overline{C}\int^\lambda d\lambda'/[\mu(\lambda')-p]\right\} \tag{29}$$

$$y(p,u_x,\lambda)=[\mu(\lambda)-p]^{-1}\chi(v,\lambda)\,\exp\left\{\overline{C}\int^\lambda d\lambda'/[\mu(\lambda')-p]\right\}. \tag{29'}$$

Equation (28) becomes

$$(1+\tfrac{1}{2}v^2)\,\chi(v,\lambda)=(2\pi p)^{-1}\int d\boldsymbol{v}' k(\lambda-\Lambda,\lambda)\,\exp\left\{-\overline{C}\int_{\lambda-\Lambda}^\lambda d\lambda'/[\mu(\lambda')-p]\right\}\chi(v',\lambda), \tag{30}$$

and we shall show that in the asymptotic limit Λ vanishes, so that $k(\lambda-\Lambda,\lambda)$ equals C, and the exponential becomes independent of λ. As a result χ becomes, in this limit, a nonsingular function of v only, so that the exponential in (29) does indeed represent the singular behavior of w. The values of $\overline{C}$ will be fixed by the condition that $\chi\,(v)$ converge for large v.

To carry out this program, we begin by studying the equation (27) which determines Λ. If we substitute $\boldsymbol{u}$ and $\boldsymbol{u}'$ from (24), (27) becomes

$$\Lambda=1-\left[1-\frac{1}{2}\frac{\mu(\lambda)-p}{p}v^2\right]\left[1-\frac{1}{2}\frac{\mu(\lambda-\Lambda)-p}{p}v'^2\right]$$
$$-\left\{\frac{1}{2}\frac{\mu(\lambda)-p}{p}\left[1-\frac{1}{4}\frac{\mu(\lambda)-p}{p}v^2\right]\frac{1}{2}\frac{\mu(\lambda-\Lambda)-p}{p}\left[1-\frac{1}{4}\frac{\mu(\lambda-\Lambda)-p}{p}v'^2\right]\right\}^{1/2}2\,\boldsymbol{v}\cdot\boldsymbol{v}'. \tag{31}$$

Terms of higher order in $[\mu(\lambda)-p]/p$ will be disregarded henceforth in the asymptotic limit. Such terms should be treated by a power expansion in case one intended to proceed to higher

approximations. This procedure has the same effect upon (31) as the "small angle approximation" indicated in (23). Equation (31) reduces then to

$$\Lambda=\frac{1}{2}\frac{\mu(\lambda)-p}{p}\left\{\left[v^2+\frac{\mu(\lambda-\Lambda)-p}{\mu(\lambda)-p}\,v'^2\right]-\left[\frac{\mu(\lambda-\Lambda)-p}{\mu(\lambda)-p}\right]^{1/2}2\,\boldsymbol{v}\cdot\boldsymbol{v}'\right\}. \tag{32}$$

Since this equation indicates that Λ tends to vanish in proportion to $[\mu(\lambda)-p]/p$, in the asymptotic limit, we replace Λ with the variable

$$\xi=\Lambda p/[\mu(\lambda)-p], \tag{33}$$

which we surmise to remain finite in the asymptotic limit. The dependence of $\mu(\lambda-\Lambda)$ on Λ will also be indicated through a parameter which tends to a finite limit, namely

$$\eta=[\mu(\lambda)-\mu(\lambda-\Lambda)]/p\Lambda=[\mu(\lambda)-\mu(\lambda-\xi[\mu(\lambda)-p]/p)]/\xi[\mu(\lambda)-p] \tag{34}$$

$$\mu(\lambda-\Lambda)=\mu(\lambda)-\eta p\Lambda. \tag{35}$$

With these substitutions, (32) reduces to the quadratic form

$$(2+v'^2\eta)^2\xi^2-2[2(v^2+v'^2)+(v'^4+v^2v'^2-2\boldsymbol{v}\cdot\boldsymbol{v}'^2)\eta]\xi+[(v^2+v'^2)^2-4\boldsymbol{v}\cdot\boldsymbol{v}'^2]=0. \tag{36}$$

This equation depends on ξ not only explicitly but also through η. However, if the right side of (34) is expanded into powers of $[\mu(\lambda)-p]/p$ and only the first term is retained, one finds that

$$\eta=(d\mu/d\lambda)/p=\dot{\mu}(\lambda)/p \tag{37}$$

independently of ξ. Therefore, ξ is given by (36) as an algebraic expression $\xi(\boldsymbol{v}\cdot\boldsymbol{v}',\dot{\mu}/p)$ which is finite and independent of $[\mu(\lambda)-p]/p$ in the asymptotic limit. Owing to (33), Λ vanishes then in the asymptotic limit, as we had surmised.

Therefore, in this limit, $k(\lambda-\Lambda,\lambda)=k(\lambda,\lambda)=C$, the exponent of (30) becomes

$$\overline{C}\int_{\lambda-\Lambda}^{\lambda}d\lambda'/[\mu(\lambda')-p]=\overline{C}\int_{\lambda-\xi[\mu(\lambda)-p]/p}^{\lambda}d\lambda'/[\mu(\lambda')-p]=(\overline{C}/\dot{\mu})\ln[1-\xi\dot{\mu}/p]. \tag{38}$$

and the equation (30) reduces to

$$(1+\tfrac{1}{2}v^2)\chi(v,\lambda)=(C/2\pi p)\int d\boldsymbol{v}'\,[1-\xi(\boldsymbol{v},\boldsymbol{v}',\dot{\mu}/p)\,\dot{\mu}/p]^{\overline{C}/\dot{\mu}}\chi(v',\lambda). \tag{39}$$

The kernel of this integral equation depends on λ through $\dot{\mu}$. Within the narrow critical range of photon energies, $\lambda\sim\lambda_s$, in which we seek an analytical solution, μ (λ) can be expressed as a power series

$$\dot{\mu}(\lambda)=\dot{\mu}_s+\ddot{\mu}_s(\lambda-\lambda_s)+1/2\dddot{\mu}_s(\lambda-\lambda_s)^2+\ldots \tag{40}$$

Accordingly, one may seek the solution of (39) by expanding both the kernel $[1-\xi(\boldsymbol{v},\boldsymbol{v}',\dot{\mu}/p)\,\dot{\mu}/p]\overline{C}/\dot{\mu}$ and the unknown function $\chi(v,\lambda)$ into powers of $(\lambda-\lambda_s)$. Since the critical range around λ_s becomes infinitely narrow in the asymptotic limit, the singularity of $y(p,u_x,\lambda)$ (at $p=\mu_s,u_x=1$) depends only on the zero-order term of the expansion into $(\lambda-\lambda_s)^n$. Therefore, for the purpose of studying this singularity, we may set

$$\chi(v,\lambda)\sim\chi(v,\lambda_s)=\chi_0(v), \tag{41}$$

where $\chi_0(v)$ fulfils the eq (39) at $\lambda=\lambda_s$, and with $p=\mu_s$, that is,

$$(1+\tfrac{1}{2}v^2)\chi_0(v)=(C/2\pi\mu_s)\int d\boldsymbol{v}'[1-\xi(\boldsymbol{v},\boldsymbol{v}',\dot{\mu}_s/\mu_s)\,\dot{\mu}_s/\mu_s]^{C/\dot{\mu}_s}\chi_0(v'). \tag{42}$$

In this manner we have reduced the problem to the solution of an equation in the single variable v, that is, we have achieved the same separation of the energy and direction variables (λ and v) as was achieved by Wick. The only difference lies in having achieved the separation by a limiting procedure rather than by initial assumptions regarding the variation of $\mu(\lambda)$ and the constancy of $k(\lambda,\lambda)$. Notice that (42) holds whether λ_s coincides with the primary wavelength λ_0 (that is, for $\lambda_0>\lambda_m$), with the longest wavelength λ (that is for $\lambda_0<\lambda<\lambda_m$) or with the wavelength of minimum absorption λ_m(that is for $\lambda_0<\lambda_m<\lambda$). In the last event $\mu_s=\dot{\mu}_m=0$ and, according to (36) and (37), the kernel of (42) reduces to

$$\{[1-\xi(\boldsymbol{v},\boldsymbol{v}',\dot{\mu}_s/\mu_s)\dot{\mu}_s/\mu_s]^{C/\dot{\mu}_s}\}_{\dot{\mu}_s=0}=\exp[-(\overline{C}/\mu_m)\xi(\boldsymbol{v},\boldsymbol{v}',0)]=\exp\{-\tfrac{1}{2}(\overline{C}/\mu_m)|\boldsymbol{v}-\boldsymbol{v}'|^2\} \quad (43)$$

Equation (42) is equivalent to the Wick eigenvalue equations and has finite solutions $\chi_0(v)$ only for special values of $\overline{C}$. As in the standard eigenvalue problems with a single independent variable, the successive eigenfunctions $\chi_0^{(0)}(v),\chi_0^{(1)}(v),\ \ldots\ \chi_0^{(n)}(v)\ \ldots$ have $0,1\ \ldots\ n\ \ldots$ nodes. The corresponding eigenvalues $\overline{C}^{(0)},\ \overline{C}^{(1)},\ \ldots\ \overline{C}^{(n)}\ \ldots$ depend monotonically on n. The eigenvalue $\overline{C}^{(0)}$ is the largest one, algebraically. Each of the eigenvalues $\overline{C}^{(n)}$ characterizes a type of singularity of $y(p,u_x,\lambda)$. As mentioned before, these singularities coincide with those of the straight-ahead solutions (14) in section 5 except for the replacement of the constant C with $\overline{C}$. The solution of the inhomogenous equation (8) or (26) will be constructed, in the next section, as a superposition of components, each of which is a solution of the homogeneous equation, with different values of $\overline{C}$. We anticipate here that the component with the largest value of $\overline{C}$ in (29′) is clearly the one with the sharpest singularity and therefore the one which predominates and which alone matters in the asymptotic limit.

The equivalence of (42) with the Wick equations is immediately apparent when $\lambda_s=\lambda_m$, $\mu_s=\mu_m$, $\dot{\mu}_s=0$, that is, when the kernel of (42) takes the form (43), so that

$$\left[1+\frac{1}{2}v^2\right]\chi_0(v)=[C/2\pi\mu_m]\int d\boldsymbol{v}'\exp\left[-\frac{1}{2}(\overline{C}/\mu_m)|\boldsymbol{v}-\boldsymbol{v}'|^2\right]\chi(v'). \quad (44)$$

This equation coincides with (W53) [1], as shown by substituting

$$\boldsymbol{v}=\frac{1}{2}(M/k)^{1/2}\boldsymbol{s},\quad \overline{C}/\mu_m=2k/M,\quad C/\mu_m=(M+1)^2/2M^2. \quad (45)$$

When $\dot{\mu}_s\neq 0$ no better procedure is seen, to show the eigenvalence with the Wick equations, than to backtrack from (42) to an equivalent homogeneous equation in the variables λ and u_x and to handle this problem by Laplace and Fourier transforms in the manner of Wick. One may then identify $\chi_0(v)$ with a transform of solutions of Wick equations according to the formulae

$$\begin{aligned}\chi_0(v)&=(\dot{\mu}_s/2\pi i\mu_s)\int_{-i\infty}^{i\infty}dt\ \exp t\, t^{1-\overline{C}/\dot{\mu}_s}f([2t\dot{\mu}_s/\mu_s]^{1/2}v)\\&=(\dot{\mu}_s/8\pi^2 i)\int_{-i\infty}^{i\infty}dt\int d\boldsymbol{q}\ \exp\,(t-it^{1/2}\boldsymbol{q}\cdot\boldsymbol{v})\ t^{1-\overline{C}/\dot{\mu}_s}\phi([\mu_s/2\dot{\mu}_s]^{1/2}\boldsymbol{q})\\&=(\dot{\mu}_s/8\pi^2 i)\int_{-i\infty}^{i\infty}dt\int d\boldsymbol{q}\ \exp\,(t-it^{1/2}\boldsymbol{q}\cdot\boldsymbol{v}+q^2/u)t^{1-\overline{C}/\dot{\mu}_s}U([\mu_s/2\dot{\mu}_s]^{1/2}\boldsymbol{q}).\end{aligned} \quad (46)$$

The functions f, Φ and U obey the equations

$$\left[\overline{C}-\dot{\mu}_s-\frac{1}{2}\dot{\mu}_s u(d/du)+\frac{1}{4}\mu_s u^2\right]f(u)=(C/4\pi)\int d\boldsymbol{u}'\exp\left(\frac{1}{4}|\boldsymbol{u}-\boldsymbol{u}'|^2\right)f(u'), \quad (47)$$

$$\left\{\frac{1}{4}\mu_s[(d/d\sigma)^2+\sigma^{-1}(d/d\sigma)]-\frac{1}{2}\dot{\mu}_s\sigma(d/d\sigma)+C\exp(-\sigma^2)\right\}\phi(\sigma)=\overline{C}\phi(\sigma), \quad (48)$$

$$\left\{\frac{1}{4}\mu_s[(d/d\sigma)^2+\sigma^{-1}(d/d\sigma)]+\frac{1}{2}\dot{\mu}_s+C\exp(-\sigma^2)-\frac{1}{4}\dot{\mu}_s\sigma^2/\mu_s\right\}U(\sigma)=\overline{C}U(\sigma). \quad (49)$$

All of these equations obtain when $\mu_s=0$ as well as when $\mu_s\neq 0$, and for $\mu_s<0$ (that is, for $\lambda_0<\lambda_s<\lambda_m$) as well as for $\mu_s>0$. In particular, (47) coincides with (44), for $\mu_s=0$, if $\boldsymbol{u}$ is replaced with $(2\overline{C}/\mu_m)^{1/2}\boldsymbol{v}$.

The self-adjoint differential equation (49) has the form of the Schroedinger equation for the motion of a particle oscillating radially in a cylindrically symmetrical potential. It is identical with (W105) [1] as shown by performing the substitutions

$$C/\mu_s=(M+1)^2/2M^2, \quad \dot{\mu}_s/\mu_0=2\gamma/M, \quad \overline{C}/\dot{\mu}_s=2-\rho. \tag{50}$$

It is also identical with eq (V4) [4] as shown by replacing σ^2 with $\sigma^2/2$ and $\overline{C}$ with $-Q/\dot{\mu}_s$.

Wick has estimated the largest eigenvalue of his Schroedinger-type equations by a variational method. When $\dot{\mu}_s=0$ he finds

$$\overline{C}\sim(C^{1/2}-\tfrac{1}{2}\mu_m{}^{1/2})^2=C[1-\tfrac{1}{2}(\mu_m/C)^{1/2}]^2. \tag{51}$$

This eigenvalue reduces to C as μ_m/C approaches zero. The ratio C/μ_m represents the differential cross section for Compton scattering, for $\lambda'=\lambda$, expressed in units of the minimum value of the total cross section. When $\dot{\mu}_s\neq 0$ the largest approximate eigenvalue is

$$\overline{C}\sim\mu_s[(C/\mu_s)r(r+1)^{-1}+\tfrac{1}{2}\dot{\mu}_s/\mu_s-\tfrac{1}{4}(\dot{\mu}_s/\mu_s)^2r^{-1}], \tag{52}$$

where the parameter r indicates the solution of the algebraic equation

$$4(C/\mu_s)(r+1)^{-2}+(\dot{\mu}_s/\mu_s)^2r^{-2}=1. \tag{53}$$

When the logarithmic derivative $|\dot{\mu}_s/\mu_s|$ is large, one may solve (49) by a perturbation method starting from the solutions of the quantum mechanical harmonic oscillator problem and treating $\epsilon=\mu_s/\dot{\mu}_s$ as a small quantity. The result, given in (V6) [4], is

$$\overline{C}=C-\tfrac{1}{2}\dot{\mu}(\alpha-1)+C\epsilon^2/\alpha(\alpha+\epsilon)+C^2\epsilon^4(2\alpha+\epsilon)^2/\dot{\mu}_s\alpha^3(\alpha+\epsilon)^4+\ \ldots, \tag{54}$$

with

$$\alpha=[1+4(C/\dot{\mu}_s)\epsilon]^2. \tag{55}$$

In practice $\mu_s/\dot{\mu}_s$ is seldom very small, and the range of application of the simple perturbation method is limited. The investigation of eigenvalues proceeds more effectively by the simple variational method of Wick or by the methods that were developed by Spencer [6] for the numerical solution of the semiasymptotic problem. Appendix C contains a description of these latter methods and tables of eigenvalues.

8. Effect of Obliquity of the Primary Radiation

We resume here the discussion of section 2.6 regarding the influence of the source direction on the penetration law.

In the last section, we have studied the singularity of special solutions of the transform equation at $p=\mu_s$. These special solutions obey a homogeneous transform equation shorn of any source term. It was understood that the solution $y(p,u_z,\lambda)$ of the complete, inhomogeneous, transport equation (8), in the critical range $\lambda\sim\lambda_s$ and in the asymptotic limit, should be constructed as a superposition of special solutions (29′)

$$y(p,u_z,\lambda)=\Sigma_n a_n[\mu(\lambda)-p]^{-1}\chi^{(n)}(v,\lambda)\ \exp\left\{\overline{C}^{(n)}\int^{\lambda}d\lambda'/[\mu(\lambda')-p]\right\}$$

$$\sim\Sigma_n a_n[\mu(\lambda)-p]^{-1}\chi_0^{(n)}(v)\ \exp\left\{\overline{C}^{(n)}\int^{\lambda}d\lambda'/[\mu(\lambda')-p]\right\}. \tag{56}$$

here $\chi_0^{(n)}(v)$ and $\overline{C}^{(n)}$ represent, respectively, the n-th eigenfunction and eigenvalue of (42). The function $\chi^{(n)}(v,\lambda)$ in the middle part of (56) represents the complete expansion $\chi^{(n)}=\Sigma_r \chi_r^{(n)}(v)(\lambda-\lambda_s)^r$ which begins with $\chi_0^{(n)}$ and can be carried to higher order of approximation if necessary.

As p approaches μ_s, the factors $\exp\left\{\overline{C}^{(n)}\int^{\lambda} d\lambda'/[\mu(\lambda')-p]\right\}$ become infinitely large, provided $\overline{C}^{(n)}>0$. Wick pointed out that only one of the eigenvalues $\overline{C}^{(n)}$, namely $\overline{C}^{(0)}$, may happen to be positive. At any rate the term $n=0$ of the sum (56), with the algebraically largest eigenvalue $\overline{C}^{(0)}$, will increase fastest as p approaches μ_s and will predominate over all others in the asymptotic limit. Therefore, the singularity of $y(p,u_z,\lambda)$ depends primarily on the behavior of $\exp\left\{\overline{C}^{(0)}\int^{\lambda} d\lambda'/[\mu(\lambda')-p]\right\}$, as anticipated in section 7. The behavior of this factor is described by (14) in section 5.

In addition, one must consider the factor $[\mu(\lambda)-p]^{-1}$, if $\mu(\lambda)\sim\mu_s$ and especially the dependence, if any, of the coefficient a_0 on p. The coefficients a_n of the superposition (56) are determined by the inhomogenity of the transform eqn (8), that is by the characteristics of the radiation source. Therefore, these characteristics may influence the singularity of $y(p,u_z,\lambda)$, and hence the penetration law at great depths, through the dependence of a_0 on p.

It has been pointed out in section 2.6 that the obliquity of the primary radiation has much less influence on the penetration for high source energies, $\lambda_0<<\lambda_m$ than for $\lambda_0>\lambda_m$. This important difference shows up clearly in the process of determining the coefficients a_n of the expansion (56).

If the source energy is considerably larger than the energy of maximum penetration, one will probably have to resort to numerical integration of the transform eq (8) from the source wavelength λ_0 at least up to some wavelength λ_f somewhat lower than λ_m. If $\lambda_0<<\lambda_m$, and one is interested in the distribution of photons of energy higher than the energy of maximum penetration, then λ_s equals the wavelength of these photons and one must choose $\lambda_f<\lambda_s$. Whether $\lambda_s<\lambda_m$ or $\lambda_s=\lambda_m$, we define λ_f so that $\lambda_0<\lambda_f\lesssim\lambda_s\leq\lambda_m$. A superposition of analytical solutions valid in the critical range $\lambda\sim\lambda_s$ should then be fitted to the numerical solution at λ_f. Under asymptotic conditions, $(\mu_s-p)/p<<1$, the fitting-wavelength λ_f can be so chosen that $\mu(\lambda_f)-\mu_s>>\mu_s-p$, that is so that $\mu(\lambda)-p$ can be safely replaced with $\mu(\lambda)-\mu_s$ for $\lambda\leq\lambda_f$. When this is so, the photon distribution at λ_f varies no longer as p approaches μ_s still further. Similarly, the analytical solutions $\chi^{(n)}(v,\lambda)\exp\left\{\overline{C}^{(n)}\int^{\lambda} d\lambda'/[\mu(\lambda')-p]\right\}$, extended from $\lambda\sim\lambda_s$ to λ_f, no longer depend on p in the proximity of λ_f, where p may be effectively replaced with μ_s.

Under these conditions, the fitting of the superposition of analytical solutions to the actual photon distribution at λ_f, that is, the determination of the coefficients a_n of (56), gives a result independent of p. Any change of obliquity of the source radiation causes a change of the directional distribution of the photons at λ_f and, therefore, a change of the coefficients a_n. The photon distribution through the critical range will vary with p in a manner which depends on the intensity ratio of the component solutions $a_n\chi_n(v,\lambda)\exp\{\ldots\}$ of (56) and, therefore, on the obliquity of the source radiation.

However, the intensity of the lower energy radiation depends only on the $n=0$ term of (56), once p is sufficiently near to μ_m, and therefore it will vary with p only through $\exp\left\{\overline{C}^{(0)}\int^{\lambda} d\lambda'/[\mu(\lambda')-p]\right\}$, independently of the ratios among the a_n's. That is, the source obliquity influences the intensity of the lower energy radiation through the same factor a_0 independently of depth of penetration, provided this depth is adequate to insure fully asymptotic conditions.

A quite different situation prevails when $\lambda_0>\lambda_m$, since the coefficients of the analytical solutions in (56) must be fitted to the directional distribution of the source radiation right at $\lambda_0=\lambda_s$, in the middle of the critical range. Here, the dependence of the a_n's on p has been worked out by Wick for an isotropic source [1], and in reference [4] for a monodirectional source.

General formulae equivalent to a determination of the a_n's will be given here below, but they are of very limited usefulness because of their complication and, especially, because they imply a knowledge of the directional eigenfunctions $\chi_0^{(n)}(v)$. A practical solution of the effect of source obliquity under these conditions will probably require much additional work.

An analytical solution for $\lambda_0 > \lambda_m$, equivalent to (56) and fitted to the directional distribution of the X-ray source, can be obtained performing a Laplace transformation of the energy variable λ, according to Wick [1]. This is a solution of the transport equation (8) schematized in the following manner:

(1) $\mu(\lambda)$ is taken as $\mu_0 + \dot{\mu}_0(\lambda - \lambda_0)$,

(2) $k(\lambda', \lambda)$ is replaced with C,

(3) $\boldsymbol{u} = (\vartheta, \varphi)$ is replaced with a "small-angle approximation" vector $\boldsymbol{s} = (s, \varphi)$, with $0 \leq s \leq \infty$, such that u_z may be replaced with $1 - \frac{1}{2}s^2$, and $\boldsymbol{u} \cdot \boldsymbol{u}'$ with $1 - \frac{1}{2}|\boldsymbol{s} - \boldsymbol{s}'|^2$. For small angles, one sets $s \sim \vartheta$. The solution of the equation is then written as

$$y(p, s, \lambda) = \frac{1}{2\pi i} \int_{-i\infty}^{i\infty} d\eta e^{\eta(\lambda - \lambda_0)} \frac{1}{4\pi^2} \int d\boldsymbol{k} e^{i\sqrt{2\alpha}\boldsymbol{k}\cdot\boldsymbol{s} + \dot{\mu}_0 k^2/2p} \times \Sigma_n U_n(k) \frac{\eta}{\mu_0 - p} \int_0^\infty dl e^{-\eta l} \left[1 + \frac{\dot{\mu}_0 l}{\mu_0 - p}\right]^{\overline{C}^{(n)}/\dot{\mu}_0 - 1} D_n\left(\eta\left[1 + \frac{\dot{\mu}_0 l}{\mu_0 - p}\right]\right). \quad (57)$$

Here U_n and $\overline{C}^{(n)}$ are the eigenfunctions and eigenvalues of (49) and

$$D_n(\alpha) = \frac{\alpha}{4\pi^2} \int d\boldsymbol{s} f\left(1 - \frac{1}{2}s^2\right) \int d\boldsymbol{k} e^{-i\sqrt{2\alpha}\boldsymbol{k}\cdot\boldsymbol{s} - \dot{\mu}_0 k^2/2p} U_n(k) \quad (58)$$

is, in essence, a coefficient of the expansion of the directional distribution of the source—indicated by $f(u_z)$ in (8)— in terms of the eigenfunctions of (47). Some simplification is attained by considering only the X-ray flux integrated over all directions, since in this case (57) yields

$$\int d\boldsymbol{s} y(p, s, \lambda) = \frac{1}{2\pi i} \int_{-i\infty}^{i\infty} d\eta e^{\eta(\lambda - \lambda_0)} \Sigma_n \frac{U_n(0)}{2(\mu_0 - p)} \cdot \int dl e^{-\eta l} \left[1 + \frac{\dot{\mu}_0 l}{\mu_0 - p}\right]^{\overline{C}^{(n)}/\dot{\mu}_0 - 1} D_n\left(\eta\left[1 + \frac{\dot{\mu}_0 l}{\mu_0 - p}\right]\right). \quad (59)$$

Much further simplification obtains for two special types of source, namely, (a) monodirectional perpendicular to the source plane, $f(1 - \frac{1}{2}s^2) = \delta(\boldsymbol{s})$, and (b) isotropic, or practically isotropic, $f(1 - \frac{1}{2}s^2) \sim \overline{f} = \text{const.}$, since (58) reduces, respectively, to

$$D_n(\alpha) = \frac{\alpha}{2\pi} \int_0^\infty k dk e^{-\dot{\mu}_0 k^2/2p} U_n(k), \quad (60a)$$

and

$$D_n(\alpha) = \tfrac{1}{2} U_n(0) \overline{f}. \quad (60b)$$

Whether D_n is constant or proportional to its argument, the two integrals in (59) may be treated as a Laplace transform followed by its inverse, so that (59) reduces to

$$\int d\boldsymbol{s} y(p, s, \lambda) = \Sigma_n \frac{U_n(0)}{4\pi} \frac{d}{d\lambda} \frac{1}{\mu_0 - p} \left[1 + \frac{\dot{\mu}_0(\lambda - \lambda_0)}{\mu_0 - p}\right]^{\overline{C}^{(n)}/\dot{\mu}_0 - 1} \int_0^\infty k dk e^{-\dot{\mu}_0 k^2/2p} U_n(k), \quad (61a)$$

and

$$\int d\boldsymbol{s} y(p, s, \lambda) = \Sigma_n \frac{1}{4} [U_n(0)]^2 \overline{f} \frac{1}{\mu_0 - p} \left[1 + \frac{\dot{\mu}_0(\lambda - \lambda_0)}{\mu_0 - p}\right]^{\overline{C}^{(n)}/\dot{\mu}_0 - 1}, \quad (61b)$$

respectively, that is, to algebraic functions of $\mu_0 - p$. (The p in the exponential of (61a) may be safely replaced with μ_0).

For other types of directional distribution, the dependence of (57) or (59) on $\mu_0 - p$ is quite complicated and even difficult to survey qualitatively, as had been anticipated.

9. Inversion of the Laplace Transform

Following the discussion of the singularity of $y(p,u_x,\lambda)$ at $p=\mu_s$ in sections 5 and 7, we shall now translate each type of singularity of the Laplace transform into a corresponding distribution-in-depth of the X-rays for large values of the depth x within the medium. The translation is done by means of the inverse transform formula (7)

$$Y(x,u_x,\lambda)=\frac{1}{2\pi i}\int_{-i\infty}^{i\infty}\exp(-px)\,y(p,u_x,\lambda)dp=\exp(-\mu_s x)\frac{1}{2\pi i}\int_{-i\infty}^{i\infty}\exp[(\mu_s-p)x]\,y(p,u_x,\lambda)dp. \quad (62)$$

Having split off the factor $\exp(-\mu_s x)$ in the last expression, the remaining integral represents the buildup factor $B(x,u_x,\lambda)$ (to within a constant factor equal to the source intensity). Henceforth, we shall be interested in the dependence of B on x for any given obliquity u_x and wavelength λ and, therefore, we shall omit explicit reference to u_x and λ. Similarly, it will be convenient to indicate $y(p,u_x,\lambda)$ simply as $y(\mu_s-p)$, so that (62) takes the form

$$B(x)=\frac{1}{2\pi i}\int_{-i\infty}^{i\infty}dp\,\exp[(\mu_s-p)x]y(\mu_s-p). \quad (63)$$

The preceding sections have called attention to two types of singularities of $y(\mu_s-p)$, namely: (a) an inverse power law, which we indicate as

$$y(\mu_s-p)\propto(\mu_s-p)^{-K-1}, \quad (64a)$$

and (b) an exponential function of the inverse square root, which we indicate as

$$y(\mu_s-p)\propto\exp[D\mu_s/(\mu_s-p)]^{1/2}. \quad (64b)$$

Equation (64a) describes the singularity when $\lambda_0>\lambda_m$ and the directional distribution of the source is either perpendicular to the source plane or effectively isotropic, as shown, respectively, by (61a) and (61b). In addition, the same type of singularity arises for $\lambda_0<\lambda_m$ in the calculation of the buildup factor for $\lambda<\lambda_m$, that is, when $\lambda_0<\lambda_s<\lambda_m$, in which case the straight-ahead result (14c) applies, except for the replacement of C with $\overline{C}^{(0)}$. Henceforth $\overline{C}^{(0)}$ will be indicated briefly as $\overline{C}$. The value of K in (64a) is given by

$$K=\overline{C}/|\dot{\mu}_s| \quad (65)$$

for $\lambda_s<\lambda_m$, according to (14c), and for $\lambda_s>\lambda_m$ with an isotropic source, according to (61b), whereas

$$K=\overline{C}/\dot{\mu}_s+1 \quad (66)$$

for $\lambda_s>\lambda_m$ with a monodirectional source, owing to the derivative in (61a). Equation (64b) describes the singularity when $\lambda_s=\lambda_m$ and $\lambda>\lambda_m$, which implies $\lambda_0<\lambda_m$, in which case (14b) applies, except for the replacement of C with $\overline{C}$, and

$$D=2\pi^2\overline{C}^2/\mu_m(d^2\mu/d\lambda^2)_m. \quad (67)$$

It may be added that the build-up of the radiation of maximum penetration $\lambda=\lambda_m$, for which $\lambda_s=\lambda_m$ also, involves an integration of the arctangent type of integral in (13b) over a range of $\pi/2$ of the arctangent, instead of π. Moreover, in this case, the factor $[\mu(\lambda)-p]^{-1}$ in (14b) represents $(\mu_s-p)^{-1}$. As a result, (64b) must be replaced with

$$y(\mu_s-p)\propto(\mu_s-p)^{-1}\exp[F\mu_s/(\mu_s-p)]^{1/2}, \quad (64c)$$

where

$$F=\pi^2\overline{C}^2/2\mu_m(d^2\mu/d\lambda^2)_m=D/4. \quad (68)$$

Notice that both K and D have been defined as numerical coefficients whose value has to be calculated for each medium and for the appropriate wavelength but is always of the order of 1. To emphasize the dimensional structure of K and D, we rewrite (65) and (67) in the following manner:

$$K=\frac{\overline{C}}{C}\,k(\lambda,\lambda)\left|\left(\frac{d\lambda}{d\mu}\right)_s\right| \tag{65'}$$

$$D=2\pi^2\left(\frac{\overline{C}}{C}\right)^2\left[\frac{k(\lambda,\lambda)}{\mu_m}\right]^2\Big/\left(\frac{d^2\log\mu}{d\lambda^2}\right)_m. \tag{67'}$$

The power-law singularity (64a), entered into the integral (63) yields the build-up factor proportional to x^K, which was anticipated in (2). This result can be easily derived by replacing $(\mu_s-p)s$ with $-t$ in the integral (63):*

$$B(x)\propto\frac{1}{2\pi i}\int_{-i\infty}^{i\infty}dp\,\exp\left[(\mu_s-p)x\right](\mu_s-p)^{-K-1}=x^K\,\frac{1}{2\pi i}\int_{-i\infty}^{i\infty}dt\,\exp\,(-t)(-t)^{-K-1}=\frac{x^K}{\Gamma(K+1)} \tag{69}$$

(See appendix C, tables 1, 2 for values of K, $\dot{\mu}_s/\mu_s$, C/μ_s.)

If desirable, one can also carry out the build-up factor integration by entering into (63) not merely the singularity of y as given by (64a), but the expression of $\int ds\,y(p,s,\lambda)$ as given by (61a) or (61b). We may write

$$B(x)\propto\frac{1}{2\pi i}\int_{-i\infty}^{i\infty}dp\,\exp\left[(\mu_0-p)x\right](\mu_0-p)^{-1}\left[1+\frac{\dot{\mu}_0(\lambda-\lambda_0)}{\mu_0-p}\right]^K, \tag{70}$$

and proceed, for example, by expanding the binomial

$$\left[1+\frac{\dot{\mu}_0(\lambda-\lambda_0)}{\mu_0-p}\right]^K=\sum_\nu\frac{\Gamma(-K+\nu)}{\Gamma(-K)\nu!}\left[-\frac{\dot{\mu}_0(\lambda-\lambda_0)}{\mu_0-p}\right]^\nu, \tag{71}$$

and integrating term by term, which yields

$$B(x)\propto\sum_\nu\frac{\Gamma(-K+\nu)}{\Gamma(-K)\nu!}\,[-\dot{\mu}_0(\lambda-\lambda_0)x]^\nu={}_1F_1(-K,1,-\dot{\mu}_0[\lambda-\lambda_0]x)=L_{-K}(-\dot{\mu}_0[\lambda-\lambda_0]x). \tag{72}$$

Here ${}_1F_1$ indicates, as usual, the confluent hypergeometric function whose power expansion is represented by the Σ_ν, and L_{-K} indicates the Laguerre function, to which the ${}_1F_1$ reduces when its second parameter equals 1. The binomial expansion (71) is actually unnecessary since (70) is directly recognizable as an integral representation of ${}_1F_1$ or L_{-K}. Equation (72) was derived from a schematized treatment of the straight-ahead problem in (I4) [2].

The singularity (14b) for $\lambda_s=\lambda_m$, entered into the integral (63), yields a build-up factor represented by a transcendental function of unusual type, namely

$$\begin{aligned}B(x)\propto&\frac{1}{2\pi i}\int_{-i\infty}^{i\infty}dp\,\exp\,\{(\mu_m-p)x+[D\mu_m/(\mu_m-p)]^{1/2}\}\\&=D\mu_m(D\mu_m x)^{-2/3}\,\frac{1}{2\pi i}\int_A dt\,\exp\,\{(t+t^{-1/2})(D\mu_m x)^{1/3}\}=D\mu_m(D\mu_m x)^{-2/3}G([D\mu_m x]^{1/3}).\end{aligned} \tag{73}$$

Here $t=(\mu_m-p)\,(D\mu_m)^{-2/3}x^{1/3}$, the contour A loops around the origin in the positive direction and

$$G(z)=\frac{1}{2\pi i}\int_A dt\,\exp\,[(t+t^{-1/2})z]. \tag{74}$$

* The expression of the integral as a Γ-function is found, for example, in reference [20], last formula on p. 245.

For large values of z, the function G can be evaluated by steepest descent method in the proximity of the saddle point, which lies at $t=2^{-2/3}$. The result is

$$G(z)\sim(2\pi)^{-1/2}(2^{2/3}3z)^{-1/2}\exp\,(2^{-2/3}3z). \tag{75}$$

This formula, entered into (73), yields

$$B(x)\propto(D\mu_m)(D\mu_m x)^{-5/6}2^{-5/6}(3\pi)^{-1/2}\exp\,[2^{-2/3}3(D\mu_m x)^{1/3}]. \tag{76}$$

This build-up factor is proportional to $x^{-5/6}\exp\,[H(\mu_m x)^{1/3}]$, as anticipated in (3), with

$$H=2^{-2/3}3D^{1/3}=3(\pi^2\overline{C}^2/2\mu_m\ddot{\mu}_m)^{1/3}. \tag{77}$$

This result was derived in (II 13c) [3] for the straight-ahead approximation, that is with C in the place of $\overline{C}$. (See appendix C, table 3 for values of μ_m, H, D, and $\overline{C}$).

The case $\lambda=\lambda_s=\lambda_m$ with the singularity (64c), may be treated by taking the second derivative of $B(x)$ with repsect to $D^{1/2}$, since this operation generates (64c) from (64a), and then replacing D with the appropriate value (68) of F, namely $D/4$, and H with $H/2^{2/3}=0.63\ H$.

The function $G(z)$ has been tabulated throughout the range $z>0$ by carrying out the integration (74) numerically along the steepest descent path $\mathrm{Im}(t+t^{-1/2})=0$. However no application of this tabulation has been required because Spencer [6] found it convenient to evaluate integrals of the type

$$\frac{1}{2\pi i}\int dp(\mu_0-p)^{\alpha}\exp\{(\mu_m-p)x+[D\mu_m/(\mu_m-p)]^{1/2}\} \tag{78}$$

by expansion into powers of $[D\mu_m/(\mu_m-p)]^{1/2}$ followed by term-by-term integration in the manner of (70) and (72). The method proved practical because the convergence of the expansion was moderately rapid despite the large value of the argument. (The number of terms in the expansion corresponds to the multiplicity of scattering [6]).

I thank L. V. Spencer for many helpful discussions and for contributing the appendix C.

10. References

[1] G. C. Wick, Phys. Rev. **75,** 738 (1949) referred to as W. See also, M. Verde and G. C. Wick, Phys. Rev. **71,** 852 (1947), R. E. Marshak, Rev. Mod. Phys. **19,** 201 (1947).
[2] H. A. Bethe, U. Fano, and P. R. Karr, Phys. Rev. **76,** 538 (1949), referred to as I.
[3] U. Fano, Phys. Rev. **76,** 739 (1949), referred to as II.
[4] U. Fano, H. Hurwitz Jr. and L. V. Spencer, Phys. Rev. **77,** 425 (1950), referred to as V.
[5] S. Chandrasekhar, Radiative transfer (Oxford University Press, Oxford, England, 1950).
[6] L. V. Spencer, Phys. Rev. **88,** 793 (1952).
[7] J. O. Hirschfelder, J. L. Magee, and M. H. Hull, Phys. Rev., **73,** 853 (1948); J. O. Hirschfelder and E. N. Adams, Phys. Rev. **73,** 863 (1948); P. Maignan, Compt. rend. **230,** 2018 (1950).
[8] G. H. Peebles and M. S. Plesset, Phys. Rev. **81,** 430 (1951).
[9] L. Cave, J. Corner and R. H. A. Liston, Proc. Roy. Soc. [A] **204,** 223 (1950); J. Corner and R. H. A. Liston, Proc. Roy. Soc. [A] **204,** 323 (1950); J. Corner, F. A. G. Day and R. E. Weir, Proc. Roy. Soc. [A] **204,** 329 (1950).
[10] L. L. Foldy, Phys. Rev. **81,** 395 (1951); L. L. Foldy and R. K. Osborn, Phys. Rev. **81,** 400 (1951).
[11] W. R. Faust and M. H. Johnson, Phys. Rev. **75,** 467 (1949); W. R. Faust, Phys. Rev. **77,** 227 (1950).
[12] H. Kahn, Nucleonics **6,** 60 (1950).
[13] L. V. Spencer and U. Fano, J. Research, NBS **46,** 446 (1951). RP2213.
[14] L. V. Spencer, Phys. Rev. **90,** 146 (1953).
[15] G. R. White, Phys. Rev. **80,** 154 (1950).
[16] E. Hayward, Phys. Rev. **86,** 493 (1952).
[17] L. V. Spencer and F. A. Stinson, Phys. Rev. **85,** 662 (1952).
[18] U. Fano, Phys. Rev., in press.
[19] I. Waller, Arkiv Mat. **34A,** No. 3, 4, 5.
[20] E. T. Whittaker and G. N. Watson, Modern Analysis, Cambridge and New York (1946).
[21] R. C. O'Rourke, Phys. Rev. **85,** 881 (1952).

11. Appendix A. Connection Between the X-Ray Distributions From a Plane Isotropic and From a Point Isotropic Source

The X-ray distribution from a plane isotropic source is represented by the solution of eq (5), with $f(u_z)=1$. The equation for a point isotropic monoenergetic source is a particular case of (4) in which one takes the source term $S(\boldsymbol{r},\boldsymbol{u},\lambda)=\delta(\boldsymbol{r})\delta(\lambda-\lambda_0)$. The solution of this equation will be indicated as $F(r,u_r,\lambda)$, where $u_r=\boldsymbol{u}\cdot\boldsymbol{r}/r$ is the radial component of $\boldsymbol{u}$.

Following up the discussion of plane-symmetrical geometries in section 1, we notice that the plane isotropic source $\delta(x)\delta(\lambda-\lambda_0)$ may be regarded as a plane integral over a distribution of point isotropic sources located at $\boldsymbol{r}_0=(0,y_0,z_0)$

$$\delta(x)\delta(\lambda-\lambda_0)=\int_{-\infty}^{\infty}\int_{-\infty}^{\infty}dy_0dz_0\delta(\boldsymbol{r}-\boldsymbol{r}_0)\delta(\lambda-\lambda_0). \tag{A1}$$

Owing to the linearity of the transport eq (4), the distribution $Y(x,u_x,\lambda)$ will be similarly expressed as an integral over the distribution $F(r,u_r,\lambda)$. Consider an isotropic point source at $(0,y_0,z_0)$ and a point P at $(x,0,0)$. The distance from the source to P is $r=[x^2+y_0^2+z_0^2]^{1/2}$ and u_r is equal to $(u_x x-u_y y_0-u_z z_0)/[x^2+y_0^2+z_0^2]^{1/2}$. We have

$$Y(x,u_x,\lambda)=\int_{-\infty}^{\infty}\int_{-\infty}^{\infty}dy_0dz_0F\left([x^2+y_0^2+z_0^2]^{1/2},\frac{u_x x-u_y y_0-u_z z_0}{[x^2+y_0^2+z_0^2]^{1/2}},\lambda\right). \tag{A2}$$

If we take cylindrical coordinates (ρ,ψ,x), with $\rho^2=y_0^2+z_0^2$ and $\psi=\arccos\,[-(u_y y_0+u_z z_0)/\rho(1-u_x^2)^{1/2}]$, (A2) becomes

$$Y(x,u_x,\lambda)=\int_0^{2\pi}d\psi\int_0^{\infty}\rho d\rho F\left([x^2+\rho^2]^{1/2},\frac{u_x x+[1-u_x^2]^{1/2}\rho\cos\psi}{[x^2+\rho^2]^{1/2}},\lambda\right). \tag{A3}$$

The distribution $F(r,u_r,\lambda)$ may be represented by the Legendre polynomial expansion

$$F(r,u_r,\lambda)=\sum_l(2l+1)(4\pi)^{-1}F_l(r,\lambda)\,P_l(u_r), \tag{A4}$$

and similarly

$$Y(x,u_x,\lambda)=\sum_l(2l+1)(4\pi)^{-1}Y_l(x,\lambda)\,P_l(u_x). \tag{A5}$$

Since the $\int_0^{2\pi}d\psi\,P_l([u_x x+(1-u_x^2)^{1/2}\rho\cos\psi]/[x^2+\rho^2]^{1/2})$ equals simply $2\pi P_l(u_x)\,P_l(x/[x^2+\rho^2])$, (A3) reduces to

$$Y_l(x,\lambda)=\int_0^{\infty}\rho d\rho F_l([x^2+\rho^2]^{1/2},\lambda)\,P_l(x/[x^2+\rho^2]^{1/2})$$
$$=\int_x^{\infty}RdR\,F_l(R,\lambda)\,P_l(x/R). \tag{A6}$$

The Legendre coefficients with $l=0$ represent the total intensity distribution at each point, irrespective of direction of propagation. Since $P_0=1$, the relationship (A6) simplifies for $l=0$ to

$$Y_0(x,\lambda)=\int_x^{\infty}RdR\,F_0(R,\lambda) \tag{A7}$$

$$F_0(x,\lambda)=x^{-1}\partial Y_0(x,\lambda)/\partial x. \tag{A8}$$

12. Appendix B. Note on the Treatment of Strongly Nonself-adjoint Systems

Consider the system of equations.

$$\sum_{m=1}^{n}a_{nm}x_m+px_{n+1}=c_n. \tag{B1}$$

In the limit $p=0$ this system has a trivially simple solution since the first equation contains the variable x_1 alone and all other equations can be solved chainwise. If p is sufficiently small, the terms px_{n+1} may be regarded as small perturbations with respect to the trival case $p=0$.

Our method of proceeding is this: If one assumes a trial value of the ratio x_2/x_1, the first equation determines the absolute value of x_1 and x_2. Thereafter the n-th equation determines the $n+1$-th variable, chainwise. Owing to the smallness of p, any error in the initial estimate of x_2/x_1 which causes a wrong estimate of $\sum_{m=1}^{n}a_{nm}x_m$, causes a much larger error in the estimate of x_{n+1}, and so on. A trial and error method with successive estimates of x_2/x_1 may thus proceed quite rapidly, because the amplification of the error in successive equations soon causes the trial solution to become grossly unrealistic, as judged by some suitable criterion.

Experimental calculations were made with the homogeneous system

$$x_n=(x_{n-3}+x_{n-2}+x_{n-1}-x_{n+1})/2, \tag{B2}$$

assuming $x_n=0$ for negative n. This system may be regarded as representing a game of chance of the parchesee type, in which case x must be positive. Successive variables are linear functions of the trial value of x_1/x_0 with alternate and rapidly increasing slope. Calculation up to $n=8$ suffices to show that the solution becomes unacceptable unless x_1/x_0 ~ 0.325.

As a physical model for the considerations presented here one may think of a chain of pendulums with asymmetrical or "coaster", couplings, such that the motion of each pendulum influences the next pendulum on its right strongly but the one on its left only weakly. If the right-to-left coupling were nil, then the motion of the whole set would be fully determined proceeding from the left to the right. Because the right-to-left coupling is weak, one can still determine the whole motion easily by approximation methods proceeding in the same way from left to right. Any error in the initial estimate of the motion of one pendulum implies a large error in the corresponding estimate for the pendulums further to the right.

We call this situation "strongly nonself-adjoint" because it is a typical feature of the self-adjoint problem with symmetric coupling that one must consider the whole set of pendulums simultaneously. Similarly, we would characterize the trivial case of a completely one-way coupling as "extreme nonself-adjoint".

In general terms one might state the situation as follows. Self-adjoint systems are represented by symmetrical matrices. Extremely nonself-adjoint systems are represented by matrices all of whose elements vanish on one side of the diagonal; these systems have simple solutions. Systems with matrices having small-valued elements on one side of the diagonal should generally be amenable to easy approximate treatment, especially if these elements are confined to a strip near the diagonal.

13. Appendix C.* Determination of Wick's Eigenvalue by Semiasymptotic Iteration Procedures

This method for determining eigenvalues can perhaps best be illustrated by proceeding step by step through the solution of a specific example. Thus, suppose we want to determine the eigenvalue of eq (44) for the case of Pb, that is, for $\overline{C}/\mu_m=2.90$. To begin with, we backtrack a little and define a variable $u=(\overline{C}/\mu_m)^{1/2}v$. In terms of this variable, eq (44) becomes

$$\left[\overline{C}/\mu_m+\frac{1}{2}u^2\right]\chi_0(u)=(C/\mu_m)\int du'\,\frac{1}{2\pi}e^{-1/2|u-u'|^2}\chi_0(u'). \tag{C1}$$

Next, we multiply this equation by powers of $(u^2/2)$, integrate over the u space, and thus write down formally moment equations of which the first two are

$$\left.\begin{aligned}(\overline{C}/\mu_m)K_0+K_1&=(C/\mu_m)K_0\\(\overline{C}/\mu_m)K_1+K_2&=(C/\mu_m)(K_1+K_0)\end{aligned}\right\}, \tag{C2}$$

where $K_n=(1/2\pi)\int du(u^2/2)^n\chi_0(u)$. If we write $\xi=\overline{C}/\mu_m$ and insert numbers, these two equations become

$$\left.\begin{aligned}\xi K_0+K_1&=2.90K_0\\\xi K_1+K_2&=2.90(K_1+K_0)\end{aligned}\right\}. \tag{C3}$$

Now the right sides of these equations are the moments of a smooth, positive, monotonically decreasing (as $u\to\infty$) function, which we shall call $R(u)$. We shall assume that a reasonable representation for this function is $R(u)=be^{-\beta(u^2/2)}$. From (C1) we then have $\chi_0(u)=[\xi+u^2/2]^{-1}be^{-\beta(u^2/2)}$. If we take moments of this quantity, we readily obtain the relation

$$K_1/K_0=g=\xi\left\{\frac{1}{f(\beta\xi)}-1\right\}, \tag{C4}$$

*By L. V. Spencer.

where $f(x) = xe^x[-Ei(-x)]$. We now establish an iteration procedure using eq (C3) and (C4), namely

$$\left.\begin{aligned} g^{(n+1)} &= \xi^{(n)}\left\{\frac{1}{f(\beta^{(n)}\xi^{(n)})} - 1\right\} \\ \xi^{(n+1)} &= 2.90 - g^{(n+1)} \\ \beta^{(n+1)} &= \frac{1}{g^{(n+1)}+1} \end{aligned}\right\}, \qquad \text{(C5)}$$

where n refers to n'th approximation. The middle equation in (C5) is simply a rewrite of the first of eq (C3), while the last equation in (C5) is obtained by fitting moments of the assumed $R(u)$ to the right sides of eq (C3).

The function $f(x)$ can be easily calculated from standard tables. For interpolation between tabulated values we use the relation $f(x+\delta) \approx f(x)[1+\delta(1+1/x)]-\delta$.

To begin the calculation we make a guess that $g^{(0)}=1$. This yields $\xi^{(0)}=1.90$, $\beta^{(0)}=0.5$, and $\beta^0\xi^0=0.95$. Continuing, $f(0.95)=0.5863$. Thus

$g^{(1)}=1.3407$ $\quad g^{(2)}=1.4556$ $\quad g^{(3)}=1.4864$ $\quad g^{(4)}=1.4931$ $\quad g^{(5)}=1.4951$

$\xi^{(1)}=1.5593$ $\quad \xi^{(2)}=1.4444$ $\quad \xi^{(3)}=1.4136$ $\quad \xi^{(4)}=1.4069$ $\quad \xi^{(5)}=1.405$

$\beta^{(1)}=0.42722$ $\quad \beta^{(2)}=0.40723$ $\quad \beta^{(3)}=0.40219$ $\quad \beta^{(4)}=0.40111$

$f(\beta^{(1)}\xi^{(1)})=0.5172$ $\quad f(\beta^{(2)}\xi^{(2)})=0.49284$ $\quad f(\beta^{(3)}\xi^{(3)})=0.48632$ $\quad f(\beta^{(4)}\xi^{(4)})=0.48481$

The difference between successive ξ's is converging by a factor $\sim$3–4 at each step. Consequently, $\xi^{(\infty)}$ should be, within a small fraction of a percent, equal to 1.404. This yields $\overline{C}=0.484C$. This compares with Wick's variational value of $\overline{C}=0.499C$. (See eq (51).)

This type of calculation can be extended easily by taking into account more of the moment equations (C2). A calculation making use of four moment equations yields an approximate eigenvalue in agreement with that of the variational method to better than 1 percent.

The iteration procedure for the case of a monotonically increasing attenuation coefficient can be set up in the same way. Our original intention was to calculate the eigenvalues of tables 2 and 3 by this method using four moment equations and starting from a variational method value. It turned out, however, that the semiasymptotic calculations agreed to within about a percent or better with the variational calculations in all parts of the tables 2 and 3 and thus we decided to present the numerical values of the variational calculation results obtained from eq (51) and (52).

The agreement between variational and semiasymptotic calculations argues strongly for an accuracy of 1 percent or so in the eigenvalue determinations. However, in practical siuations, K and H depend also upon first and second derivatives, respectively, of μ. These are difficult to determine accurately. There may thus be quite sizeable errors in the tabulated values of H and D (table 3) and of $\dot{\mu}_a/\mu_s$ (table 1).

TABLE 1. *Values of $\dot{\mu}_a/\mu_s$ and C/μ_s for various materials and energies*

Source energy	H_2O		Al		Fe	
	$\dot{\mu}_a/\mu_s$	C/μ_s	$\dot{\mu}_a/\mu_s$	C/μ_s	$\dot{\mu}_a/\mu_s$	C/μ_s
Mev						
10	7.5	7.54	4.1	6.21	------	------
8	6.6	6.87	4.0	5.91	0.48	4.64
6	5.5	5.96	3.8	5.43	1.2	4.56
4	4.0	4.91	3.3	4.68	2.0	4.25
3	3.1	4.22	2.7	4.10	2.1	3.89
2	2.1	3.38	2.0	3.33	1.8	3.30
1	.96	2.37	.96	2.37	.89	2.36
.8	.73	2.12	.73	2.12	.72	2.11
.6	.52	1.86	.52	1.86	.54	1.84
.4	.32	1.58	.32	1.57	.37	1.52
.3	.22	1.41	.22	1.40	.32	1.32
.2	.13	1.23	.155	1.21	.31	1.01
.15	.086	1.12	.145	1.09	.33	0.767

Source energy	Sn		Pb		U	
10	------	------	------	------	------	------
8	------	------	------	------	------	------
6	------	------	------	------	------	------
4	0.40	3.61	------	------	------	------
3	.86	3.49	0.33	2.88	0.22	2.72
2	1.4	3.13	1.7	2.65	2.0	2.48
1	1.1	2.22	1.7	1.75	1.9	1.53
.8	.92	1.95	1.6	1.43	1.8	1.21
.6	.83	1.63	1.5	1.033	1.6	.852
.4	.77	1.17	1.35	.579	1.4	.449
.3	.74	.798	1.2	.333	1.2	.260
.2	.72	.417	.95	.133	.97	.100
.15	.70	.223	.77	.0647	.82	.0485

TABLE 2. *Values of the exponent* $K=\overline{C}/\dot{\mu}_a$ *of the build-up factor for various combinations of the parameters* $\dot{\mu}_a/\mu_a$ *and* $\overline{C}/\mu_a$

[Values of $\dot{\mu}_a/\mu_a$ and $\overline{C}/\mu_a$ for various materials and energies are given in table 1]

$\dot{\mu}_a/\mu_a$	$\overline{C}/\mu_a=0.02$	0.05	0.1	0.25	0.5	1	2	4	6	8
0.02	0.0200	0.0516	0.1095	0.374	2.63	13.00	42.3	113.0	189.5	272
.05	.01939	.0494	.1052	.332	1.328	5.49	17.21	45.5	76.5	108.9
.1	.01846	.0473	.0988	.293	.871	2.98	8.84	23.0	38.5	54.7
.25	.01617	.0411	.0844	.231	.547	1.439	3.81	9.48	15.69	22.2
.5	.01341	.0338	.0687	.1798	.388	.887	2.11	4.96	8.16	11.32
1	.01003	.0252	.0506	.1289	.265	.559	1.211	2.67	4.24	5.87
2	.....	.....	.0335	.0841	.1696	.345	.709	1.477	2.28	3.11
4	.....	.....	.....	.....	.....	.....	.....	.821	1.173	1.674
6	.....	.....	.....	.....	.....	.....	.....	.577	.870	1.165
8	.....	.....	.....	.....	.....	.....	.....	.447	.671	.897

TABLE 3.—*Values of* μ_m, $H=3[\pi^2\overline{C}^2/2\mu_m(d^2\mu/d\lambda^2)_m]^{1/3}$, $D=4H^3/27$ *and* $\overline{C}$ *for various materials*

Material	μ_m	H	D	$\overline{C}$ (cm^2/g per Compton wavelength unit)
	cm^2/g			
H_2O	0.0167	2.0	1.3	0.118
Al	.0216	2.1	1.4	.0942
Fe	.0300	2.8	3.4	.0826
Sn	.0351	2.6	2.7	.0689
W	.0391	2.5	2.4	.0619
Pb	.0410	2.3	1.8	.0594
U	.0425	2.1	1.4	.0565

WASHINGTON, March 17, 1953.

U. S. GOVERNMENT PRINTING OFFICE: 1953

UNITED STATES
GOVERNMENT PRINTING OFFICE
DIVISION OF PUBLIC DOCUMENTS
WASHINGTON 25, D. C.

OFFICIAL BUSINESS

PENALTY FOR PRIVATE USE TO AVOID PAYMENT OF POSTAGE, $300

Journal of Research of the National Bureau of Standards Vol. 51, No. 2 August 19

Contents

		Page
Heat capacity, heats of fusion and vaporization, and vapor pressure of tetrafluoroethylene. George T. Furukawa, Robert E. McCoskey, and Martin L. Reilly.	RP2432	69
Hydrothermal preparation of some strontium silicates. Elmer T. Carlson and Lansing S. Wells.	RP2433	73
Ultraviolet spectral radiant energy reflected from the moon. Ralph Stair and Russell Johnston.	RP2434	81
Phase equilibria in the system MgO-TiO_2. L. W. Coughanour and V. A. DeProsse.	RP2435	85
Pairs of normal matrices with property L. Helmut Wielandt.	RP2436	89
Heat capacity of gaseous hexafluoroethane. John S. Wicklund, Howard W. Flieger, Jr., and Joseph F. Mast.	RP2437	91
Effective circuit bandwidth for noise with a power-law spectrum. Philip R. Karr.	RP2438	93
Penetration of X- and gamma rays to extremely great depths. U. Fano.	RP2439	95

Single copies of the above Research Papers are not available for sale, but the Superintendent of Documents, U. S. Government Printing Office, Washington 25, D. C., will appoint 100 or more copies, and request for the purchase price should be mailed promptly to that Office.

For sale by the Superintendent of Documents, U. S. Government Printing Office, Washington 25, D. C. Price 60 cents
$3.50 per year on subscription; $4.75 foreign

UNITED STATES GOVERNMENT PRINTING OFFICE, WASHINGTON : 1953